STUDIES ON GRAPHITIC CARBON NANOFIBERS: TOWARDS ELECTRONIC, MECHANICAL AND BIOLOGICAL APPLICATIONS

By

Jiang Li

Dissertation

Submitted to the Faculty of the

Graduate School of Vanderbilt University

in partial fulfillment of the requirements

for the degree of

DOCTOR OF PHILOSOPHY

in

Chemistry

August, 2006

Nashville, Tennessee

Approved:

Professor Charles M. Lukehart

Professor Timothy P. Hanusa

Professor G. Kane Jennings

Professor David W. Wright

To my beloved wife, Xiaohua, infinitely supportive

and

To my parents, far away in China

ACKNOWLEDGMENTS

I would like to thank my research advisor, Prof. Charles M. Lukehart, for providing me with the opportunity to work on the research projects and for providing guidance during instructive research talks. I am truly grateful for all the time and support he has given me to pass through those difficulties and to make my projects successful.

I would also like to thank my committee members, Prof. Timothy P. Hanusa, Prof. G. Kane Jennings and Prof. David W. Wright, for their help and support. Additionally, I would like to thank my previous committee members, Prof. Tingyu Li and Prof. L. Roy Xu, for their help at the beginning of my research progress.

There are many people I need to thank for help on respective projects. I would like to thank Dr. Marc R. Knecht for help on amino analysis with Traut's and Ellman's reagents. I need to thank Dr. Junmin Huang for help on Fmoc analysis. I also need to thank Prof. David M. Hercules and Dr. Matthew J. Vergne for acquiring LDI-MS and XPS spectra. I wish to thank Prof. W. Katie Zhong for fabricating GCNF/polymer nanocomposite specimens and measuring mechanical properties.

Further, I would like to thank Prof. William H. Hofmeister for help on spin coating. I need to thank Prof. Timothy S. Fisher, Vance S. Robinson and Yang Liu at Purdue for conducting thermionic emission measurements. I wish to thank Prof. Weijie Lu at Fisk for calcining supported GCNF samples at Wright Patterson. I would like to thank Prof. Raymond L. Mernaugh for conducting GCNF/antibody conjugation and Dr. Conor C.

Lynch for his help on that project. I need to thank Prof. Ronald M. Baldwin for conducting radionuclide trapping on GCNF materials. Cooperation and discussion with these talented people have been really exciting experiences and have provided me with knowledge and skills covering broad scientific areas.

I would like to thank Dr. Eve S. Steigerwalt for her initial work on GCNFs in the Lukehart group and for her help on contact resistance measurements. I also wish to thank Eric D. Mowles for his warm-hearted help during my early months in the Lukehart group. I need to thank all members of the Lukehart group, especially, Dr. Lisa M. Sullivan, Jason A. Michel, Lang Li, William H. Morris and Matthew S. Wellons.

This work would not have been possible without the financial support of Vanderbilt University (Discovery Grant), the Department of Chemistry, the Graduate School, the Vanderbilt Institute of Nanoscale Science and Engineering, National Science Foundation (NIRT Grant # CTS-0210366), National Aeronautics and Space Administration (NAS1-01047), Department of Defense (DASG 60-02-P-0104 and DASG 60-02-P-0245).

Most importantly, I would like to thank Xiaohua Wu being a wonderful presence in my life and my parents in China for their love, support and patience.

TABLE OF CONTENTS

LIST OF TABLES

LIST OF SCHEMES

LIST OF FIGURES

LIST OF ABBREVIATIONS

AFC:	alkaline fuel cell
Ahx-OH:	aminohexanoic acid
APTES:	3-aminopropyl triethoxysilane
ASTM:	American Society for Testing and Materials
BGE:	butyl glycidyl ether
CNTs:	carbon nanotubes
CT:	computed tomography
CVD:	chemical vapor deposition
DIC:	N,N’-diisopropylcarbodiimide
DIEA:	N,N-diisopropylethylamine
DMF:	N,N-dimethyl formamide
DMFC:	direct methanol fuel cell
DMG:	N,N-dimethylglycine
DSG:	disuccinimidyl glutarate
DTNB:	5,5’-dithio-bis-(2-nitrobenzoic acid), Ellman’s reagent
EDAC:	1-(3-(dimethylamino)propyl)-3-ethylcarbodiimide
EDX:	energy dispersive X-ray spectroscopy
ELISA:	enzyme-linked immunosorbent assay

ESI-MS:	electrospray ionization mass spectrometry
FDG:	2-[^{18}F]fluoro-2-deoxy-D-glucose
Fmoc:	fluorenylmethyloxycarbonyl
GCNFs:	graphitic carbon nanofibers
GDLs:	gas diffusion layers
HDA:	1,6-hexamethylenediamine
HMDS:	hexamethyl disilazane
HOBt:	1-hydroxybenzotriazole
HR:	high-resolution
ICDD:	International Center for Diffraction Data
IgG:	immunoglobulin G
IR:	infrared (spectra)
LDI-MS:	laser desorption/ionization mass spectrometry
MCFC:	molten carbonate fuel cell
MRI:	magnetic resonance imaging
MWNTs:	multi-walled carbon nanotubes
NHSS:	N-hydroxysulfosuccinimide
ODA:	3,4’-oxydianiline
PAFC:	phosphoric acid fuel cell
PDA:	1,4-phenylenediamine

PDF:	powder diffraction file
PEMFC:	polymer electrolyte membrane fuel cell
PET:	positron emission tomography
SEM:	scanning electron microscopy
SOFC:	solid oxide fuel cell
SWNTs:	single-walled carbon nanotubes
TAB:	1,3,5-tris(4-aminophenoxy)benzene
TAPA:	tris(4-aminophenylene)amine
TAPE:	tris[4-(4-aminophenoxy)phenyl]ethane
TBTU:	1-[bis(dimethylamino)methylene]-1*H*-benzotriazolium tetrafluoroborate 3-oxide
TEEDs:	thermionic electron energy distributions
TEM:	transmission electron microscopy
TFAA:	trifluoroacetic anhydride
TGA:	thermogravimetric analysis
THF:	tetrahydrofuran
TMOS:	tetramethoxysilane
TMS:	tetramethylsilane
TPO:	temperature-programmed oxidation
XDA:	*p*-xylylenediamine

XPS: X-ray photoelectron spectroscopy

XRD: X-ray diffraction

ABSTRACT

Graphitic carbon nanofibers (GCNFs) have become the subject of extensive research due to their high aspect ratio, large surface area, superior electronic and mechanical properties. A variety of nanocomposites containing GCNFs have been designed, synthesized and characterized in this study. Surface-reactive carbon atoms have enabled the surface functionalization of herringbone GCNFs with covalently bound linker molecules, including diamines, triamines and an aminoalkoxysilane. GCNF/epoxy nanocomposites have been fabricated using GCNFs surface-derivatized with diamine linker molecules, and bending test data have revealed enhanced flexural strength for these nanocomposites over pure epoxy specimens. In addition, GCNF/silica xerogel nanocomposites prepared via sol-gel chemistry of GCNF/amidoalkoxysilane have displayed improved wetting and dispersion of GCNFs within a ceramic matrix. Further, attempts to bind antibodies and radionuclides onto surface-functionalized GCNFs have demonstrated interesting results for potential biological applications. Moreover, GCNFs have been grown on diverse substrates, including silicon wafers, carbon felt and carbon paper. Work functions of GCNFs have been acquired from thermionic electron emission measurements. GCNF/SiC/carbon felt nanocomposites prepared by carbothermal reduction exhibit optimized mechanical robustness, high chemical stability and reversible superhydrophobicity, and serve as a close structural mimic of a lotus leaf. Furthermore,

the electrical resistance of GCNF/carbon paper nanocomposites has been evaluated for potential use as gas diffusion layers in fuel cells.

CHAPTER I

INTRODUCTION

1.1 Graphitic Carbon Nanofibers

Graphitic carbon nanofibers (GCNFs) have attracted a lot of interest from chemists, physicists, and material scientists during the last decade.[1,2] It is known that these nanofibers can be prepared having controlled diameters between 10 through 200 nm and lengths between a few to tens of microns. High-resolution transmission electron microscopic (HR-TEM) images show that nanofibers consist of orderly stacked graphene layers. Based on the stacking directions of graphene layers with respect to the long axis of nanofibers, they are often classified into three types, "platelet" (perpendicular), "parallel", and "herringbone", as represented in Figure 1.[3,4]

GCNFs are synthesized catalytically from carbonaceous gas decomposition on a transition metal catalyst at 500-700 °C.[3] The arrangement of graphene layers can be tailored to a desired geometry by choice of catalyst system and synthesis conditions.[5] For example, the growth catalyst can be made of Fe, Co, Ni, Cu, Pt or their alloys, while the carbonaceous gas as carbon source may be methane, ethane, ethylene, propane, or carbon monoxide.[6]

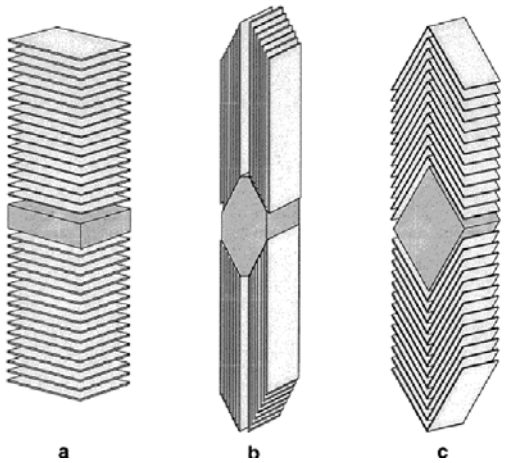

Figure 1. Schematic representation of graphene layer orientation in three types of GCNFs: (a) platelet, (b) parallel, and (c) herringbone arrangements. (Reprinted from ref 4. Copyright 2001 American Chemical Society.)

The growth mechanism of graphitic carbon nanofibers has been investigated since the 1970's.[7] Recent reports on *in situ* TEM observations and *ab initio* simulations are consistent with an adsorption-diffusion-precipitation mechanism as follows (Figure 2): (1) dissociative adsorption of carbon-containing compounds on favorable crystal facets of metal growth catalyst particles, (2) diffusion of adsorbed carbon atoms along the surface and subsurface of metal catalyst particles to those crystal facets favoring graphene precipitation, and (3) precipitation of carbon atoms on the crystal facets forming carbon nanofibers.[8-10] The details of growth mechanism are discussed in Appendix D.

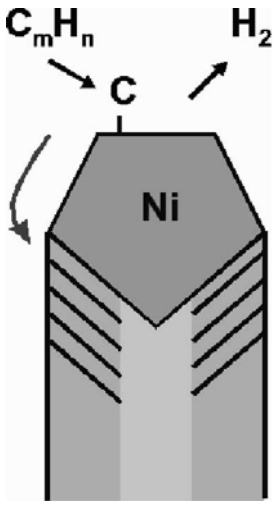

Figure 2. Schematic illustration of growth mechanism of herringbone GCNFs. (Reprinted from ref 9. Copyright 2001 American Physical Society.)

GCNFs possess specific electrical, thermal, and mechanical properties that are promising for a variety of applications. As reported in the literature, CVD-grown herringbone carbon nanofibers have electrical conductivity as high as 2.4×10^4 S m^{-1},[11-13] while the axial Young's modulus of a single GCNF has been reported to be over 600 GPa.[14] Moreover, GCNFs have a large aspect ratio up to 1000 and high surface areas. Therefore, it is not surprising that many studies have been conducted on GCNF applications, such as supercapacitors,[15] hydrogen storage,[16] field-emission devices,[17] radionuclide adsorption,[18] heterogeneous catalyst support,[19-21] and electroanalytical utility.[22]

1.2 Graphene Layers and Carbon Nanotubes

GCNFs consist of orderly stacked graphene layers, which are held together by weak

van der Waals forces as found in graphite. It is known that graphene layers comprise hexagons with side length of 0.1426 nm (C-C bond distance, $d_{C\text{-}C}$) with interlayer spacing of 0.3362 nm (d_{002}) (ICDD PDF # 41-1487). Those carbon atoms making up graphene layers have three sp^2-hybridized electrons, covalently shared between neighbors in the plane, and one *p* electron delocalized among all the atoms in the plane, accounting for the high in-plane electrical and thermal conductivity of both GCNFs and graphite. Carbon atoms along the armchair and zigzag edges of the graphene layers are incompletely bonded and those unsaturated atoms are of higher reactivity than the saturated ones (Figure 3). Each unsaturated carbon atom is occupying 0.083 nm^2 and 0.072 nm^2 on zigzag and armchair edges, with an average of 0.078 nm^2 per carbon atom.

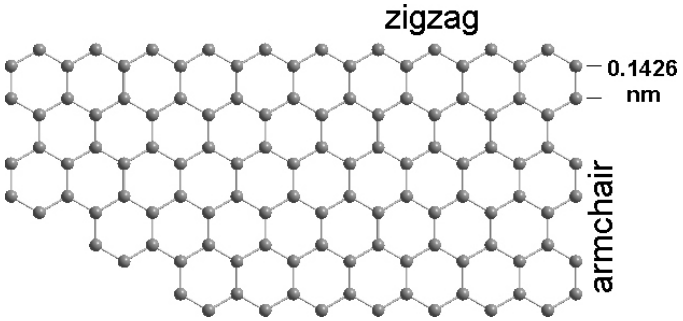

Figure 3. Schematic illustration of a graphene layer showing armchair edges and zigzag edges.

Comparison of Figure 1 and 3 will help understand the structural specificity of graphitic carbon nanofibers. Large numbers of unsaturated carbon atoms are present along the side surfaces of platelet and herringbone GCNFs, while a much reduced

number of reactive carbon atoms are present along the side surfaces of parallel GCNFs, since the surfaces are mainly of basal graphene layers. The presence of large numbers of reactive carbon atoms on platelet and herringbone GCNFs makes them distinguishable from parallel GCNFs and other carbon nanostructures, as discussed below.

Carbon nanotubes, based on rolled-up graphene layers, have been one of the most attractive materials throughout diverse fields since Iijima's discovery in 1991.[23] There are two distinct types of carbon nanotubes: single-walled and multi-walled carbon nanotubes. Single-walled carbon nanotubes (SWNTs) are made of one rolled graphene layer and one or two hemisphere caps, while multi-walled carbon nanotubes (MWNTs) consist of concentric rolled graphene layers. Because the graphene layer can be rolled up along different chiral vectors $\boldsymbol{R} = m\boldsymbol{a_1} + n\boldsymbol{a_2}$, SWNTs may have varying degrees of twist along its long axis, such as [5,5] armchair, [9,0] zigzag, and [10,5] chiral nanotubes as shown in Figure 4.[24] Given the specific mechanical, electrical, optical, and thermal properties of carbon nanotubes, studies on the synthesis,[25,26] separation,[27-29] modification[30-32] and device fabrication[33] of carbon nanotubes have been employed towards diverse applications.

Another form of carbon nanostructure, fullerene, which was discovered by Smalley in 1985,[34] is a closed-cage carbon molecule with three-coordinate carbon atoms. The best known example is C_{60}, a truncated icosahedral structure formed by twelve pentagonal rings and twenty hexagonal rings. There is an extensive literature on the synthesis, modification and application of fullerenes, especially for electron transfer in

donor-acceptor systems.[35]

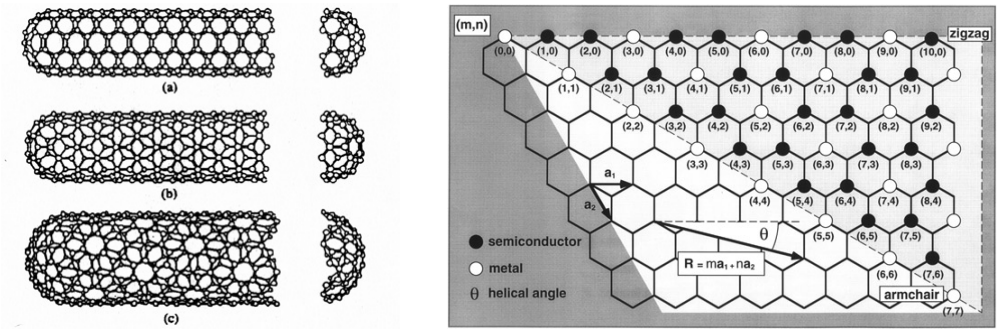

Figure 4. (left) Schematic representation of SWNTs: (a) [5,5] armchair, (b) [9,0] zigzag, and (c) [10,5] chiral nanotubes and (right) the indexing scheme of graphene layer to create nanotube cylinders. (Reprinted from ref 24 and 25. Copyright 2001 Wiley-VCH and 1997 Institute of Physics.)

Other forms of carbon structures, such as carbon foams,[36,37] carbon nanowires,[38,39] carbon nanoscrolls,[40] carbon nanorods,[41] nanodiamonds,[42,43] and ordered mesoporous carbon,[44] have been explored in research labs for different applications.

1.3 Overview of Research Projects

Compared with other carbon materials, graphitic carbon nanofibers (GCNFs) have many advantages including ease of growth, structural variety, high chemical reactivity, and superior mechanical and electrical properties. Based on these advantages, the research described in this thesis involves several projects on the chemistry of GCNFs for a variety of applications.

Poor dispersibility and chemical inertness of as-prepared carbon nanostructures have

been obstacles to the incorporation of these materials into composites and devices. Herringbone GCNFs have reactive edge carbon atoms, which are beneficial for covalent attachment of reactive linker molecules to carbon nanofiber surfaces. Chapter II reports the preparation and characterization of herringbone GCNF/linker molecule materials derived from seven diamines and triamines.[45] The GCNF/linker molecule materials are characterized by microscopic, analytical and spectroscopic methods. Direct evidence identifying linker molecule composition is provided by LDI-MS and by quantitative XPS analysis of trifluoroacetylated derivatives, while the presence of reactive pendant amino groups is determined quantitatively via the Fmoc method and synthetically by effecting nucleophilic ring-opening oligomerization of epoxy monomer.

The introduction of amino groups onto the surface of GCNFs enables much chemistry possible for nanofiber/polymer composite fabrication. Strong covalent bonding at a nanofiber/polymer interface may impart a high degree of nanofiber wettability and dispersibility and enhance mechanical and other properties of the resulting nanocomposite material. Chapter III focuses on the fabrication of GCNF/epoxy nanocomposites with varying nanofiber loadings and three-point bending tests on these nanocomposite samples.[46-49] The bending test data demonstrate enhanced flexural strength and breaking strain for GCNF/epoxy nanocomposites over pure epoxy specimens.

During the preparation of ceramic-based composites containing carbon nanostructures, there remains a generally recognized problem of how to achieve excellent

wetting of the hydrophobic carbon surface by a polar ceramic matrix. Chapter IV reports the formation of GCNF/silica xerogel composites using sol-gel processing.[50] Co-hydrolysis and condensation of tetramethoxysilane in the presence of GCNFs surface-derivatized with sol-gel reactive 3-amidopropylsilyl functional groups afford a high degree of covalent binding across the GCNF/ceramic interface on the nanoscale. Enhanced wetting and dispersion of GCNFs are confirmed by visual observation and SEM images.

Growth of carbon nanofibers or carbon nanotubes on silicon wafers has attracted extensive interest for diverse applications. Chapter V demonstrates the growth of graphitic carbon nanofibers on silicon wafers after spin-coating catalyst precursor powders onto silicon wafer surfaces. Work functions have been derived based on the total electron energy distributions from thermionic electron emission measurements of these wafer-supported graphitic carbon nanofibers.

Superhydrophobic materials, with water contact angles larger than 150^{o}, have been an important topic during the last few years for novel applications. A closely related phenomenon in nature, the lotus-leaf effect, is based on the binary structure of a lotus leaf on both micro- and nano-scale and its "self-cleaning" capability has been attributed to this hierarchical structure. In Chapter VI, two types of GCNFs have been grown on weakly hydrophobic carbon felt to mimic the hierarchical structure of a lotus leaf. Carbothermal treatment of GCNF/SiO_2/carbon felt nanocomposites yields GCNF/SiC/carbon felt nanocomposites, which have displayed optimized mechanical

robustness and chemical stability. Water contact-angle measurements reveal that only the carbothermally treated GCNF/carbon felt sample shows superhydrophobicity, while bulk density measurements indicate a bulk density of 0.11 g/cm^3 for the GCNF/SiC/carbon felt sample, only one fifth of that for carbon felt (0.64 g/cm^3). Furthermore, this superhydrophobic sample can be reversibly changed to being hydrophilic with simple hot water treatment and then back to being superhydrophobic upon vacuum drying, indicating a close mimicking of both the hierarchical structure and wetting property of lotus leaves.

Polymer electrolyte membrane (PEM) fuel cells have been widely explored as power sources for automobile propulsion and for portable electronics. In a single PEM fuel cell, the electrical resistance between two bipolar plates, mainly from the bulk resistance of gas diffusion layers and from the contact resistance between gas diffusion layers and bipolar plates, imposes an undesired loss of cell output voltage, which should be minimized. In Chapter VII, herringbone-structure GCNFs have been grown on the micro-scale fibers of carbon paper, a popular material for gas diffusion layers. Then, a model fuel cell assembly has been constructed using the GCNF/carbon paper composite samples as gas diffusion layers and the voltage drop of the model cell assembly has been tested as a function of compression pressure in an effort to decrease the fuel cell resistance.

Various biomolecules, such as antibodies, have been bound onto carbon nanotubes via physical adsorption (hydrophobic interactions), electrostatic forces, or covalent

bonding. These CNT/antibody conjugates have been tested for detection of proteins and cells via antibody-antigen interactions. In Appendix A, attempts at binding rabbit IgG antibodies to surface-functionalized GCNF nanofibers using a bifunctional cross-linker, disuccinimidyl glutarate, are discussed. The conjugated antibodies were detected with enzyme-linked immunosorbent assay (ELISA). The preliminary data suggest that antibodies are likely to bind with nanofibers via hydrophobic interactions, which make the cross-linker unnecessary.

Positron emission tomography (PET) is a novel bioimaging technique for clinical oncology diagnosis and neuroscience research. The basics of PET technique are to image and quantify the in vivo distribution of positron-emitting radioisotopes such as fluorine-18, which can be substituted into receptor ligands to monitor the biological functions of those receptors. GCNFs are promising candidates as vehicles delivering radioligands given their bioinertness, high aspect ratio and large surface area. Appendix B exhibits preliminary data on radiohalide ion trapping on surface-functionalized GCNFs. The amino groups on GCNF/ODA surface can be transformed into quaternary ammonium cations with amide coupling and methylation reactions. Then, the triflate anion associated with methylation was exchanged with radioactive [^{18}F]fluoride or [^{123}I]iodide via sonication or stirring. The net trapping efficiency was evaluated.

CHAPTER II

SURFACE FUNCTIONALIZATION OF GCNFS WITH DIAMINE AND TRIAMINE LINKER MOLECULES[45]

2.1 Introduction

Poor dispersibility and chemical inertness of as-prepared carbon nanostructures have been obstacles to the incorporation of these materials into composites and devices. Surface modification is critical for resolving these problems, as surface-bound functional groups can enhance the wettability, dispersibility, and surface reactivity of carbon nanostructures in fluids and further improve the carbon/matrix interfacial binding within composite materials.

Two strategies commonly employed to modify carbon nanostructure surfaces are covalent functionalization of surface carbon atom sites[51] and noncovalent wrapping of carbon nanostructures with surfactants, polymers, or ceramic coatings.[52,53] Covalent attachment of reactive linker molecules to carbon nanostructure surfaces is particularly attractive, given the numerous known methods for covalently binding reactive molecules to inert surfaces. Reactions between linker molecules and matrix functional groups can then afford carbon/matrix interfaces of high covalent integrity.

There is a vast literature reporting successful surface functionalization of single-walled carbon nanotubes (SWNTs),[54,55] multi-walled carbon nanotubes (MWNTs),[56] and vapor-grown carbon nanofiber materials.[57] Haddon and coworkers

have shown that single-walled carbon nanotube (SWNT) bundles can be exfoliated with 2.6 M nitric acid to give individual SWNTs bearing terminal carboxylic acid groups.[54] Exfoliation under more rigorous conditions leads to oxidation of side-wall carbon sites along with partial degradation of the electronic and mechanical properties of the nanotubes.[51] Sun and coworkers have reported nitric acid oxidation of fullerene nanostructures with similar observations.[58] As discussed in Section 1.2, graphitic carbon nanofibers (GCNFs), particularly those having the platelet or herringbone structures,[1,3] possess unsaturated edge-site carbon atoms of each graphene layer terminating the nanofiber surface and are especially suitable for surface functionalization.

This chapter reports the preparation and characterization of seven herringbone GCNF/linker molecule materials derived from the following three types of linker molecules: (1) aliphatic diamines, including 1,6-hexamethylenediamine (HDA) and *p*-xylylenediamine (XDA); (2) aromatic diamines, including 1,4-phenylenediamine (PDA) and 3,4'-oxydianiline (ODA); (3) aromatic triamines, including tris(4-aminophenylene)amine (TAPA), 1,3,5-tris(4-aminophenoxy)benzene (TAB), and tris[4-(4-aminophenoxy)phenyl]ethane (TAPE). GCNF surface oxidation and functionalization by a linker molecule is accomplished by following a stepwise process involving amidation chemistry (Scheme 1).

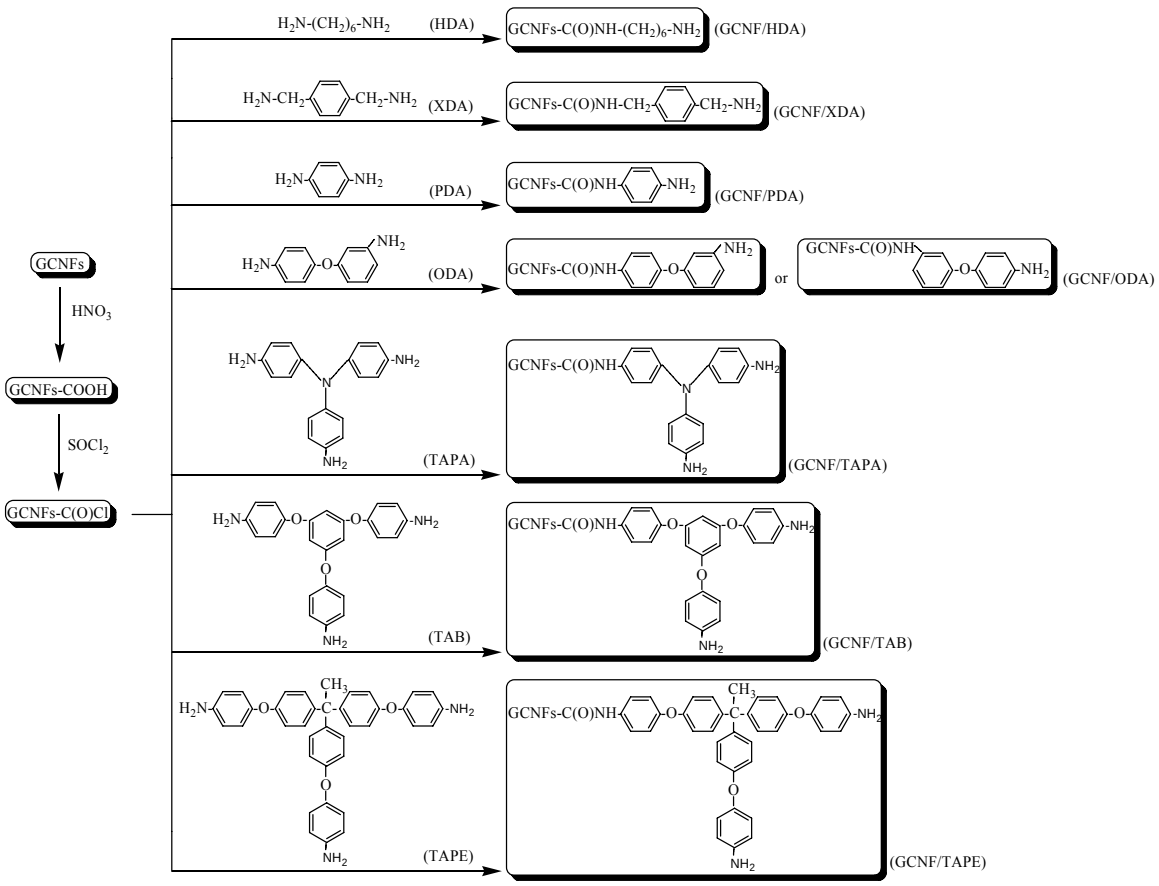

Scheme 1. Surface oxidation, acylation, and functionalization of graphitic carbon nanofibers (see Experimental section for reaction conditions).

GCNF materials are characterized by TEM, IR, TGA, laser desorption/ionization mass spectrometry (LDI-MS), and by elemental analysis. Direct evidence identifying linker molecule compositions is provided by LDI-MS and by quantitative XPS analysis of trifluoroacetylated derivatives, while the presence of reactive pendant amino groups is determined quantitatively via the Fmoc method and synthetically by effecting nucleophilic ring-opening oligomerization of epoxy monomer. Approximate GCNF/(linker molecule)$_x$ compositions are proposed consistent with acid-uptake and

elemental analysis data. Successful formation of highly functionalized GCNF materials using amide-coupling chemistry provides a convenient method for tailoring GCNF dispersibility and reactivity. A wide variety of applications using a GCNF/amido linker molecule platform can now be explored.

2.2 Experimental Section

2.2.1 General Procedures

Solvents were distilled prior to use. All gaseous reagents were obtained from Air Liquide Gas. 1,6-Hexamethylenediamine (HDA), *p*-xylylenediamine (XDA), 1,4-phenylenediamine (PDA), 3,4'-oxydianiline (ODA), and tris(4-nitrophenylene)amine were purchased from Aldrich Chemical Company, Inc. 1,3,5-tris(4-aminophenoxy)benzene (TAB) and tris[4-(4-aminophenoxy)phenyl]ethane (TAPE) were kindly supplied from the NASA John H. Glenn Research Center, Cleveland, OH. Other reagents are reagent grade and used as obtained.

Transmission electron microscopy (TEM) was performed on a Philips CM-20T Electron Microscope operated at 200 kV. Proton nuclear magnetic resonance spectra (NMR) were recorded on a Bruker AC300 FT-NMR Spectrometer using tetramethylsilane (TMS) as internal standard. Infrared spectra (IR) were recorded from KBr pellets on an ATI Mattson Genesis Series FT-IR spectrometer.

Laser desorption/ionization mass spectra (LDI-MS) were acquired using an Applied

Biosystems Voyager DE-STR mass spectrometer (Framingham, MA) with a 337 nm N_2 laser. The acceleration voltage was 25 kV, and the spectra were acquired in the linear mode with positive ion detection. For sample preparation, the sample powders were spread onto double-sided carbon tape and placed on the mass spectrometer sample plate.

X-ray photoelectronic spectroscopic (XPS) curves were collected on a Leybold Heraeus ES-10 X-ray photoelectron spectrometer. For sample preparation, the sample powders were placed on double-sided carbon tape adhered to the sample mount. Spectra were acquired with Mg K_α excitation at 250 watts of power (12.5 kV voltage and 20 mA current) and with 200 eV pass energy. XPS spectra were collected of the fluorine 1s (689 eV) and nitrogen 1s (400 eV) regions. To determine the relative sensitivity factors for fluorine and nitrogen, both the F 1s region and the N 1s region for the XPS spectra of an ODA$[C(O)CF_3]_2$ sample (synthesized as below) were collected and integrated. If the measured sensitivity factor for fluorine on the XPS instrument is set to a value of unity ($S_F = 1$), the measured sensitivity factor for nitrogen (S_N) using ODA$[C(O)CF_3]_2$ is 0.28.

Bulk elemental analysis was performed by Atlantic Microlab, Inc. Norcross, GA. Every sample was analyzed twice and values were averaged for composition calculation. Thermogravimetric analyses (TGA) were performed on a Thermal Analysis Instruments High-Resolution TGA 2950 Thermogravimetric Analyzer with heating rate of 15 $^oC\ min^{-1}$ in an atmosphere of nitrogen. BET surface area analysis was determined from N_2 adsorption/desorption isotherms recorded with a Quantachrome NOVA 1000 high-speed surface-area analyzer.

Surface acidic functionality was determined by the base-uptake method.[59] Approximately 100 mg of the surface-treated nanofibers were placed into 40 mL of 1 mM sodium hydroxide solution. The mixture was allowed to stand for 18 h. The pH value was recorded before and after base uptake and the number density of acidic sites was calculated.

Similarly, surface basic functionality was determined by the acid-uptake method.[59] Approximately 200 mg of the surface-treated nanofibers were placed into 40 mL of 1 mM hydrochloric acid solution. The mixture was allowed to stand for 18 h. The pH value was recorded before and after acid uptake and the number density of basic sites was calculated.

The content of free primary amino groups on surface-derivatized nanofibers was quantitatively determined by three methods: with Traut's and Ellman's reagents,[60] the ninhydrin method[61] and the Fmoc method.[62] In a typical surface amino group analysis with Traut's and Ellman's reagents (Scheme 2), 2-10 mg of Traut's reagent (2-iminothiolane·HCl, Pierce) was dissolved in 5 mL of 50 mM triethanolamine·HCl buffer solution (0.15 M HCl, 1 mM EDTA, pH = 8.0) and mixed with 100 mg of a GCNF sample. The mixture was incubated under nitrogen for 45 min at room temperature. After centrifugation, the supernatant was discarded, and the solid was washed with 5 mL of buffer solution twice. Then the solid sample was mixed with 5 mL of 1 mM Ellman's reagent (5,5'-dithio-bis-(2-nitrobenzoic acid), DTNB, Pierce) in Na_2HPO_4 buffer solution (pH = 8.0) and incubated for 15 min at room temperature. After centrifugation,

absorbance of the supernatant at 412 nm was measured. Fresh cysteine solution (Na_2HPO_4 buffer, pH = 8.0) was used to react with Ellman's reagent to prepare a standard curve for amine content calculation. Analysis of surface amino groups with the ninhydrin method followed a literature procedure (Scheme 3).[61]

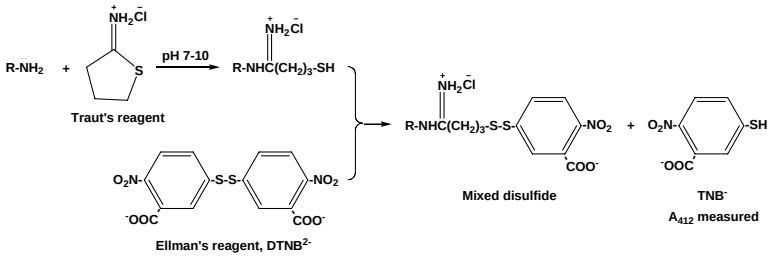

Scheme 2. Reactions using Traut's and Ellman's reagents for amino analysis.

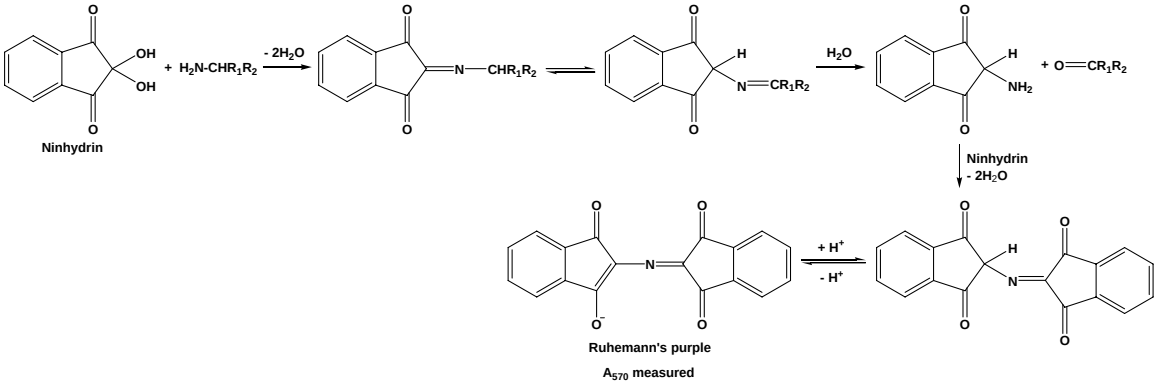

Scheme 3. The ninhydrin method for amino analysis.

In a typical surface amino group analysis with the Fmoc method (Scheme 4),[62] 150 mg of derivatized GCNFs were mixed with 175 mg of fluorenylmethyloxycarbonyl aminohexanoic acid (Fmoc-Ahx-OH, NOVA Biochem), 67.5 mg of 1-hydroxybenzotriazole (HOBt, Aldrich) and 1 mL of N,N-dimethyl formamide (DMF).

After dissolution of Fmoc-Ahx-OH and HOBt, 80 μL of N,N'-diisopropylcarbodiimide (DIC, Aldrich) was added. Reaction occurred by shaking for 12 h. The mixture was filtered and the solid was washed with DMF, methanol and methylene chloride, and dried under reduced pressure overnight. Twenty milligram of dried sample was mixed with 3 mL of a mixture of piperidine (Aldrich) and DMF (20:80), and shaken for 45 min. After centrifugation, the UV absorption of the supernatant was measured at 290 nm and the concentration of amino groups in the functionalized GCNF samples was calculated.

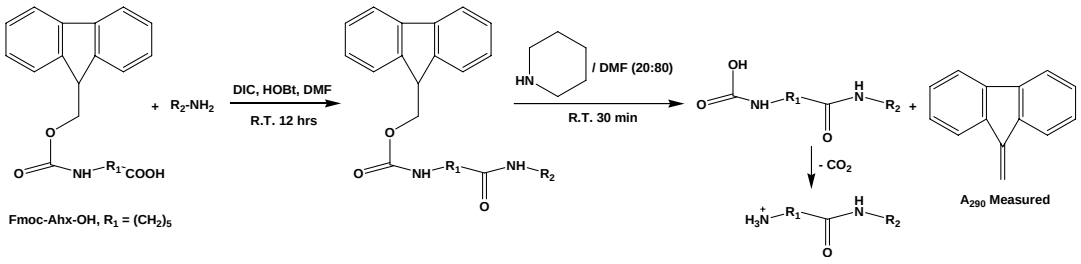

Scheme 4. The Fmoc method for amino analysis.

2.2.2 Synthesis and Surface Derivatization of Graphitic Carbon Nanofibers

Synthesis of Graphitic Carbon Nanofibers

Herringbone-type carbon nanofibers were grown by the interaction of a carbon source gas with mixed-metal powder growth catalyst, following a modified literature procedure.[3] Iron-copper powder with atomic ratio of 7:3 was prepared by the coprecipitation of the respective metal nitrate solutions, containing $Fe(NO_3)_3 \cdot 9H_2O$ (4.84 g, 12.0 mmol) and $Cu(NO_3)_2 \cdot 3H_2O$ (1.26 g, 5.2 mmol) with excess ammonium

bicarbonate. The precipitate was dried in an oven at 110 °C and ground into fine powder (1.5 g). The powder (300 mg) was put into a quartz boat in a horizontal tubular furnace (Lindberg 55341) and was converted into metal oxide mixture by calcining in the air at 400 °C for 4 h. The mixed-metal oxide was reduced in a 20% H_2/He flow of 250 mL/min at 500 °C for 20 h. After the catalyst was further reduced at 600 °C for 2 h, ethylene was introduced to the reactor with the gas composition of 4:1:1 for C_2H_4:H_2:He (total 300 mL/min). The growth of carbon nanofibers was completed at 600 °C after 90 min. The product was cooled to room temperature under helium and collected (10.7 g). Anal. Found: C, 95.78; H, 0.29; O, 0.22.

Surface Oxidation and Acylation of Carbon Nanofibers

To derivatize the carbon nanofibers, GCNFs (2.0 g) were treated with concentrated nitric acid (200 mL) at 140 °C for 4 h. After washing with deionized water until the filtrate reached a pH value of ca. 7, the sample was dried *in vacuo* at room temperature and collected (1.4 g). Anal. Found: C, 86.82; H, 0.50; N, 0.22. The surface-oxidized carbon nanofibers were acylated by reaction with thionyl chloride (30 mL) at 70 °C for 24 h with 0.5 mL of DMF. The mixture was cooled and washed with distilled tetrahydrofuran (THF) under nitrogen until the supernatant was clear. The black solid of surface-acylated carbon nanofibers was dried by purging with nitrogen at room temperature for further use.

Preparation of Carbon Nanofibers with Surface-Bound 1,6-Hexamethylenediamine (HDA)

Surface-acylated GCNFs were reacted with 1,6-hexamethylenediamine (10 g) at 100 °C under nitrogen for 96 h. The mixture was cooled to room temperature. The excess 1,6-hexamethylenediamine was dissolved by stirring with acetone for 30 min. After vacuum filtration and washing with acetone, the 1,6-hexamethylenediamine-derivatized graphitic carbon nanofibers (abbreviated as GCNF/HDA) were dried at reduced pressure overnight. Anal. Found: C, 87.44; H, 1.66; N, 2.35.

Preparation of Carbon Nanofibers with Surface-Bound p-Xylylenediamine (XDA)

Surface-acylated GCNFs were reacted with *p*-xylylenediamine (10 g) at 100 °C under nitrogen for 96 h. The mixture was cooled to room temperature. The excess *p*-xylylenediamine was dissolved by stirring with toluene for 30 min. After vacuum filtration and washing with toluene, the *p*-xylylenediamine-derivatized graphitic carbon nanofibers (abbreviated as GCNF/XDA) were dried at reduced pressure overnight. Anal. Found: C, 84.17; H, 1.92; N, 4.00.

Preparation of Carbon Nanofibers with Surface-Bound 1,4-Phenylenediamine (PDA)

Surface-acylated GCNFs were reacted with 1,4-phenylenediamine (10 g) at 150 °C under nitrogen for 96 h. The mixture was cooled to room temperature. The excess 1,4-phenylenediamine was dissolved by stirring with ethanol for 30 min. After vacuum filtration and washing with ethanol, the 1,4-phenylenediamine-derivatized graphitic carbon nanofibers (abbreviated as GCNF/PDA) were dried at reduced pressure overnight.

Anal. Found: C, 85.31; H, 1.44; N, 3.97.

Preparation of Carbon Nanofibers with Surface-Bound 3,4'-Oxydianiline (ODA)

Surface-acylated GCNFs were reacted with 3,4'-oxydianiline (10 g) at 100 °C under nitrogen for 96 h. The mixture was cooled to room temperature. The excess 3,4'-oxydianiline was dissolved by stirring with ethanol for 30 min. After vacuum filtration and washing with ethanol, the 3,4'-oxydianiline-derivatized graphitic carbon nanofibers (abbreviated as GCNF/ODA) were dried at reduced pressure overnight. Anal. Found: C, 86.66; H, 1.19; N, 2.14.

Preparation of Carbon Nanofibers with Surface-Bound Tris(4-aminophenylene)amine (TAPA)

Tris(4-aminophenylene)amine (TAPA) was prepared from reduction of tris(4-nitrophenylene)amine with 10 wt% Pd/C catalyst following the literature procedure.[63] Surface-acylated GCNFs were reacted with tris(4-aminophenylene)amine (5 g) at 250 °C under nitrogen for 1 h. The mixture was cooled to room temperature. The excess tris(4-aminophenylene)amine was dissolved with ethanol. The tris(4-aminophenylene)amine-derivatized graphitic carbon nanofibers (abbreviated as GCNF/TAPA) were obtained by vacuum filtration and dried at reduced pressure overnight. Anal. Found: C, 88.63; H, 1.40; N, 3.40.

Preparation of Carbon Nanofibers with Surface-Bound 1,3,5-Tris(4-aminophenoxy)benzene (TAB)

Surface-acylated GCNFs were reacted with TAB (5 g) at 150 °C under nitrogen for

96 h. The mixture was cooled to room temperature. The excess TAB was dissolved by stirring with ethanol for 30 min. After vacuum filtration and washing with ethanol, the TAB-derivatized graphitic carbon nanofibers (abbreviated as GCNF/TAB) were dried at reduced pressure overnight. Anal. Found: C, 86.66; H, 1.33; N, 2.32.

Preparation of Carbon Nanofibers with Surface-Bound Tris[4-(4-aminophenoxy)phenyl]ethane (TAPE)

Surface-acylated GCNFs were reacted with TAPE (5 g) at 220 °C under nitrogen for 4 h. The mixture was cooled to room temperature. The excess TAPE was dissolved by stirring with dimethyl sulfoxide for 30 min. After vacuum filtration and washing with dimethyl sulfoxide, the TAPE-derivatized graphitic carbon nanofibers (abbreviated as GCNF/TAPE) were dried at reduced pressure overnight. Anal. Found: C, 86.32; H, 1.36; N, 1.65.

Sonication of GCNF/ODA with Butyl Glycidyl Ether

Surface-derivatized GCNF/ODA products (0.25 g) were mixed with 20 mL of diluent, butyl glycidyl ether (BGE, Aldrich), and sonicated at a power level of 70 watts for 60 min using a Branson Digital Sonifier (Model 450). After sonication, excess diluent in the GCNF/ODA/BGE liquid blend was evaporated at 80 ^{o}C and a yellow solid was obtained.

Trifluoroacetic Anhydride (TFAA) Treatment of Functionalized GCNFs for XPS Measurements

In a typical TFAA treatment experiment, 100 mg of derivatized GCNFs were stirred with 1.2 mL of N,N-diisopropylethylamine (DIEA, 7 mmol) and 10 mL of ether. To the

suspension was added 1 mL of trifluoroacetic anhydride (7 mmol). After reaction at room temperature for 3 days with continuous stirring, the reaction mixture was filtered. The black solid was washed with ether, acetone, water, and acetone and dried under reduced pressure overnight.

A calibration standard was prepared by derivatizing the free diamine ODA with TFAA following the same reaction procedure as above. After reaction at room temperature for 4 h with continuous stirring, the solution was mixed with 10 mL of water. The organic layer was collected and filtered. The target product ($ODA[C(O)CF_3]_2$) was isolated with column chromatography and collected by evaporating the solvent. ^1H NMR (300 MHz, CD_2Cl_2): δ [ppm] = 1.50 (s, 2H, NH), 6.83-7.88 (m, 8H, Ar); ESI-MS 393.3 amu [$ODA[C(O)CF_3]_2$, $(M+H)^+$].

2.3 Results and Discussion

2.3.1 GCNF Preparation, Surface Derivatization, and Morphology

GCNFs having a herringbone graphene layer structure are prepared by a known process in which decomposition of a carbonaceous gas on an appropriate metal catalyst directs carbon nanofiber growth.[3] Covalent attachment of linker molecules to GCNF surface sites is accomplished by following the stepwise process shown in Scheme 1.

TEM micrographs of representative GCNF materials prepared in this study are displayed in Figure 5. As-prepared GCNFs have an average diameter of ca. 200 nm and

usually contain metal growth catalyst particles affixed to the nanofiber terminus, as shown in Figure 5a. Following oxidation by nitric acid, the resulting oxidized GCNFs have the same nanofiber morphology (Figure 5b), although acid etching removes any residual metal growth catalyst nanoparticles and any amorphous carbon by-product initially present in the as-prepared GCNFs. Surface derivatization with a linker molecule, such as ODA, also occurs with retention of overall nanofiber morphology (Figure 5c).

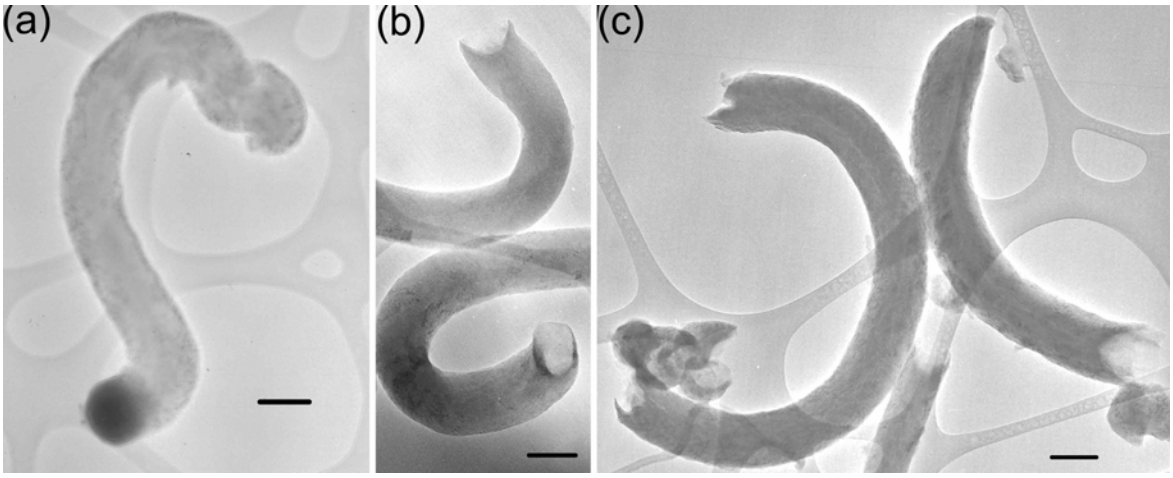

Figure 5. TEM micrographs of (a) as-prepared GCNFs, (b) oxidized GCNFs, and (c) GCNF/ODA nanofibers. Scale bar = 200 nm.

2.3.2 Qualitative Characterization of GCNF Materials

Infrared (IR) Spectra

Infrared spectra of as-prepared, oxidized, and the seven surface-derivatized GCNF materials described above are provided in Appendix C. Particularly noteworthy spectral features are discussed below.

Bands at 1579 and 1181 cm^{-1} observed in the IR spectra of as-prepared GCNFs correspond to C=C stretching and bending vibrations of the graphene backbone.[64] Intense peaks centered at ca. 3435 cm^{-1} are assigned to the presence of physically adsorbed water,[64] while weak bands at ca. 3000 cm^{-1} are assigned to C-H bond stretching vibrations arising from hydrogen-atom termination at carbon edge sites.[65]

IR spectra of oxidized GCNFs contain a similar band at 1578 cm^{-1} for C=C stretching, confirming that the nanofiber graphene backbone structure is unaffected by treatment with nitric acid, consistent with the TEM observations presented above. A new band appears at 1719 cm^{-1}, which is attributed to C=O stretching vibrations of surface carboxylic acid groups, as observed for acid-oxidized SWNTs.[54a]

Following surface acylation of oxidized GCNFs by thionyl chloride and amide condensation with an amine reagent, such as hexamethylenediamine, the IR C=O stretching band assigned to carboxylic acid groups is dramatically reduced in intensity, typically leaving only weak peaks in the carbonyl stretching region. Unfortunately, the expected carbonyl stretching band for surface-bound amide functional groups, which appears at 1616 cm^{-1} for SWNTs derivatized with octadecylamide groups,[54b,55a] overlaps with the intense graphene stretching band at 1578 cm^{-1}. IR spectra of the other six GCNF/linker molecule materials reveal similar reductions in intensity of the corresponding CO_2H carbonyl-stretching bands upon amidation, with no direct observation of amide carbonyl-stretching bands due to peak overlap.

Laser Desorption/Ionization Mass Spectra (LDI-MS) and Reaction with Butyl Glycidyl Ether

GCNF materials prepared in this study have been examined by LDI-MS to obtain direct evidence for the presence of covalently bound linker molecules. In this technique, laser irradiation (337 nm) on the GCNF matrix leads to direct desorption and ionization of surface analyte species along with ionized fragments of the carbon matrix.

LDI-MS spectra of as-prepared GCNFs, oxidized GCNFs, and the seven GCNF/linker molecule materials described herein along with the mass spectra of the corresponding pure amines used as linker molecules are provided in Appendix C. Parent ions and assignments of prominent fragment ions are identified on each mass spectrum.

Mass spectra of as-prepared and surface-oxidized GCNFs show few fragment ions at low m/z values. The mass spectrum of as-prepared GCNFs contains a base peak at 39 m/z and a peak of much lower intensity at 73 m/z. The peak at lower m/z is assigned to endogenous K^+ ion, while the fragment of higher mass is identified as the C_6H^+ carbon cluster. Carbon cluster ion formation is also observed in the mass spectra of carbon films.[66] Mass spectra of oxidized GCNFs contain a base peak for potassium ion along with a cascade of peaks assigned to C_4-C_{10} carbon cluster cations. A peak at 46 m/z is assigned to the formic acid ion, $[HCOOH]^+$, that could form during ionization of surface-bound CO_2H functional groups. Ions of other carbonaceous clusters containing undetermined numbers of oxygen and hydrogen atoms are also evident.

Comparison of the mass spectrum of each GCNF/linker molecule material with that

of the corresponding pure amine reveals a close match of parent ion, base peak, and main fragment ions within each pair of samples. While this correspondence is consistent with each linker molecule being uniquely present within a given GCNF/linker molecule material, direct confirmation of an amide functional group binding linker molecules to the GCNF surface is not observed by LDI-MS with the possible exception of the GCNF(TAPA) material. In addition, mass spectra of GCNF/linker molecule materials all show peaks at m/z values substantially greater than that of the corresponding pure amine. In most cases, these unidentified ions have masses sufficiently large to be assigned as non-covalent complexes between parent ions and prominent fragment species of the corresponding linker molecules. However, for the GCNF(TAPA) material, a mass spectral peak at 316 m/z is observed. This peak is only 26 amu greater than the mass of the neutral TAPA triamine (290 amu) and could be assigned to a cationic isocyanate species, such as $(O=C=N\text{-}TAPA)^+$, derived from a surface-bound TAPA-amido linker molecule (see Scheme 1).

As a control study, oxidized GCNFs were separately reacted with a representative aromatic (ODA) and aliphatic (HDA) diamine without thionyl chloride activation under the same reaction procedures reported above. LDI-MS spectra of the obtained product materials did not contain any ion fragments identifiable with the corresponding diamine reagents. This result confirms that intermediate reaction with thionyl chloride is necessary to observe linker molecule ionization and suggests that covalent amidation of linker molecules to GCNF surface sites is likely. Any linker molecules physisorbed or

associated with nanofibers through acid-base reactions do not survive the reaction and purification procedures.

To confirm the presence of a reactive, pendant amino group in a representative GCNF/linker molecule material, GCNF/ODA nanofibers have been reacted with neat butyl glycidyl ether (BGE). The LDI-MS spectrum of the nanofiber product material, as recorded in negative-ion mode, is shown in Figure 6. Surprisingly, the base peak at 228 m/z can now be assigned to the protonated form of the expected ODA-amide linker molecule formed by covalent amide condensation of ODA with a surface-bound acid chloride functional group. In addition, a pattern of three peaks of decreasing intensity at m/z values of 358, 488, and 618 is observed in which each peak is separated by the mass of one butyl glycidyl ether monomer (130 amu). This spectrum indicates that this product is best described as GCNF/ODA$(BGE)_n$, in which the amino terminus of surface-bound ODA linker molecules initiates nucleophilic ring-opening of BGE monomers to covalently extend the linker molecule structure by at least a three-epoxy oligomeric unit. Thus, the presence of an amide-bound linker molecule containing a reactive pendant amino functional group in the GCNF/ODA material can be inferred.

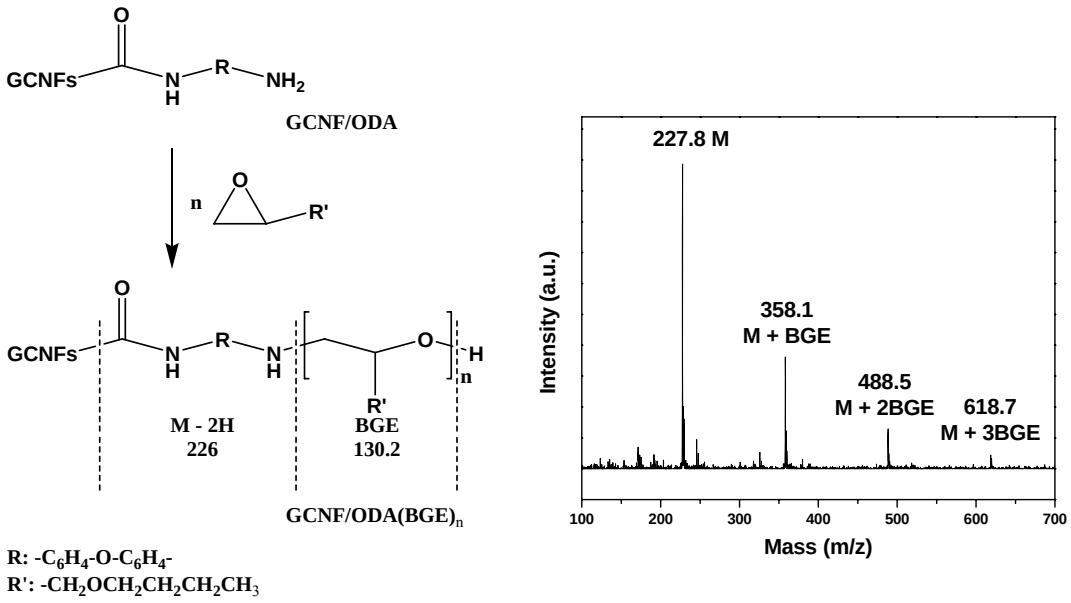

Figure 6. LDI mass spectrum of GCNF/ODA(BGE)$_n$ and assignment of important peaks.

X-ray Photoelectronic Spectroscopy (XPS)

Additional evidence supporting covalent binding of the seven linker molecules investigated in this study to GCNFs has been obtained using a known XPS analysis technique for identifying surface amine functional groups.[67,68] In this method, surface amino groups are quantitatively acylated by reaction with trifluoroacetic anhydride (TFAA) to form the corresponding trifluoroacetamide (Scheme 5). A representative XPS spectrum for the trifluoroacetylated GCNF/ODA material is shown in Figure 7. The F/N atomic ratio of the product material can then be theoretically calculated based on the expected product formula (column 2 in Table 1 for pure amine, right column in Scheme 5 and columns 4 and 5 in Table 1 for GCNF/linker molecules). Also the F/N ratio can be spectroscopically determined from the relative intensities of the N 1s (400 eV) and F 1s

(689 eV) XPS peaks corrected to a standard sample (column 6 in Table 1). Surface nitrogen atoms present as amides will contribute to the N 1s XPS peak intensity but will not react with TFAA. Therefore, the relative number of amino and amido N atoms present within each diamine or triamine (either as a free molecule or as a linker molecule) can be obtained from F/N atomic ratios experimentally determined by XPS. Control experiments confirm that as-prepared and surface-oxidized GCNFs do not react with TFAA to produce a detectable F 1s peak.

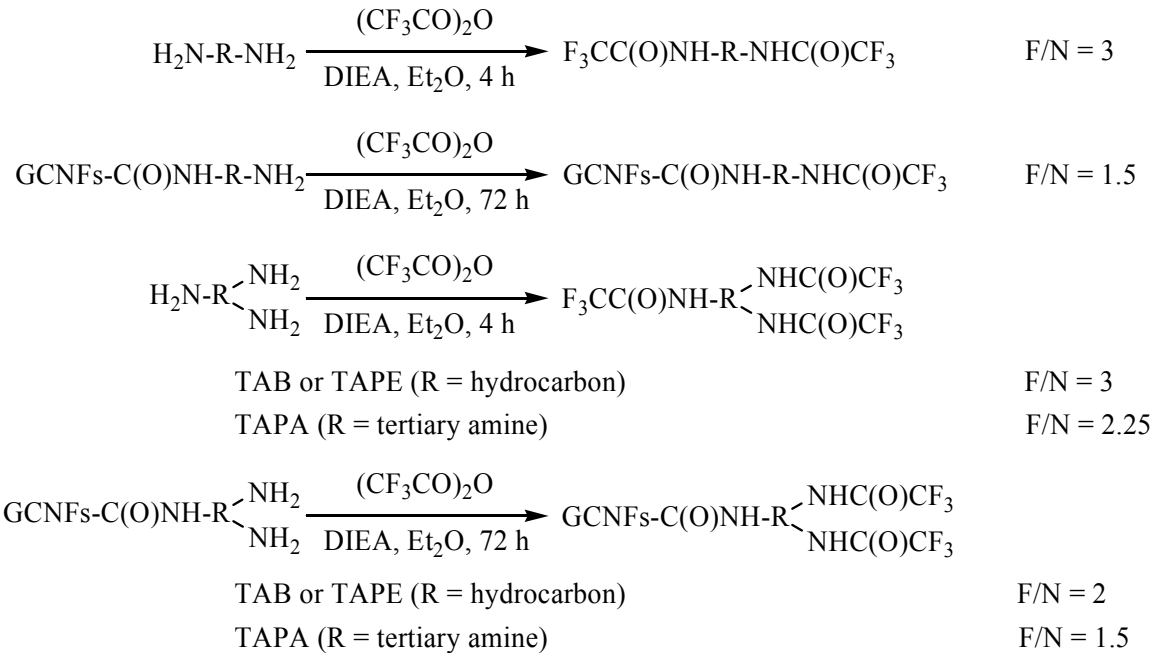

Scheme 5. Reaction of free and surface-bound diamines (HDA, XDA, PDA and ODA) or triamines (TAPA, TAB and TAPE) with TFAA showing the F/N atomic ratios of expected products.

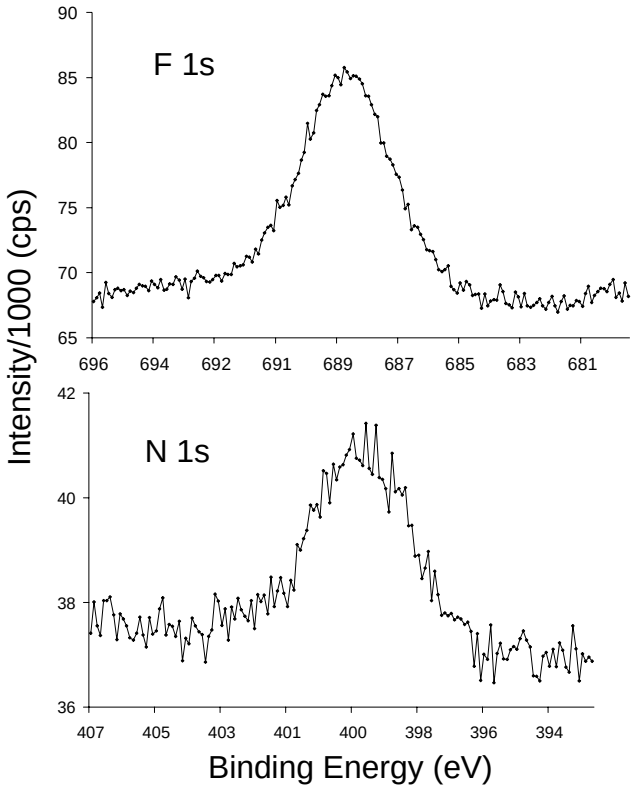

Figure 7. XPS spectra of GCNF/ODA[$C(O)CF_3$] samples (F 1s and N 1s regions).

For the four GCNF/diamine (HDA, XDA, PDA, and ODA) materials, the experimental F/N atomic ratios, as shown in Table 1, are within one standard deviation of values predicted from the structures shown in Scheme 1 based on monodentate surface attachment via amidation.

For the three GCNF/triamine (TAB, TAPA, and TAPE) materials, two different binding modes are evident. The TAPA and TAB linkers give F/N atomic ratios consistent with the monodentate surface-amidation structure depicted in Scheme 1. However, the largest triamine, TAPE, has a F/N atomic ratio consistent only with bidentate surface-amide attachment to GCNF surface sites. This binding mode would be expected

in those cases where (1) a sterically bulky, pyramidal triamine adopts orientations that places a second amino group within proximity to the GCNF surface, and (2) when the number density of surface acid chloride groups is relatively high (*vide infra*). XPS analysis of these trifluoroacetylated GCNF/linker molecule materials strongly supports covalent surface attachment through amide condensation reactions and excludes other structural possibilities, such as linker molecule physisorption or intercalation.

Table 1. Calculated F/N ratios of pure amines and of functionalized GCNFs assuming complete amidation of free amine groups by reaction with TFAA for either mono- or bidentate GCNF surface binding compared to experimental F/N ratios

Pure amine	F/N[a]	GCNF/linker material	F/N[a] (monodentate binding)	F/N[a] (bidentate binding)	F/N[b] (observed)
HDA	3	GCNF/HDA	1.5	0	1.7 ± 0.3
XDA	3	GCNF/XDA	1.5	0	1.2 ± 0.3
PDA	3	GCNF/PDA	1.5	0	1.5 ± 0.2
ODA	3	GCNF/ODA	1.5	0	1.7 ± 0.4
TAPA	2.25	GCNF/TAPA	1.5	0.75	1.5 ± 0.3
TAB	3	GCNF/TAB	2	1	2.4 ± 0.3
TAPE	3	GCNF/TAPE	2	1	1.2 ± 0.3

[a] Calculated values. [b] As determined from XPS F 1s and N 1s standardized peak areas.

2.3.3 Quantitative Characterization of GCNF Materials

Derivation of approximate compositions for the GCNF materials prepared in this study has been attempted using a variety of quantitative analysis methods including bulk elemental analysis, acid and base-uptake measurements, three methods for amino group analysis, and TGA. TGA traces for as-prepared GCNFs, oxidized GCNFs, and for the seven GCNF/linker molecule materials reported herein are provided in Appendix C, although the interpretation of these TGA curves is complicated by overlapping mass-loss events. Chemical compositions proposed for the GCNF materials reported in this study are only approximate and have been formulated under the following assumptions: (1) suggested compositions must be consistent with bulk elemental analysis data, (2) ΔpH measurements are reliable for quantifying acidic and basic sites, (3) Fmoc analysis is reliable for the quantification of nucleophilic amino groups, and, (4) TGA mass-loss events provide only semi-quantitative information about composition.

As-prepared GCNFs have the empirical formula, $C_{580}H_{21}O$, based on bulk elemental analysis (excluding residual metal growth catalyst). TGA reveals a total mass loss of 0.25 wt% from room temperature to 125 °C, consistent with desorption of physisorbed water. Assuming that IR bands near 3000 cm^{-1} can be assigned to C-H bond stretching vibrations, the proposed composition for as-prepared GCNFs is $C_{580}H_{19}(H_2O)$.

Oxidized GCNFs have an empirical formula of $C_{460}H_{32.5}NO_{50}$ based on bulk elemental analysis. Acid-uptake measurements indicated the presence of strong acid sites (6.92×10^{-5} mol/g), while base-uptake data give a total acid site content of 5.20×10^{-4}

mol/g and a calculated weak acid component of 4.51×10^{-4} mol/g. Assuming that strong acid sites are various N-O-H species best represented compositionally as HNO_3, that the remaining N content is present as NO_2 groups, and that weak acid species can be represented as CO_2H, a composition of $C_{914}H_{58}O_{82}(NO_2)(HNO_3)(COOH)_6$ is suggested. Nitric acid intercalates into graphite and carbon nanotubes and might do likewise with GCNFs.[69] TGA shows a 4 wt% total mass loss from room temperature to 100 °C that is assigned to loss of physisorbed water and HNO_3, giving a final suggested composition of $C_{914}H_{10}O_{58}(NO_2)(HNO_3)(COOH)_6(H_2O)_{24}$. Other O-containing species likely present in oxidized GCNFs include aldehyde, ketone, anhydride, or phenolic functional groups.[64,65]

The above results can be compared to related oxidized carbon nanostructured materials. For vapor-grown carbon nanofibers, nitric acid oxidation gives 7.57×10^{-5} mol/g of surface acid groups,[57a] which is about one sixth of carboxylic acid content of oxidized herringbone GCNFs. For multi-walled carbon nanotubes of diameter 20-25 nm, nitric acid oxidation gives 2.7×10^{-3} mol/g of surface acid groups,[56c] which corresponds to about 67% of the acid group content determined for oxidized herringbone GCNFs used in this study, when normalized to the same average diameter. The higher normalized acid content achieved for herringbone GCNFs is consistent with the unique structure of these nanofibers.

Amino group contents have been determined with three analysis methods (Schemes 2-4). All methods depend on the coupling reaction of surface amino groups with chromophore groups and the cleavage of the chromophore for absorption measurements.

However, it is challenging to determine the contents of surface amino group due to the steric effects and poor swelling capability of GCNF materials and the reduced reactivity of surface organic groups. From the analysis results as shown in Figure 8, the Fmoc method yields the highest results for all seven GCNF/linker molecule materials, which is reasonable considering the long aliphatic chain between the carboxylic acid group and the bulky fluorenyl group in the Fmoc reagent (Scheme 4).

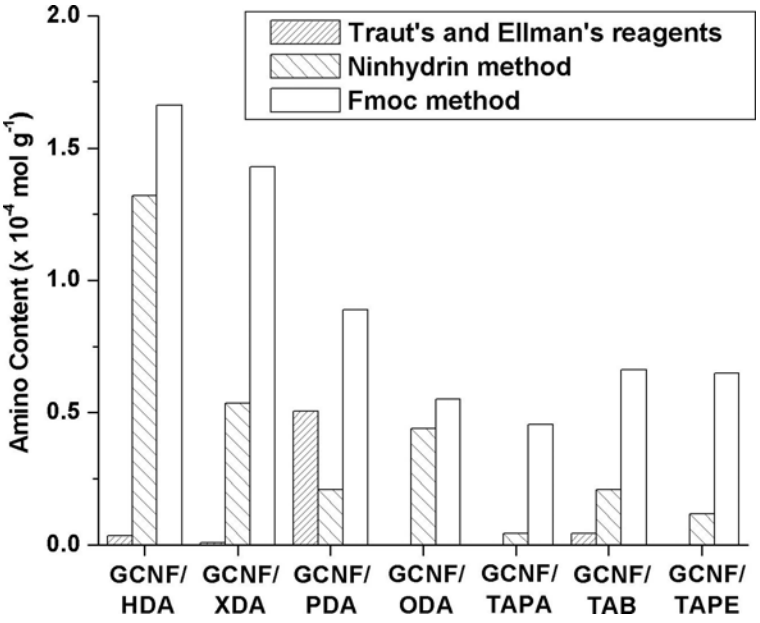

Figure 8. Amino group contents determined from three quantitative analysis methods. Note that results for GCNF/ODA, GCNF/TAPA, and GCNF/TAPE using Traut's and Ellman's reagents are not available.

Approximate chemical compositions derived for the seven GCNF/linker molecule materials prepared in this study are provided in Table 2. Since amidation reactions are conducted under strongly basic and moderately reducing conditions (neat amine at

elevated temperature), any HNO_3, nitrogen oxide or chemically equivalent functional groups present in the oxidized GCNFs will be removed or reduced. Acid-uptake data is used to quantify the number density of proton basic sites, and Fmoc analysis data is used to quantify the number density of nucleophilic primary amino sites.

Table 2. Quantitative compositional data for GCNF/linker molecule materials

GCNF/linker material	Composition by bulk EA	Basic sites[a] (mol/g) × 10^4	Fmoc-reactive sites[b] (mol/g) × 10^4	Fraction of basic[c] NH_2 (%)	Fraction of Fmoc-reactive[d] NH_2 (%)
GCNF/HDA	$C_{80}H_5$[C(O)HDA]	8.2	1.7	98	20
GCNF/XDA	$C_{42}H_{23}$[C(O)XDA]	12	1.4	84	10
GCNF/PDA	$C_{43}H_3$[C(O)PDA]	1.4	0.89	10	6
GCNF/ODA	$C_{82}H_4$[C(O)ODA]	0.43	0.55	6	7
GCNF/TAPA	$C_{103}H_6$[C(O)TAPA]	2.2	0.45	18	4
GCNF/TAB	$C_{106}H_4$[C(O)TAB]	1.8	0.66	16	6
GCNF/TAPE	$C_{144}H_3$[C(O)TAPE]	0.80	0.65	10	8

[a] Basic sites are calculated from acid-uptake measurements (average esd is 3.3%). [b] Fmoc-reactive sites are calculated from Fmoc analysis (average esd is 3.7%). [c] Fraction of basic sites is the ratio of experimental basic sites to the total amine groups expected from nitrogen elemental analysis. It is assumed there is one amine group for surface-bound diamine molecules and two for triamine molecules. [d] Fraction of Fmoc-reactive sites is the ratio of experimental Fmoc-reactive sites to the total amine groups expected from nitrogen elemental analysis.

Comparison of calculated chemical compositions based only on acid uptake and Fmoc analysis data with the chemical compositions derived from bulk elemental analysis data gives estimates for the percentages of pendant, primary amino groups, which are assumed to be present within the sample and reactive to protonation or to electrophilic attack by the Fmoc reagent. Due to the vast structural variety of local site environments probably present within GCNF materials, it is likely that some fraction of surface-bound linker molecules might have all available amino groups bound to the GCNF surface as amides or might have pendant, primary amino groups in local environments unsuitable for protonation by aqueous acid or for nucleophilic attack by the Fmoc reagent.

Overall chemical compositions range from a relatively high incorporation of linker molecule for XDA and PDA (1 linker molecule for every ca. 40 GCNF carbon atoms) to relatively low incorporation for TAPE (1 TAPE linker molecule for every ca. 150 GCNF carbon atoms). Based on BET surface area of oxidized GCNFs (138 m^2/g), linker molecule coverage is calculated to be 0.12 nm^2 per XDA or PDA molecule and 0.40 nm^2 per TAPE molecule. The percentage of pendant, primary amino groups assumed to be present that can be protonated ranges from nearly 100% for the aliphatic diamines HDA and XDA to only 6% for the aromatic diamine ODA. Likewise, the percentage of pendant, primary amino groups assumed to react as nucleophiles with the Fmoc reagent ranges from 20% for HDA to only 4% for the triamine TAPA. Although rationalizing these different degrees of chemical reactivity is complicated by batch-to-batch variability of GCNF surface structure and degree of surface-site oxidation, these results provide useful

comparisons of relative linker-molecule reactivity to aid in the selection of GCNF/linker molecular materials for future applications.

Quantification of the surface density of linker molecule binding is complicated by not knowing the precise surface structure of herringbone GCNFs. Surface areas measured for as-prepared herringbone GCNFs (107 m^2/g) and oxidized GCNFs (138 m^2/g) show an increase in nanofiber surface area due to oxidative etching of metal growth catalyst particles and the removal of amorphous carbon present within as-prepared GCNFs. From the compositional data shown in Table 2, the average linker molecule content of these seven GCNF/linker molecule materials is one linker molecule/86 GCNF carbon atoms. Knowing the surface area of oxidized GCNFs, the calculated average surface coverage per linker molecules is 0.24 nm^2. Relative to an edge-site atom surface coverage in graphite of ca. 0.08 nm^2 per carbon atom, approximately one-third of the available GCNF edge sites are apparently derivatized with linker molecules. With a linker molecule surface density this high, a GCNF of 200 nm average diameter will have nearly one thousand linker molecules attached to each graphene layer. GCNF/linker molecule materials might be attractive as reactive strengthening additives for composite materials, because the structural features providing strengthening are individual graphene layers within the nanofiber and not GCNFs as a whole. Work exploring the use of GCNF/linker molecule materials as additives for the fabrication of GCNF/polymer composite materials is presented in Chapter III.

2.4 Conclusions

Surface carbon sites of as-prepared GCNFs are oxidized to carboxylic acid groups by nitric acid and covalently bound to seven different linker molecules containing pendant amino groups using carboxylate amidation chemistry. GCNF materials are characterized by TEM, IR, TGA, laser-desorption/ionization (LDI) mass spectrometry, and by elemental analysis. Approximate GCNF/(linker molecule)$_x$ compositions are proposed consistent with acid-uptake and elemental analysis data. Direct evidence for the presence and composition of surface-bound linker molecules is provided by LDI mass spectrometry and by quantitative XPS analysis of trifluoroacetylated derivatives. The reactivity of pendant amino groups present within attached linker molecules is determined quantitatively via Fmoc analysis and synthetically by effecting nucleophilic ring-opening oligomerization of epoxy monomer.

CHAPTER III

FABRICATION AND MECHANICAL CHARACTERIZATION OF GCNF/POLYMER NANOCOMPOSITES[46-49]

3.1 Introduction

A number of carbon nanofiber/polymer composites have been reported,[70-76] mainly with thermoplastic polymer matrixes, such as polypropylene,[70] nylon,[72,76] poly(methyl methacrylate)[74] and poly(ether ether ketone).[75] Typical nanofiber loadings range from 5 wt% to 40 wt%. Studies on such composite materials at much lower fiber loading (< 5 wt%) would be valuable to obtain enhanced properties at lower cost. Unfortunately, carbon nanofiber/polymer composites of such low loadings do not generally show increased mechanical strength[73-75] and even exhibit reduced tensile strength.[70] Mechanical failure for those samples has been attributed to poor wetting at the nanofiber surface and to difficulties in obtaining good dispersion of the nanofiber reinforcement additives throughout the polymer matrix.

Fiber-matrix interfacial adhesion plays an important role on the mechanical properties of nanofiber/polymer composites. Stronger interfacial bonding imparts high degrees of nanofiber wettability and dispersibility and enhances mechanical and other properties of the resulting nanocomposite materials. While chemical modification of carbon fiber surfaces has been used to augment fiber/polymer attractive interactions, there have been few reports of GCNF surface modification designed to achieve covalent bonding across the GCNF/polymer interface.

This chapter will report the preparation of GCNF/epoxy nanocomposites by curing

epoxy resin with surface-functionalized herringbone GCNFs containing reactive linker molecules, which bear pendant primary amino functional groups capable of binding covalently to epoxy resins[45,77]. Scheme 6 shows the preparation of the most used bisphenol A based epoxy resins, which are mixture of linear oligomers produced by glycidation of bisphenol A with epichlorohydrin. During thermal curing, the linear oligomers are cross-linked into a three-dimensional infusible network, mostly by epoxide ring opening with curing agents, such as polyamines and polyphenols.

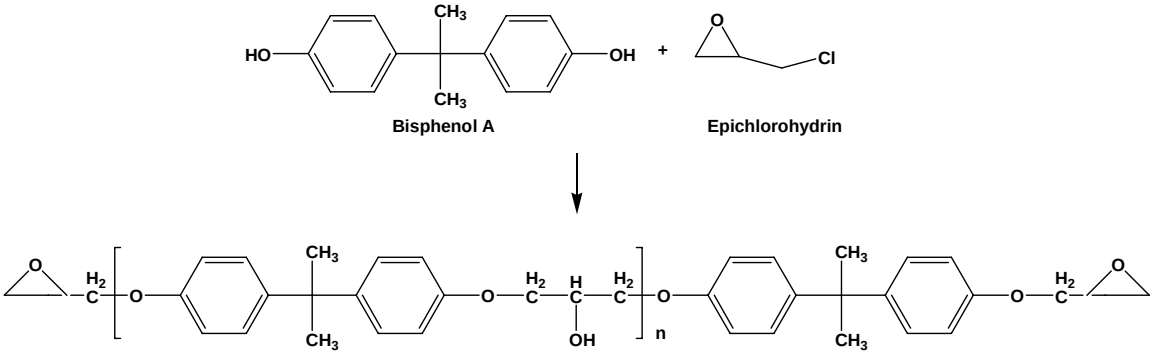

Scheme 6. Synthesis of glycidated epoxy resins.

As discussed in Chapter II, 3,4'-oxydianiline-derivatized GCNFs (GCNF/ODA) are found to react with neat butyl glycidyl ether (BGE) to form mono-, di-, or tri-glycidyl oligomers covalently bonded to the ODA pendant amino groups on GCNF surfaces. The resulting GCNF/ODA$(BGE)_n$ nanofibers, with hydroxyl groups on the free end of the extended linker molecules, are more reactive for covalent incorporation into epoxy resins during thermal curing through curing-agent-like nucleophilic attack of the terminal

hydroxyl group onto the epoxide ring. Key steps in the fabrication of GCNF/epoxy specimens include: (1) the preparation of GCNF/ODA nanofibers, (2) sonication of GCNF/ODA nanofibers in neat butyl glycidyl ether, which yields a liquid blend of GCNF/ODA and BGE containing shortened GCNFs with extended linker molecules, GCNF/ODA(BGE)$_n$, and (3) dispersion of GCNF/ODA/BGE blend into epoxy resin followed by thermal curing. This chapter focuses on the fabrication of GCNF/epoxy nanocomposites with nanofiber loadings ranging from 0.15 wt% to 1.3 wt%, and three-point bending tests, which demonstrate ca. 26% enhancement of flexural strength and 31% enhancement of breaking strain for GCNF/epoxy nanocomposite with 0.3 wt% GCNF addition over pure epoxy specimens.

3.2 Experimental Section

3.2.1 General Procedures

A Philips CM20 TEM was used to observe the sample structures. A Hitachi S-4200 SEM was used to observe the fracture surface morphology of samples after specimen breaking. Three-point bending tests were conducted on a MTS 880 testing machine following ASTM D790-00 (Standard test methods for flexural properties of unreinforced and reinforced plastics and electrical insulating materials). At least five specimens were tested for each sample. The size of rectangular specimens were 70.0 ± 0.5 mm (length) × 12.5 ± 0.3 mm (width) × 3.0 ± 0.2 mm (thickness). The loading rate was 1 mm/min.

3.2.2 Preparation of GCNF/ODA/BGE Blend and GCNF/Epoxy Nanocomposites

GCNF/ODA was prepared by surface oxidation of GCNFs with nitric acid and by functionalization with 3,4'-oxydianiline as described in Chapter II. Then GCNF/ODA/BGE liquid blend was prepared by sonicating GCNF/ODA powders in butyl glycidyl ether (BGE) with a digital sonifier (Branson Ultrasonics, Model 450) at power level of 70 watts for 60 min at 0 ^{o}C. In this study, the weight ratio of nanofiber to BGE diluent was maintained at 1:6.

Commercial liquid bisphenol A based epoxy resin, Epon 828 (Miller-Stepheson) with a viscosity of 110-150 poise was used for composite preparation, and borontrifluoride-monoethylamine ($EtNH_2 \cdot BF_3$, Aldrich) was used as curing agent (2.75 wt%). GCNF/epoxy hybrid specimens were prepared and tested mechanically by Dr. W. Katie Zhong using the following procedure. The epoxy resin and curing agent were mixed at 90 ^{o}C, and then an appropriate amount of GCNF/ODA/BGE blend was added and mixed by low-power sonication for 3 h with an ultrasonic cleaner (Branson Ultrasonics, Model 1210). After sonication, each sample was cast into a mold, and then cured under vacuum with the following curing cycle: 120 ^{o}C for 1 h, then 140 ^{o}C for 1.5 h, and 150 ^{o}C for 1.5 h. After cooling down to room temperature, sample specimens were taken out of the mold. Nanocomposite specimens with five different fiber loadings of 0.15 wt%, 0.2 wt%, 0.3 wt%, 0.5 wt% and 1.3 wt% were prepared. Accordingly, the contents of butyl glycidyl ether in the GCNF/epoxy nanocomposite specimens were 0.9 wt%, 1.2 wt%, 1.8 wt%, 3.0 wt% and 7.8 wt%.

3.3 Results and Discussion

3.3.1 Sonication of GCNF/ODA in BGE

Sonication of a mixture of herringbone GCNF/ODA nanofibers in neat BGE diluent affords a GCNF/ODA/BGE liquid blend, containing GCNF/ODA$(BGE)_n$ and excess BGE, with a uniform black appearance. As shown in Figure 9, most of the nanofibers have been shortened in length to well below one micron. As discussed in Chapter II, LDI-MS analysis of GCNF/ODA$(BGE)_n$ nanofibers has revealed the attachment of up to three butyl glycidyl monomers onto the ODA terminal amino groups on the surface of GCNF/ODA nanofibers, giving extended linker molecules. While dry GCNF/ODA nanofibers tend to aggregate due to strong π-π interactions, the sonicated GCNF/ODA/BGE blend is relatively stable. The nanofiber/diluent blend was then used in the preparation of GCNF/epoxy monolith specimens.

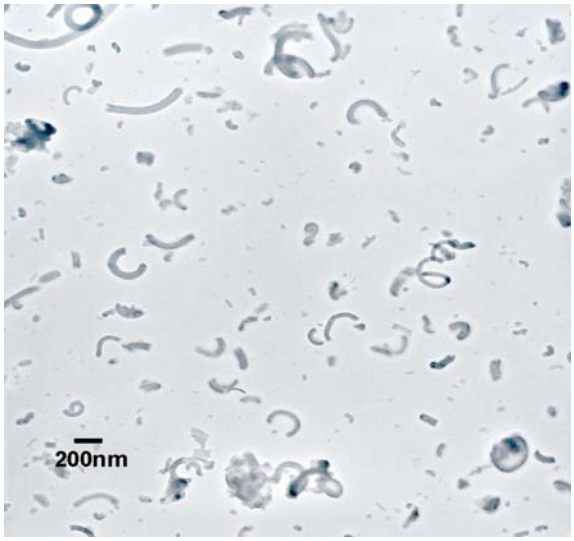

Figure 9. TEM image of GCNF/ODA/BGE blend.

3.3.2 Flexural Property of GCNF/Epoxy Nanocomposites

Specimens of GCNF/epoxy nanocomposites with fiber loadings of 0.15 wt%, 0.2 wt%, 0.3 wt%, 0.5 wt% and 1.3 wt% were prepared by mixing appropriate amounts of GCNF/ODA/BGE blend in epoxy resin followed by thermal curing. The flexural properties of cured GCNF/epoxy nanocomposites were examined through three-point bending tests.

Figure 10 shows typical flexural stress-strain curves. From the values at breaking points, the breaking strain of the GCNF/epoxy nanocomposites with 0.3 wt% of GCNF/ODA is increased by 31% in comparison to that of the pure epoxy specimen (from 0.052±0.004 to 0.068±0.005). This indicates that specimen toughness (energy to failure) has been much improved with the addition of only 0.3 wt% of GCNF/ODA nanofibers.

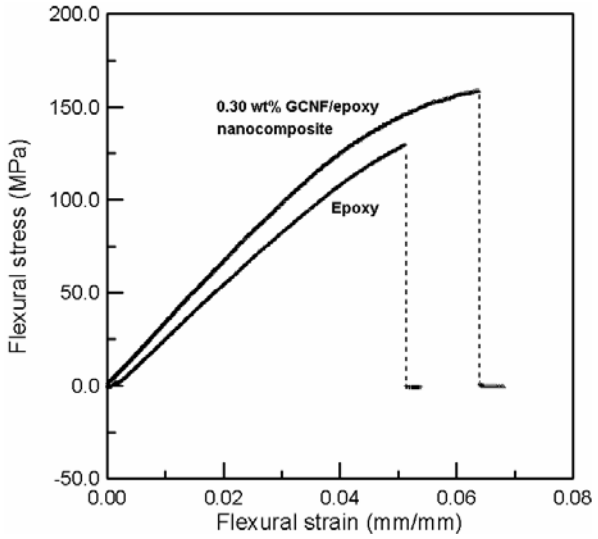

Figure 10. Flexural stress-strain curves of cured epoxy resin and of GCNF/epoxy nanocomposite with 0.3 wt% GCNF/ODA nanofibers. Dashed lines are added before and after sample breaking for easy viewing.

Testing results of flexural strength for pure epoxy specimens and for five GCNF/epoxy nanocomposites are shown in Figure 11. Flexural strength of epoxy specimens increases with nanofiber addition from 132.2 ± 1.5 MPa for pure epoxy to 166.4 ± 2.0 MPa for 0.30 wt% GCNF/epoxy nanocomposite. However, the flexural strengths of nanocomposites decrease at higher fiber loading to 150.7 ± 5.6 MPa for a 1.3 wt% GCNF/epoxy nanocomposite. Compared to the flexural strength of a pure epoxy control sample, the flexural strength of GCNF/epoxy nanocomposite specimens reach a maximum value at 0.3 wt% nanofiber loading, which corresponds to a 26% strength enhancement.

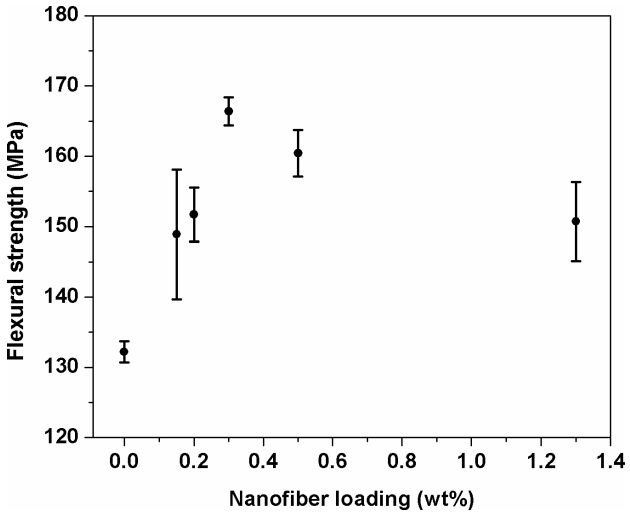

Figure 11. Flexural strength of pure epoxy and GCNF/epoxy nanocomposites.

As discussed earlier, epoxy resins are mixtures of linear oligomers with two terminal epoxide rings. Curing of epoxy resins, mainly by ring-opening polymerization of epoxide rings with curing agents, transforms epoxy resins into three-dimensional thermosetting materials.

Reactive hydroxyl groups are present at the end of butyl glycidyl oligomers on the surface of GCNF/ODA(BGE)$_n$ product, which may react with epoxide rings in the same way as curing agents normally do. With a large number of linker molecules attached to each graphene layer of carbon nanofibers, the covalent bonding between nanofibers and epoxy resin will be secured, which ensures an effective load transfer.

The diluent used in this research, butyl glycidyl ether (BGE), has been widely used as diluent in epoxy curing,[78] because it also contains an epoxide ring at one end, similar to the structure of epoxy resin. The basic function of a diluent during epoxy resin curing

is to reduce the viscosity of the resin and manipulate the degree of cross-linking. In this study, there is one more reason to use this diluent: the diluent was used as a dispersing agent for shortening the nanofibers with high-power sonication. With sonication, GCNF/ODA nanofibers are shortened and reacted with the epoxide ring of the BGE diluent, which forms extended linker molecules on the GCNF surface (Figure 6 in Chapter II). Given that GCNF/ODA nanofibers easily aggregate together in dry form, the GCNF/ODA/BGE blend was prepared and directly used for making the nanocomposites.

Flexural properties do not show a linear increase with increasing nanofiber loadings as predicted by the rule of mixtures, since the blend of GCNF/ODA nanofibers and the diluent causes two competitive effects. The reinforcement of the GCNF/ODA could function well for an epoxy matrix based on well dispersion and chemically interfacial bonding with the epoxy. Therefore, addition of nanofibers could greatly enhance mechanical properties. The diluent could prevent the nanofiber aggregation that might occur. However, higher amounts of diluent molecules would decrease the mechanical properties of the epoxy matrix since the density of cross-linking is lower. Because the weight ratio of the nanofibers to diluent can not be lower than 1:6 during sonication for an effective dispersion, there is a large amount of diluent remaining in the blend after oligomerization of some BGE monomers onto the GCNF surface. For the nanocomposites with nanofiber loadings of 0.15 wt%, 0.20 wt% and 0.30 wt%, the contents of the diluent are 0.9 wt%, 1.2 wt% and 1.8 wt%, respectively, so that the reinforcement of the nanofibers is a dominant effect. When the content of the diluent is

increased further, the effect caused by the diluent on the mechanical property will be more dominant. For the nanocomposites with nanofiber loadings of 0.5 wt% and 1.3 wt%, the contents of diluent in these two samples are 3.0 wt% and 7.8 wt%, which leads to a partial strength reduction. Therefore, the nanocomposite reinforced by 0.3 wt% of nanofibers has the best flexural property.

3.3.3 Observation of Specimen Fracture Surface Morphology

After bending tests, the fracture surface of GCNF/epoxy nanocomposite specimens was observed for better understanding on the role of sonication of GCNF/ODA powders in BGE diluent. The fracture surface of the control sample, made with curing of an epoxy resin containing dry GCNF/ODA nanofibers, shows large GCNF aggregates with size of 1-2 μm (Figure 12a). On the contrary, fracture surface of the GCNF/epoxy nanocomposite, made with epoxy resin and the GCNF/ODA/BGE blend, shows GCNF additives with sizes of 200-400 nm (Figure 12b). The image also displays improved wettability of GCNFs and superior incorporation of GCNFs within the epoxy matrix. It appears that the reactive pendant functional groups present on the surface of the GCNF/ODA nanofibers have been covalently incorporated into the epoxy matrix, leading to stronger nanofiber/matrix bonding and to enhanced flexural strength.

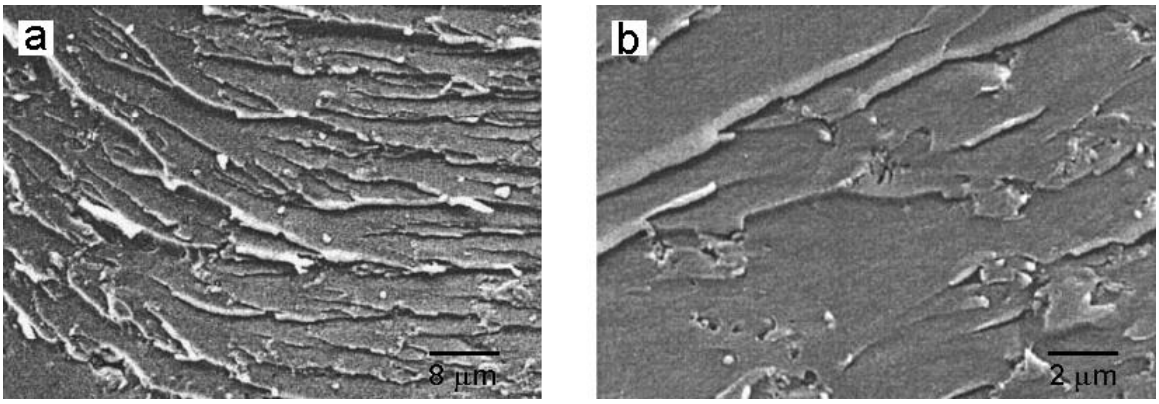

Figure 12. SEM images of GCNF/epoxy nanocomposites prepared with (a) dry GCNF/ODA nanofibers and (b) with GCNF/ODA/diluent blend.

3.4 Conclusions

Epoxy nanocomposites reinforced by GCNF/ODA nanofibers, prepared from a blend of GCNF/ODA and BGE diluent with high-power sonication, and by thermal curing of a commercial epoxy resin with the resulting GCNF/ODA/BGE blend, were mechanically examined with three-point bending tests. The nanocomposite containing 0.3 wt% of GCNF/ODA nanofibers exhibits the highest mechanical properties, that is, 26% enhancement of flexural strength and 31% enhancement of breaking strain, compared to those of a pure epoxy sample. SEM images show improved interactions between GCNFs and the epoxy matrix, which is in agreement with our initial hypothesis of strong chemical bonding developed between GCNF/ODA nanofibers and epoxy resin during the curing process.

CHAPTER IV

PREPARATION OF GCNF/CERAMIC XEROGEL NANOCOMPOSITES

4.1 Introduction

Various ceramic-based composites containing traditional micron-scale carbon fibers,[79] single-walled carbon nanotubes (SWNTs),[80] or multi-walled carbon nanotubes (MWNTs)[81] as additives have been prepared. The mechanical and electrical properties of many such carbon/ceramic composites have been determined. While the presence of carbon fiber additives can enhance the strength and electrical conductivity of carbon fiber/ceramic composites, there remains a generally recognized problem of how to achieve excellent wetting of the hydrophobic carbon fiber surface by the polar ceramic matrix.[82] Successful formation of carbon/ceramic composites on the bulk scale has been thwarted by an inability to sufficiently wet and disperse carbonaceous additives within a desired ceramic matrix.

The Lukehart group has reported the preparation of GCNF/polyimide thin-film composites by thermal condensation and curing of polyamic acid resins in the presence of GCNFs containing pendant, reactive primary amino groups.[77] Intimate contact at the GCNF/polymer interface is observed due to covalent attachment of linker molecules to each phase. With a similar strategy, it was reported in Chapter II the preparation of GCNF/epoxy resin composites with diamine linker molecules and enhanced mechanical

properties.

This chapter reports an extension of this synthesis pathway to the formation of GCNF/silica xerogel composites using sol-gel processing. Co-hydrolysis and condensation of tetramethoxysilane in the presence of GCNFs surface-derivatized with sol-gel reactive 3-amidopropylsilyl functional groups affords a high degree of covalent binding across the GCNF/ceramic interface on the nanoscale. To our knowledge, this is the first report of successful covalent incorporation of herringbone GCNFs into a silica gel matrix. Given the ready availability of GCNFs, further development of this synthesis strategy for the preparation of GCNF/ceramic hybrid materials having desirable mechanical or electrical properties appears to be warranted.

4.2 Experimental Section

4.2.1 General Methods

Solvents were distilled prior to use. All gaseous reagents were obtained from Air Liquide Gas. 3-Aminopropyl triethoxysilane (APTES) and tetramethoxysilane (TMOS) were purchased from Aldrich Chemical Company, Inc. Other reagents were reagent grade and were used as obtained.

Sonication of sample dispersions was accomplished using a Branson Ultrasonic Cleaner (Model 1210R-DTH). Scanning electron microscopy (SEM) was performed on a Hitachi S-4200 Electron Microscope with an accelerating voltage at 5 or 10 kV. Powder

samples were placed onto double-sided carbon tape on the SEM sample holder and were sputtered with gold to avoid sample charging. Infrared spectra (IR) were recorded on a ATI Mattson Genesis Series FTIR spectrometer using KBr pressed pellet samples.

Thermogravimetric analyses (TGA) were performed on a Thermal Analysis Instruments High-Resolution TGA 2950 Thermogravimetric Analyzer with a heating rate of 15 ^{o}C min^{-1} in an atmosphere of nitrogen. Bulk elemental analysis was performed by Galbraith Laboratories, Inc., Knoxville, TN.

4.2.2 Preparation of GCNFs Containing Surface-Bound 3-Amidopropylsilyl Groups, GCNF-$[C(O)NH(CH_2)_3Si(OEt)(OH)_2]_x$, **1**.

Herringbone GCNFs were prepared and surface-modified with acid chloride functional groups, C(O)Cl, as described in Chapter II. Surface-acylated carbon nanofibers (1.2 g) were treated with 10 mL of neat 3-aminopropyl triethoxysilane. Reaction occurred when this mixture was heated to 100 °C under a nitrogen atmosphere for 96 h. The resulting suspension was cooled to room temperature and was filtered through a sintered-glass frit under nitrogen. The resulting GCNF-$[C(O)NH(CH_2)_3Si(OEt)(OH)_2]_x$ product, **1** (1.1 g), was isolated as a dry, black powder and was stored in a vial under nitrogen. Anal. Found: C, 80.08; H, 1.83; N, 1.81; Si, 3.90.

4.2.3 Synthesis of GCNF/Silica Xerogel Composite Materials Containing Surface-Bound 3-Amidopropylsilyl Linker Molecules, GCNF-[C(O)NH$(CH_2)_3$Si≡]$_x$/SiO_2 Xerogel, **2**, by Sol-Gel Processing

GCNF/silica xerogel samples were prepared at low and high carbon nanofiber loadings, **2a** and **2b**, respectively (Scheme 7). Appropriate masses of surface-modified GCNFs, **1**, 0.036 g (for **2a**) or 0.236 g (for **2b**) were mixed with 8 mL of methanol, 1.2 mL of water, and 1 mL of TMOS. The resulting mixture was sonicated for 5 min to disperse the carbon nanofibers throughout the liquid phase. To this mixture was added 0.05 mL of 0.15 M aqueous ammonia, and the suspension was further sonicated for 5 min. Gelation occurred at room temperature over 24 h. The xerogel product was washed with methanol followed by drying at 105 °C for 15 min to give the GCNF-[C(O)NH$(CH_2)_3$Si≡]$_x$/SiO_2 xerogel products, **2a** and **2b**, as dry, black powders. Elemental analysis indicated carbon contents of 6.8 and 46.8 wt% for products **2a** and **2b**, respectively.

4.2.4 Synthesis of GCNF/Silica Xerogel Composites Lacking Linker Molecules, GCNF/SiO_2 Xerogel, **3**, by Sol-Gel Processing

GCNF/silica xerogel samples were prepared using herringbone GCNFs without surface modification as control samples to better demonstrate the effect of surface modification. GCNF/silica xerogel composites of similar carbon nanofiber loadings, **3a** and **3b**, respectively, were prepared using the same procedure described above for the preparation of samples **2a** and **2b**.

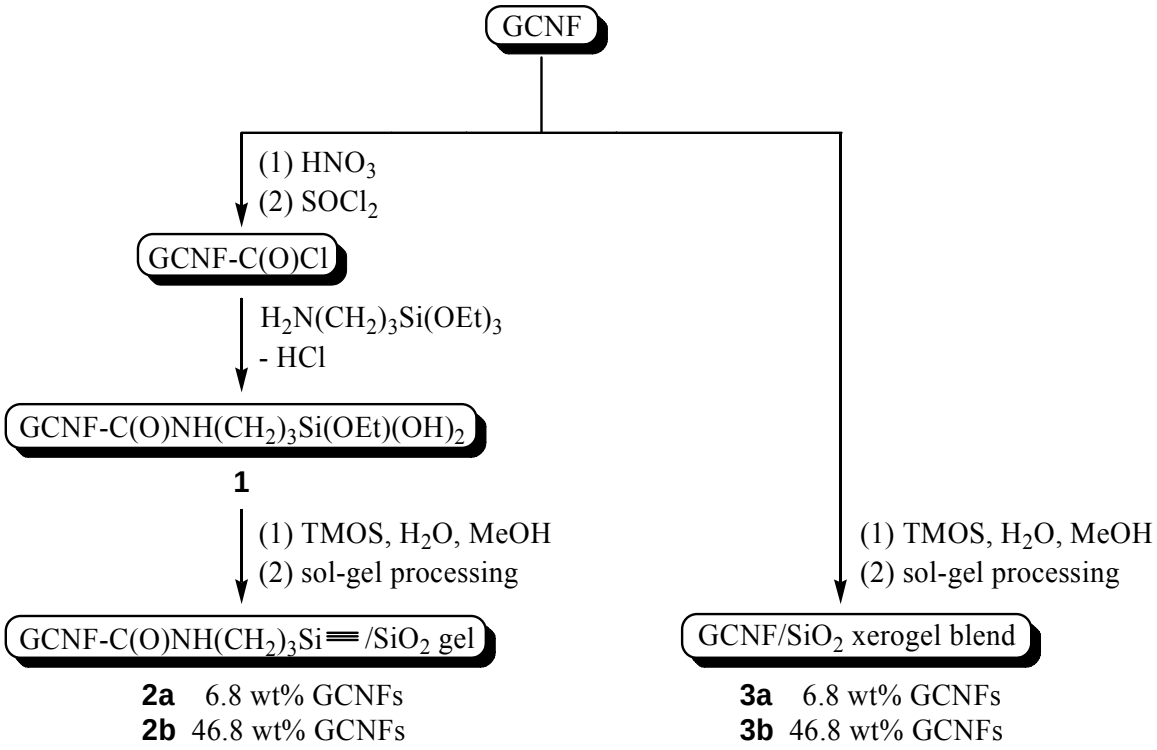

Scheme 7. Preparation of GCNF/silica xerogel samples **2a**, **2b**, **3a**, and **3b**.

4.3 Results and Discussion

GCNF/silica xerogel composites, with or without the use of linker molecules, have been prepared as shown in Scheme 7. Surface oxidation and subsequent acylation of as-prepared GCNFs gives acylated carbon nanofibers, GCNF-$[C(O)Cl]_x$. Reaction of these acylated nanofibers with neat 3-aminopropyl triethoxysilane leads to amide condensation and the formation of the GCNF-$[C(O)NH(CH_2)_3Si(OEt)(OH)_2]_x$ product, **1**. Any HCl liberated during this condensation is trapped by excess amine reagent.

The approximate chemical composition of the GCNF-$[C(O)NH(CH_2)_3Si(OEt)(OH)_2]_x$ product is derived from elemental analysis data (see Experimental). An observed Si:N atomic ratio of 1:1 is consistent with the expected

linker molecule composition, $C(O)NH(CH_2)_3Si(OEt)_3$. However, slightly reduced values for the hydrogen content indicates that some of the $Si(OEt)_3$ ethoxy groups either hydrolyze or condense during surface-derivatization. An approximate chemical composition consistent with elemental analysis data is C_{46}-$[C(O)NH(CH_2)_3Si(OEt)(OH)_2]$, which means one pendant 3-amidopropylsilyl linker molecule for approximately every 46 backbone carbon atoms.

Mild sonication of GCNF-$[C(O)NH(CH_2)_3Si(OEt)(OH)_2]_x$, **1**, with an appropriate mixture of TMOS, water, methanol, and aqueous ammonia catalyst gives a uniformly black sol which gels overnight to form a uniformly black gel product. Given the homogeneous appearance of a stable sol intermediate dispersion and of the resulting gel solid, we believe that GCNF/silica gel products of the composition GCNF-$[C(O)NH(CH_2)_3Si\equiv]_x/SiO_2$, **2a** and **2b**, are formed. The presence of 3-amidopropylsilyl functional groups on the surface of GCNFs imparts good wettability of the GCNF surface during the sol stage and promotes covalent binding of the GCNF surface to the silica gel matrix during gelation. The relatively high number density of 3-amidopropylsilyl linker molecules binding across the carbon nanofiber/ceramic interface essentially eliminates interfacial phase separation.

As a control reaction, underivatized as-prepared GCNFs were dispersed by sonication in the same silica sol solution. In contrast to the behavior of surface-derivatized GCNFs, **1**, the underivatized GCNFs did not form a stable sol. The underivatized GCNFs separated readily from the sol as a distinct phase giving a colorless

upper layer and a black, opaque bottom layer. Upon gelation, agglomeration and phase separation of underivatized GCNFs from the ceramic matrix is readily visible to the unaided eye.

The high integrity of the carbon nanofiber/ceramic interface in the GCNF-$[C(O)NH(CH_2)_3Si\equiv]_x/SiO_2$ gels **2a** and **2b** is also evident on the microscale from SEM micrographs (Figures 13 and 14). Micrographs of GCNF-$[C(O)NH(CH_2)_3Si\equiv]_x/SiO_2$ xerogel show GCNFs protruding from the silica host matrix (Figure 13a) and intimate contact of the ceramic matrix with the carbon nanofiber surface (Figure 13b), while SEM micrographs of an as-prepared GCNF/silica xerogel composite lacking linker molecules (Figure 14a, b) clearly reveal phase separation at the GCNF/silica xerogel interface and only physical contact between the carbon nanofiber additive and the ceramic matrix.

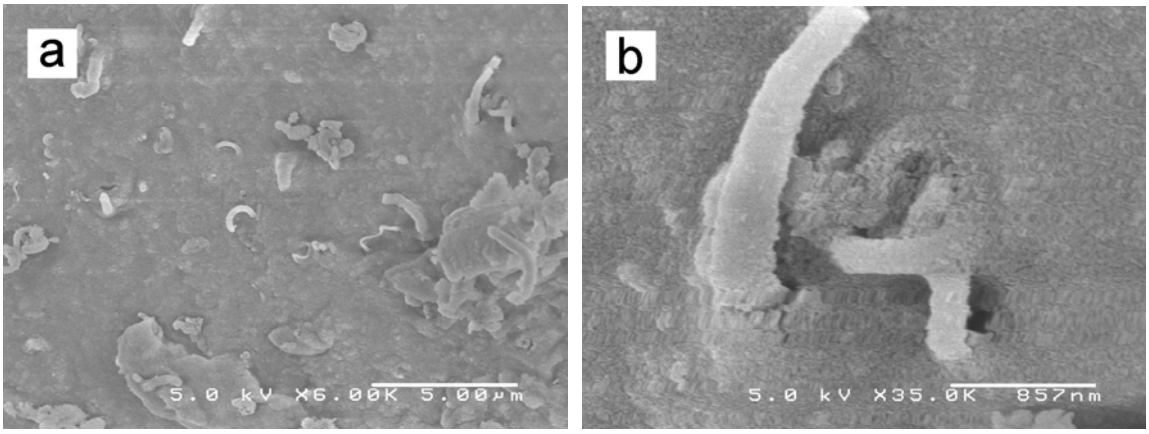

Figure 13. SEM micrographs at low (a) and high (b) magnification of a fracture surface of a type **2** GCNF/silica xerogel composite prepared using 3-amidopropylsilyl linker molecules. At high magnification, unstressed GCNFs show good wetting at the carbon/ceramic interface, while stressed GCNFs show debonding and fracture of the ceramic matrix.

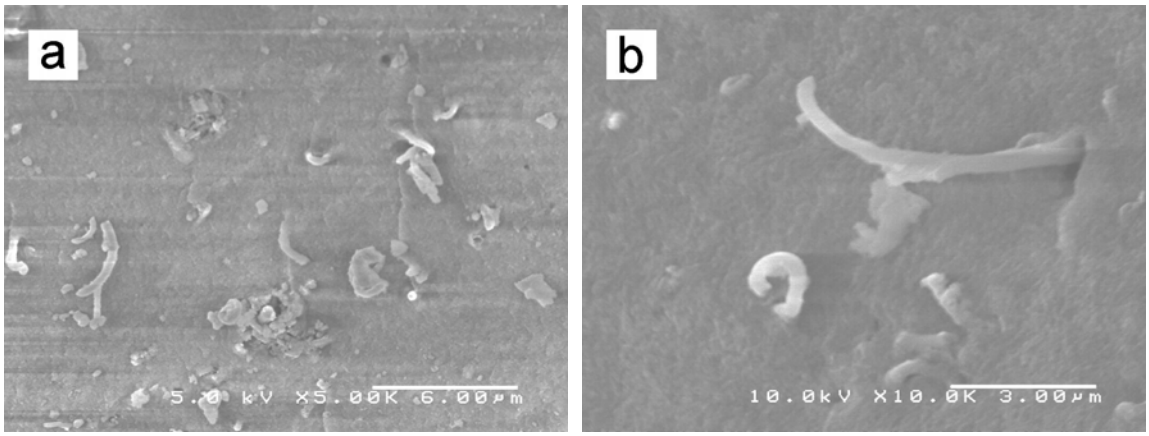

Figure 14. SEM micrographs at low (a) and high (b) magnification of a fracture surface of a type **3** GCNF/silica xerogel composite prepared without using 3-amidopropylsilyl linker molecules. At high magnification, GCNFs appear to be physically lying on top of the ceramic phase with poor wetting.

Infrared spectral data have been widely used for characterization of silica gels.[83-85] The infrared spectra of GCNF/silica xerogel composites with and without the presence of 3-amidopropylsilyl linker molecules are compared in Figure 15. Bands appearing from 800 to 1800 cm^{-1} are assigned to the expected vibrational modes shown in Table 3. The strong peak at 1655 cm^{-1} confirms the presence of amido carbonyl groups and is consistent with amido carbonyl frequencies around 1660 cm^{-1} reported for amido carbonyl groups covalently bound to the surface of single-walled carbon nanotubes[54b,55a,87] and graphite.[88]

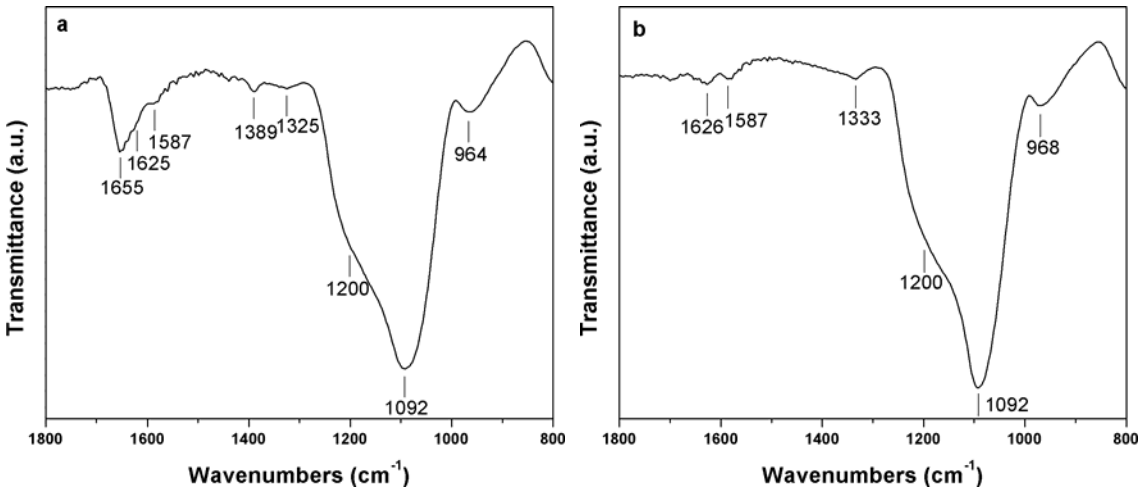

Figure 15. IR spectra of a type **2** GCNF/silica xerogel composite prepared using 3-amidopropylsilyl linker molecules (a) and of a type **3** GCNF/silica xerogel composite prepared using carbon nanofibers without surface derivatization (b).

Table 3. IR spectral data of GCNF/silica xerogels **2b** and **3b**

Product **2b**	Product **3b**	Assignment
964 cm^{-1}	968 cm^{-1}	Si-OH stretching band[83-85]
1092 cm^{-1}	1092 cm^{-1}	Si-O-Si antisymmetric stretching band[83-85]
1325 cm^{-1}	1333 cm^{-1}	C-OH stretching band[86]
1389 cm^{-1}	—	Carboxylic C-O-H bending or amide C-N stretching band[86]
1587 cm^{-1}	1587 cm^{-1}	C=C stretching band[86]
1625 cm^{-1}	1626 cm^{-1}	Deformation of residual water[83,85]
1655 cm^{-1}	—	Amide C=O stretching band[87,88]

Thermogravimetric analysis of GCNF/silica gels prepared with or without amidopropylsilyl linker molecules are shown in Figure 16. Mass loss is detected for both samples upon heating from room temperature to 900 °C due to progressive dehydration of the silica gel matrix. In addition to this water loss, a higher rate of mass loss is observed for samples containing linker molecules. The slope of the weight-loss curve for thermal degradation of a GCNF/silica gel sample containing 6.8 wt% of derivatized GCNFs (**2a**) is slightly larger than that for a GCNF/silica gel sample containing 6.8 wt% of underivatized, as-prepared GCNFs (**3a**), (Figure 16a). The higher rate of observed mass loss for samples containing linker molecules is attributed to the thermal decomposition of the organic linker molecules present within the sample. A comparison

of TGA curves for samples **2b** and **3b** that contain 46.8 wt% GCNFs as either surface-derivatized (**2b**) or underivatized (**3b**) nanofibers shows a greater relative rate of mass loss from the sample containing linker molecules, consistent with this mass-loss assignment (Figure 16b).

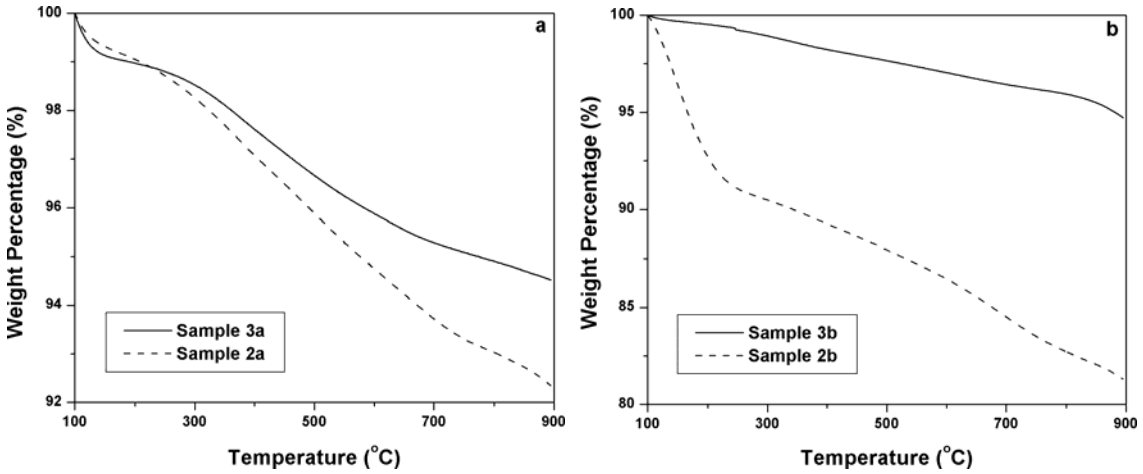

Figure 16. Comparison of TGA mass-loss curves for type **2** GCNF/silica xerogel composites prepared using 3-amidopropylsilyl linker molecules and type **3** GCNF/silica xerogel composites prepared using carbon nanofibers without surface derivatization at GCNF loadings of 6.8 wt% (**2a** and **3a**) and of 46.8 wt% (**2b** and **3b**).

4.4 Conclusions

Sol-gel reaction of tetramethoxysilane with herringbone GCNFs surface-derivatized with 3-amidopropylsilyl groups gives uniform stable sols that age to form uniformly black gel products. Control reactions using underivatized GCNFs reveal immediate separation of the carbon nanofiber and ceramic phases. Although direct evidence for covalent binding of linker molecules to the ceramic phases has yet to be obtained,

experimental observations and SEM micrographs of the resulting GCNF/silica gel products are consistent with some degree of covalent binding of linker molecules across the GCNF/ceramic interface.

CHAPTER V

PREPARATION AND ELECTRON EMISSION MEASUREMENTS OF GCNF/SILICON WAFER NANOCOMPOSITES

5.1 Introduction

Growth of carbon nanostructures, either carbon nanotubes or carbon nanofibers, on silicon wafers has attracted extensive interest for diverse applications, such as DNA delivery and gene expression,[89] AFM probe tips,[90] asymmetric functionalization,[91] hydrogen storage,[92] field emission,[93] molecular electronics,[94] nanotransistors[95] and memory storage.[96] To our knowledge, there are no studies on thermionic emission from carbon nanostructures grown on silicon wafers.

Devices based on thermionic emission are used in many contemporary applications as stable electron sources. These applications include scanning electron microscopes, fluorescent lighting, cathode ray tubes, x-ray tubes, mass spectrometers, vacuum gauges, and other scientific instruments. Further, thermionic emission is a viable means of converting heat directly into electrical power. This may be a potential pathway for addressing the developing energy demand issue given the presence of broad heat sources, such as solar radiation, nuclear reaction, and the combustion of fossil fuels. Thermionic power generation has many attractive qualities, including scalability, high reliability, high current density and power density, and silent vibration-free operation.[97,98] However, the requirement of operation at high temperature caused by the high work functions of

typical thermionic emitter materials has limited the applicability of thermionic power generation.

As measured by photoelectron emission spectroscopy at room temperature, single-walled and multi-walled carbon nanotubes exhibit work functions around 5 eV,[99] which are slightly higher than that of graphite (4.60 eV).[98] The work function of carbon nanofibers is of interest given the structural variety and nanoscale dimensions of these materials. In the present work, we have successfully grown graphitic carbon nanofibers on silicon wafers by spin-coating catalyst precursor powders onto silicon wafer surfaces and have measured the energy distributions of electrons emitted thermionically from these wafer-supported graphitic carbon nanofibers.

5.2 Experimental Section

5.2.1 General Procedures

Silicon wafers with a monolayer of native oxide on the surface were purchased from University Wafer. Surface-oxidized and nickel-coated silicon wafers were obtained from our collaborators. A monolayer of silicon oxide is present on the surface of native silicon wafer, while a silica layer of about 100 nm thick is present on a surface-oxidized silicon wafer. Nickel-coated silicon wafer was obtained by irradiating a silicon wafer with a nickel atom beam for 30 seconds.

Samples were examined by scanning electron microscopy (SEM) on a Hitachi

S-4200 Electron Microscope with accelerating voltage at 5 kV. All wafer samples were sputtered with gold using a sputter coater (Pelco Model 3) for 20 seconds to form a conductive layer for SEM observations.

Thermionic electron energy distributions (TEEDs) were measured at Purdue University with a hemispherical energy analyzer (SPECS-Phoibos 100 SCD) with an energy resolution of 0.007 eV. The energy analyzer was connected to a vacuum chamber that reaches pressures on the order of 10^{-8} Torr. When a sample was tested at different temperatures, the thermionic electron energy distributions were measured in succession without intermittent cooling. The details for TEED measurements have been published earlier.[97]

5.2.2 Preparation of Herringbone GCNF/Silicon Wafer Nanocomposites

Iron-copper catalyst precursor powders with an atomic ratio of 7:3 were prepared by the coprecipitation of the respective metal nitrate solutions with ammonium bicarbonate as described in Chapter II. The precipitate was dried in an oven at 110 °C for 18 h, ground into a fine powder and dispersed in hexamethyl disilazane (HMDS, $Me_3Si\text{-}N(H)\text{-}SiMe_3$, Aldrich) by sonication for 10 min. A silicon wafer was carefully put on the vacuum chuck of a spin coater (Chemat Technology KW-4A). A few drops of pure HMDS were dropped on the silicon wafer during spinning to form a liquid thin film. A dispersion of catalyst precursor powders in HMDS was then dropped on the silicon wafer, which continued to spin at 3500 rpm for 20 seconds. The wafer was transferred onto a

heating plate to evaporate the liquid, and the resulting powder-coated wafer was cut into small pieces with a diamond scriber.

Small pieces of powder-coated silicon wafers were put into a quartz boat in a horizontal tubular furnace. The catalyst precursor was converted into a mixed-metal alloy by calcining in air at 400 °C for 4 h and by reducing in a H_2/He flow (50 and 200 mL/min) at 500 °C for 20 h and then at 600 °C for 2 h. Ethylene was introduced with the flow rate of C_2H_4:H_2:He = 200:50:50 mL/min at 600 °C for 3, 8, 12, 15, 30 and 90 min (Table 4). The product was cooled down to room temperature under helium.

To examine the influence of GCNF structures, GCNFs with perpendicular and parallel structures were grown on the surface of silicon wafers by using carbon monoxide as the carbon source gas instead of ethylene according to literature procedures.[5] The former was prepared at 600 °C for 30 min, while the latter was formed at 700 °C for the same time.

To examine the influence of silicon wafer surface coating, surface-oxidized and nickel-coated silicon wafers were used to prepare GCNF/silicon wafer nanocomposites. The various GCNF/silicon wafer samples prepared for this study are identified in Table 4.

Table 4. GCNF/silicon wafer nanocomposite samples

Sample No.	GCNF structure	Growth time (min)
	Native-oxide-coated wafers	
1	Herringbone	3
2	Herringbone	8
3	Herringbone	12
4	Herringbone	15
5	Herringbone	30
6	Herringbone	90
7	Perpendicular	30
8	Parallel	30
	Surface-oxidized wafers	
9	Herringbone	12
	Nickel-coated wafers	
10	Herringbone	12

5.3 Results and Discussion

5.3.1 Spin Coating of Catalyst Precursor Powders on Silicon Wafers

The dispersion of the growth catalyst precursor as a fine powder in HMDS was

spin-coated onto silicon wafers with spin rates of 2000 and 3500 rpm. As shown in Figure 17, the higher spin rate (3500 rpm, Figure 17b) leads to a more uniform dispersion of precursor powders on silicon wafers than does a lower spin rate (2000 rpm, Figure 17a). However, the size of precursor powder particulates is not uniform. Some are tens or hundreds of nanometers in diameter, while other particles are about ten microns (Figure 17b). Also there is some fluctuation of precursor powder deposition, which forms concentric circles (Figure 17b). This is probably due to silicon wafer surface imperfections.

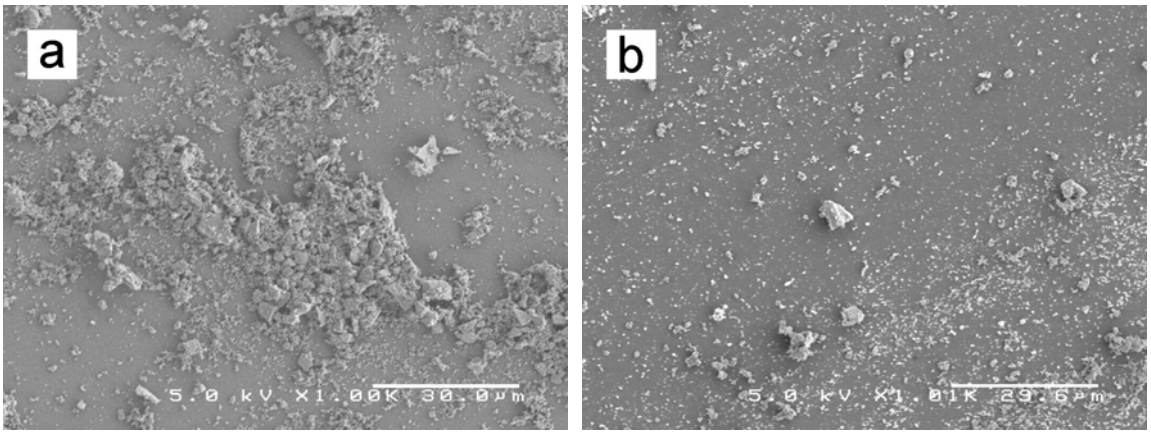

Figure 17. SEM images of catalyst precursor particles spin-coated onto native-oxide-coated silicon wafers with a spin rate of (a) 2000 or (b) 3500 rpm.

5.3.2 The Influence of GCNF Growth Time

GCNF loading on silicon wafers was varied by adjusting GCNF growth time. Herringbone GCNFs were grown using ethylene as the carbon source gas for different

time intervals of 3, 8, 12, 15, 30, and 90 min.

Different growth times yield GCNFs of different length, and thus GCNF mats of different thickness. SEM images of GCNFs grown for 3 min (Figure 18, **1**a and **1**b) or 8 min (Figure 18, **2**a and **2**b) show both small individual nanofibers and large nanofiber clusters around catalyst particles. Those individual nanofibers have diameters about 100-200 nm, and catalyst particles (bright spots in SEM images) at the ends of nanofibers have similar diameters, which confirms that the diameter of catalyst particles determines the diameter of the resulting GCNFs. GCNF lengths of 500-1000 nm are observed for growth times of either 3 or 8 min.

When the growth time is extended to 12 min, significantly longer nanofibers are obtained (Figure 18, **3**a and **3**b). GCNFs are interwoven into a GCNF mat. The thickness of the mat is not very large, since the wafer still can be seen as a black background at high magnification (Figure 18, **3**b).

When the growth time is extended to 15 min (Figure 18, **4**a and **4**b) and 30 min (Figure 18, **5**a and **5**b), longer GCNFs are obtained as a highly interwoven GCNF mat, and the silicon wafer is not visible even at high magnification. Unfortunately, these resulting GCNF mats are not mechanically robust and easily separate from the silicon wafer support due to the weak connection between the GCNFs and silicon wafers.

GCNFs grown for 90 min (Figure 18, **6**a and **6**b) are automatically stripped off after reaction. Such long nanofibers presumably have sufficient mass that their weight can not be supported at the GCNF/silicon wafer interface.

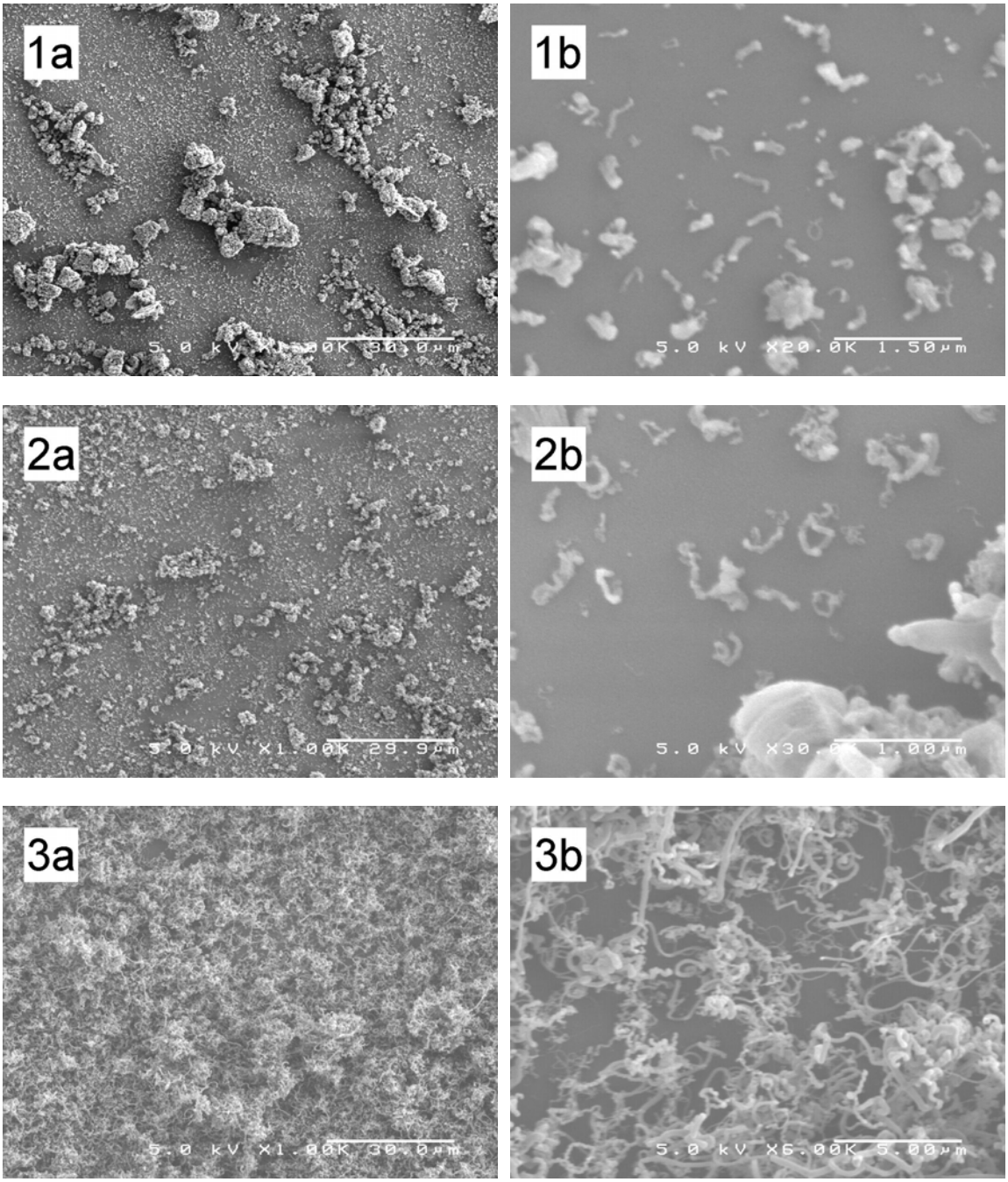

Figure 18. SEM images of herringbone GCNFs grown on native-oxide-coated silicon wafers for samples **1**-**6** at low (a) and high (b) magnification.

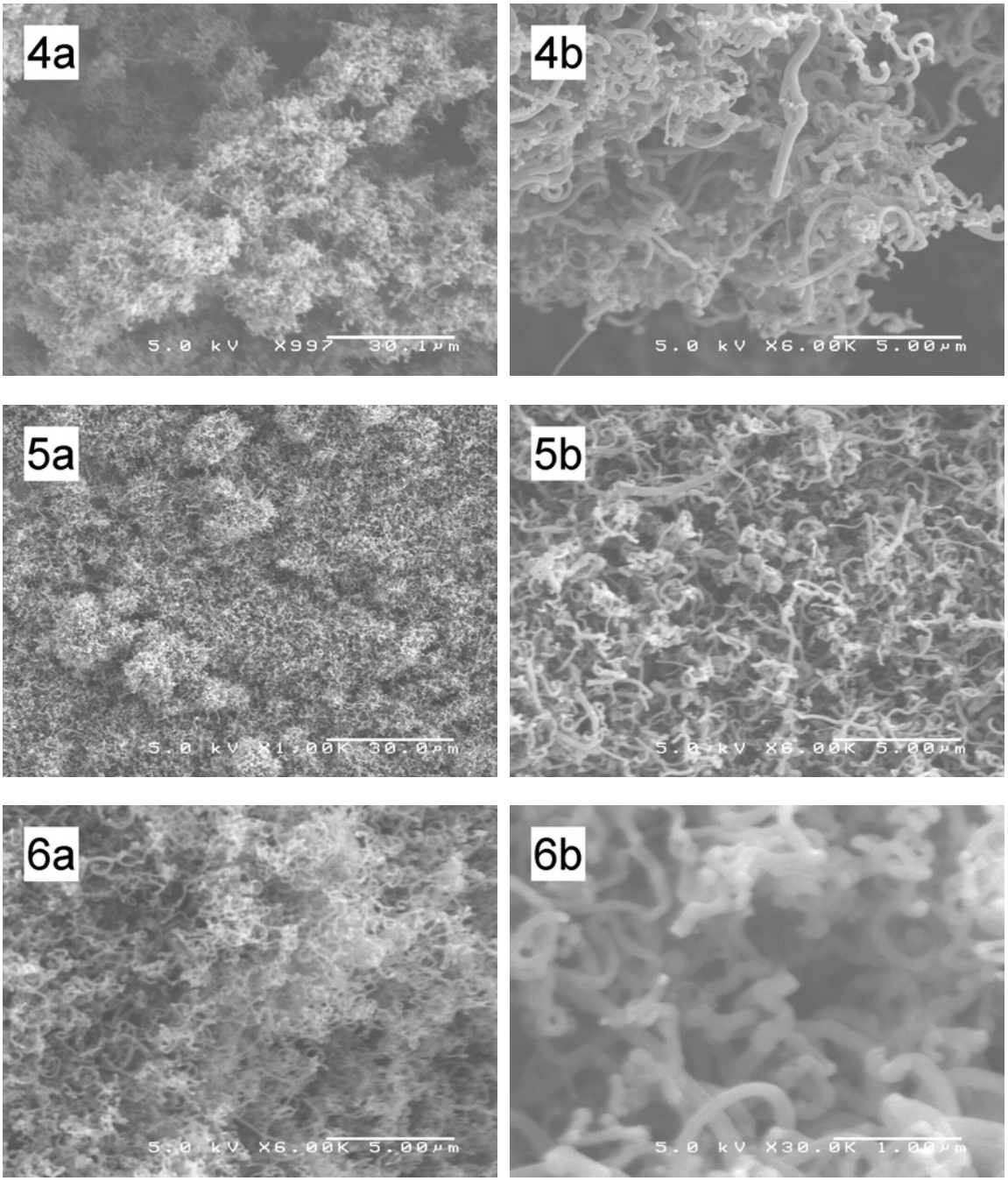

Figure 18 (Cont'd). SEM images of herringbone GCNFs grown on native-oxide-coated silicon wafers for samples **1**-**6** at low (a) and high (b) magnification.

SEM images confirm that GCNFs grow longer with increasing growth time. More precisely, GCNFs are shorter than one micron up to 8 min and grow individually. For a

growth time of 12 min, the length of the GCNFs becomes longer, so that GCNFs are interwoven with each other, and a GCNF mat forms. With longer growth time, the length of GCNFs is much longer, and a thicker GCNF mat forms and separates from the substrate. This phenomenon may be explained based on a known GCNF growth model.[5] Before 8 min, ethylene dissociates on the surface of catalyst particles and nucleation occurs as an incubation stage. After incubation, GCNF growth continues, so that the GCNFs become longer with increasing growth time and finally strip off from the substrate.

5.3.3 Different GCNF Structures and Silicon Wafer Surface Coatings

It is known that the structure of GCNFs can be controlled with the selection of carbon source gas and growth temperature.[5] All GCNFs shown in the previous section are of herringbone structure. In addition, with an Fe_7Cu_3 catalyst, perpendicular-type GCNFs can be grown by CO decomposition at 600 ^{o}C (the inset in Figure 19a), and parallel-type GCNFs grown by CO decomposition at 700 ^{o}C (the inset in Figure 19b). Following this procedure, GCNFs with perpendicular and parallel structures supported on silicon wafers (samples **7**, **8**) have been successfully prepared, as shown in Figure 19a and 19b, respectively, even though the graphene sheet orientation could not be distinguished from SEM images.

In addition to herringbone GCNFs grown on native-oxide-coated silicon wafers as shown in Figure 18 (a-l), herringbone-type GCNFs have also been grown on

surface-oxidized and nickel-coated silicon wafers (samples **9**, **10**) as shown in Figure 19c and 19d.

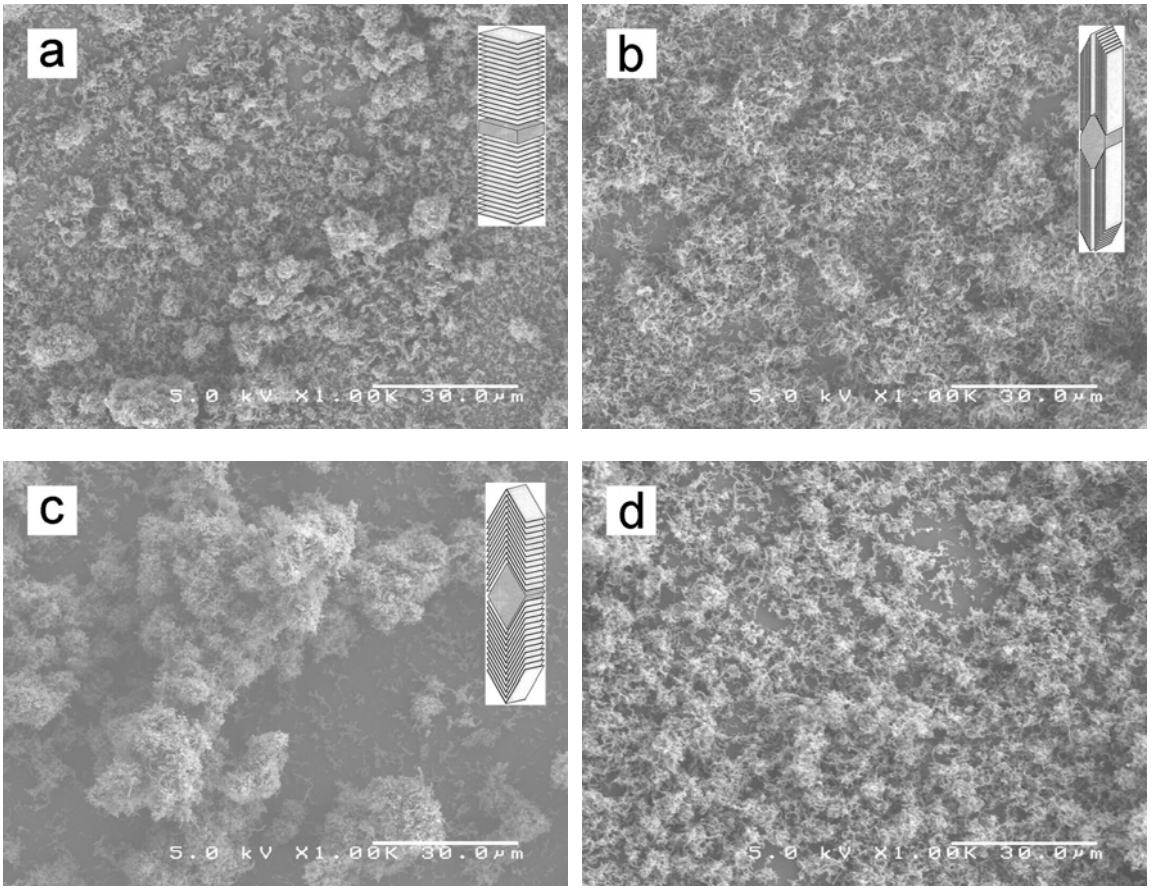

Figure 19. (a) Perpendicular- and (b) parallel-type GCNFs grown on native-oxide silicon wafers, and herringbone-type GCNFs on (c) oxidized and (d) nickel-coated wafers. The insets are schematic illustration of perpendicular, parallel and herringbone structures, respectively (Reprinted from ref 4. Copyright 2001 American Chemical Society.)

5.3.4 Thermionic-Emission Testing Data

Figure 20 shows the total energy distribution curves of select GCNF/silicon wafer nanocomposite samples from thermionic-emission testing at different temperatures. The

curve in Figure 20a is from herringbone-type GCNFs on the surface of a native-oxide-coated silicon wafer, which were grown from ethylene decomposition on an Fe_7Cu_3 catalyst for 8 min (sample **2**). The leading edge of thermionic electron energy distributions indicates the magnitude of potential energy barrier keeping electrons in the material, 4.24 eV in this case, which is similar to the work function of graphitic carbon. The diminishing intensity on the trailing edge is attributable to the decrease in available energy states defined by Fermi-Dirac statistics. One thing to be noted is that the multiple peaks along the trailing edge are reapeatable and equally spaced (0.014 eV). There may be two possible reasons for these patterns. One is quantum size effects, in which electron emission peaks are observed at energies corresponding to the work functions of GCNFs having different diameters. The other explanation is that the observed peaks may come from electron emission from carbon atom occupying different surface sites having different local energy.

Also, TEED curves have been acquired for herringbone GCNFs grown on native-oxide-coated silicon wafers for 30 min (sample **5**) and parallel GCNFs grown on native-oxide-coated silicon wafers for 30 min (sample **8**), as shown in Figure 20b and 20c. Work function values have been calculated from the TEED curves and are summarized in Table 5. It is shown that shorter growth time leads to a lower work function at the same testing temperature. Another phenomenon is that nanofibers with a herringbone structure have slightly lower work functions than those with a parallel structure, which may be assigned to the large number of unsaturated edge-site carbon atoms along the surface of

herringbone-structure nanofibers (inset of Figure 19c).

Full-width at half-maximum (FWHM) values have been calculated from TEED curves and compared with expected values from free-electron theory. The theory predicts a FWHM value of 2.45 kT for thermionic electron emission,[100] in which k is the Boltzmann constant, 1.31 x 10^{-23} J K^{-1} or 8.63 x 10^{-5} eV K^{-1}, and T is sample temperature. The FWHM values are consistent with predicted values within experimental error, suggesting that thermionic electron emission from nanofibers complies with free-electron theory.

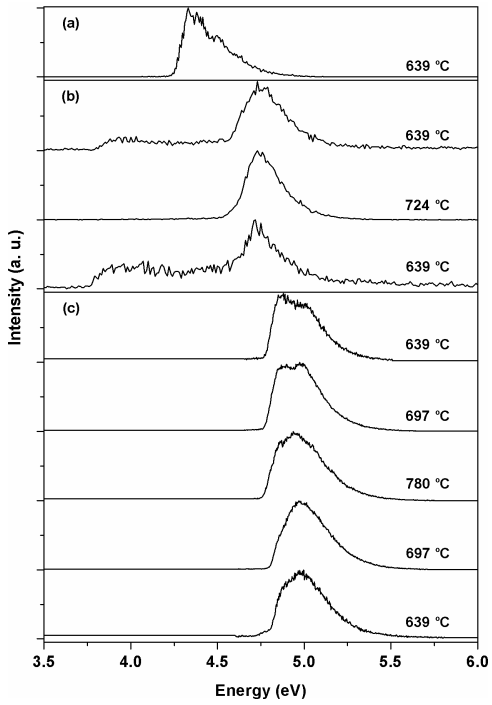

Figure 20. Thermionic electron energy distribution curves of GCNF/native-oxide-coated silicon wafer samples: (a) sample **2**, herringbone GCNFs with growth time of 8 min, (b) sample **5**, herringbone GCNFs with growth time of 30 min, and (c) sample **8**, parallel GCNFs with growth time of 30 min.

Table 5. TEED measurements of GCNFs on native-oxide-coated silicon wafers

Sample No.	Sample	T (^{o}C)	E_{max}[a] (eV)	φ[b] (eV)	FWHM[c] (eV)	2.45 kT (eV)
2	Herringbone GCNFs grown for 8 min	639	4.33	4.24	0.24	0.19
5	Herringbone GCNFs grown for 30 min	639	4.74	4.54	0.27	0.19
		724	4.73	4.58	0.23	0.21
		639	4.72	4.57	0.24	0.19
8	Parallel GCNFs grown for 30 min	639	4.86	4.78	0.30	0.19
		697	4.86	4.77	0.30	0.21
		780	4.95	4.75	0.31	0.22
		697	4.97	4.78	0.30	0.21
		639	4.99	4.80	0.31	0.19

[a] E_{max}: Peak energy. [b] φ: work function. [c] FWHM: full width at half maximum.

5.4 Conclusions

GCNF mats on silicon wafers were prepared by spin-coating catalyst precursor powders onto silicon wafers followed by GCNF growth from thermal decomposition of carbon source gas. The morphology of GCNF mats was examined by SEM, showing that GCNFs became longer with increased growth time, but with reduced mechanical robustness of GCNF/silicon wafer nanocomposites. Thermionic-emission testing data

show that GCNF/silicon wafer nanocomposites have work functions of 4.24-4.80 eV, similar to graphite. Given the poor robustness of GCNF/silicon wafer nanocomposites, other substrates have been examined for GCNF mat formation, as discussed later.

CHAPTER VI

SUPERHYDROPHOBIC GCNF/CARBON FELT NANOCOMPOSITES BIOMIMICKING LOTUS LEAVES

6.1 Introduction

Superhydrophobic materials have attracted much interest during the last few years for applications from resisting water coalescence, fog condensation, and contamination prevention to increasing biocompatibility, lubricity and durability.[101] These superhydrophobic materials, having water contact angles larger than 150^{o}, are mainly made of or have a cover layer of polymer with intrinsic hydrophobicity.[102]

A closely related phenomenon in nature, the lotus-leaf effect, refers to lotus-leaf-like surfaces showing nominal superhydrophobicity with "self-cleaning" capability.[103] In detail, SEM images of lotus leaves display randomly distributed papillae with diameters ranging from 5 to 9 μm (Figure 21a),[103] which further consist of branch-like nanostructures with diameters of 100-150 nm (Figure 21b).[104] The superhydrophobic property is mainly based on the hierarchical micro- and nano-scale structures, and in a minor part based on the hydrophobic epicuticular wax chemistry. The importance of hierarchical structure has been emphasized by experimental results, in that the superhydrophobicity of a lotus leaf can vanish when water is condensed onto its surface from vapor phase, yielding a "hydrophilic" lotus leaf.[104-106] This significant finding suggests that superhydrophobic materials can be synthesized by designing a hierarchical

structure from non-waxy compositions.

In this study, two types of GCNFs have been grown on weakly hydrophobic carbon felt to mimic the binary micro- and nano-scale structure of a lotus leaf. One is wide herringbone GCNFs (w-GCNFs), as discussed in the previous chapters, which have diameters of 150-200 nm based on the sizes of Fe_7Cu_3 growth catalyst particles. The other one is narrow herringbone GCNFs with diameters of 20-50 nm (n-GCNFs), which are grown from Fe_2Ni_8 nanoparticles supported on fumed silica.[6,10] Both types of GCNFs have been grown on a carbon felt substrate yielding w-GCNF/carbon felt and n-GCNF/SiO_2/carbon felt samples. Carbothermal treatment of the n-GCNF/SiO_2/carbon felt sample at 1650 ^oC transforms the silicon oxide phase into silicon carbide, which tightly binds the GCNFs onto carbon felt support, showing superior mechanical robustness and chemical stability.

Water contact-angle measurements reveal that only n-GCNF/SiC/carbon felt samples show superhydrophobicity, while density measurements indicate a bulk density of 0.11 g/cm^3 for n-GCNF/SiC/carbon felt, only one fifth of that for carbon felt (0.64 g/cm^3). Furthermore, the superhydrophobic sample can be reversibly changed to a hydrophilic surface with simple hot water treatment and then back to superhydrophobicity with vacuum drying, a close mimicking of both structure and property of lotus leaves.

6.2 Experimental Section

6.2.1 General Procedures

Carbon felt was purchased from Alfa Aesar as a felt pad of 100 × 100 mm and 3.18 mm thick. The pad was cut into small pieces of 10 × 10 mm for use in this study. Scanning electron microscopic (SEM) images, energy dispersive X-ray spectra (EDX) and elemental mapping images were obtained on a Hitachi S-4200 Electron Microscope with accelerating voltage at 5 or 20 kV. X-ray diffraction (XRD) scans were obtained using a Scintag X_1 θ/θ automated powder X-ray diffractometer with a Cu target, a Peltier-cooled solid-state detector, and a zero-background Si (510) support. Static contact angles were determined at room temperature by the sessile drop method with a Rame-Hart goniometer (Model 100-00) using a Gilmont syringe with deionized water. Bulk density was determined by dipping pre-weighed samples into deionized water in a thin graduated cylinder and calculated from the mass and the volume difference before and after sample dipping. TEED measurements were conducted as described in Section 5.2.1.

6.2.2 Preparation and Acid Etching of GCNF/Carbon Felt Nanocomposites

n-GCNF/SiO_2/Carbon Felt Ten milligram of Fe_2Ni_8/silica catalyst precursor[6,107] was dispersed in 1 mL of ethanol with sonication for 5 min. The dispersion was dropped on small pieces of carbon felt and then dried in 110 ^oC for 18 h. After transferring into a tube

furnace, the catalyst precursor was calcined in the air at 400 ^{o}C for 4 h, reduced in H_2/He flow (50:200 mL/min) at 350 ^{o}C for 24 h and then at 600 ^{o}C for 2 h. n-GCNFs were grown on the surface of carbon felt fibers by introducing carbon monoxide at a flow rate of CO:H_2:He = 200:50:50 mL/min at 600 ^{o}C for 10 h. The resulting n-GCNF/SiO_2/carbon felt sample was cooled to room temperature under helium.

n-GCNF/SiC/Carbon Felt A n-GCNF/SiO_2/carbon felt sample was placed into a graphite furnace (Oxy-Gon Industries). The furnace was pumped down to reduced pressure of 2.0×10^{-5} Torr, and heated at 300 ^{o}C for 10 min. Then the furnace was filled with high purity of Ar (99.9999%) and then heated to 1650 °C for 30 min to yield n-GCNF/SiC/carbon felt sample. This heating process was conducted by Dr. Weijie Lu.

w-GCNF/carbon felt Fe_7Cu_3 catalyst precursor powder, as prepared in Section 2.2.2, was deposited onto small pieces of as-received carbon felt as described above and wide herringbone-type GCNFs were grown on the carbon felt support, using ethylene as carbonaceous gas at 600 ^{o}C as Section 2.2.2, and giving w-GCNF/carbon felt samples.

Acid etching For HCl etching, a GCNF/ carbon felt sample (n-GCNF/SiO_2/carbon felt or n-GCNF/SiC/carbon felt) was soaked in HCl solution (28.7 mL of concentrated hydrochloric acid and 6.3 mL of ethanol) for 24 h and washed with ethanol/water (volume ratio of 1:1) until washings had a neutral pH. Then the sample was washed with ethanol and dried in vacuo at room temperature.

For HF etching, a GCNF/carbon felt sample was soaked in HF solution (12.7 mL of concentrated hydrofluoric acid and 22.3 mL of ethanol) for 24 h and washed with

ethanol/water (volume ratio of 1:1) until washings had a neutral pH. Then the sample was washed with ethanol and dried in vacuo at room temperature.

Hot water treatment n-GCNF/SiC/carbon felt was dipped into boiling water for 10 min. The sample was taken out, and the water contact angle was measured immediately.

6.3 Results and Discussion

6.3.1 Morphology Analysis

As-received carbon felt consists of curly fibers interwoven together (Figure 21c and 21d), and the carbon felt fibers have an average diameter of ca. 15 μm.

Narrow herringbone GCNFs are grown on carbon felt fibers following deposition of Fe_2Ni_8/silica growth catalyst precursor, and in situ catalyst reduction and GCNF fiber growth using carbon monoxide. As shown in Figure 21e and 21f, the interwoven structure of carbon felt is retained, while the carbon felt fibers are entirely covered by a coating of n-GCNFs having a nanofiber average diameter of ca. 50 nm. The diameter of carbon felt fiber has undergone little change indicating an n-GCNF layer thickness of less than one micron, since n-GCNFs are wrapping around the carbon felt fibers, not protruding away from the surface, probably due to van der Waals interactions.

After carbothermal treatment, n-GCNF/SiO_2/carbon felt samples are transformed into n-GCNF/SiC/carbon felt samples. SEM images (Figure 21g and 21h) display that some n-GCNFs are protruding from the carbon felt surface.

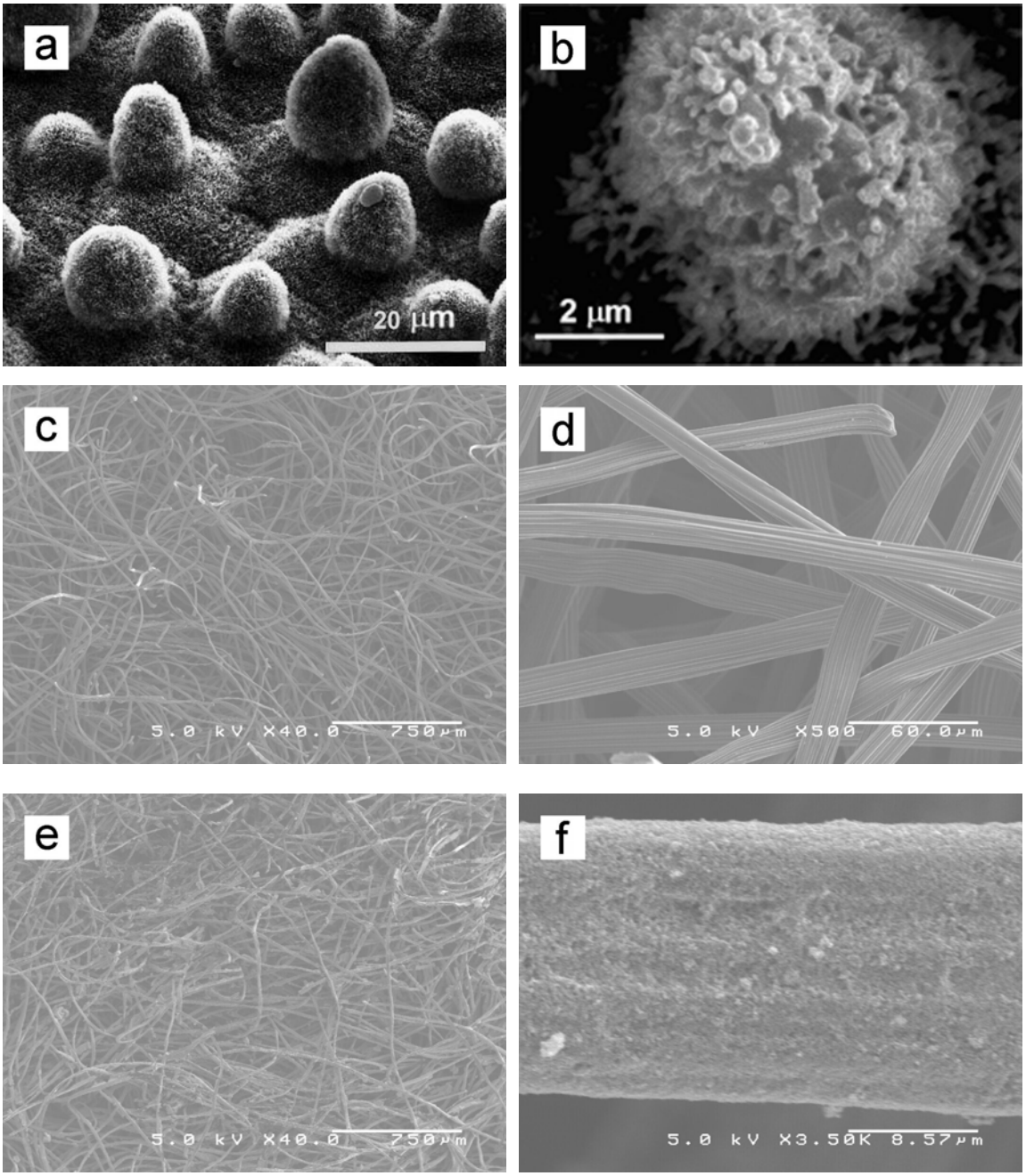

Figure 21. SEM images of (a, b) natural lotus leaf, (c, d) carbon felt, (e, f) n-GCNF/SiO_2/carbon felt, (g, h) n-GCNF/SiC/carbon felt, and (i, j) w-GCNF/carbon felt. (a and b are reproduced from ref 103 and 104. Copyright 1997 Springer-Verlag and 2002 Wiley-VCH.)

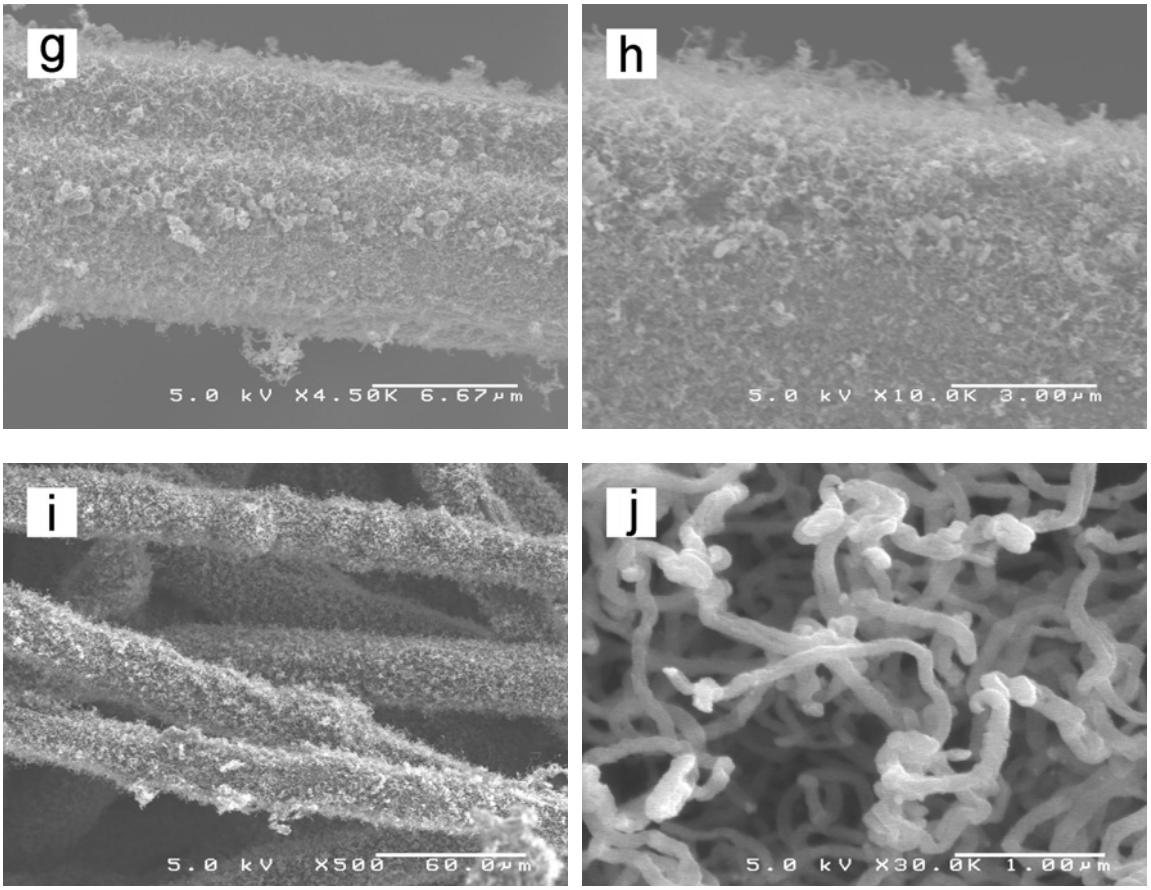

Figure 21 (Cont'd). SEM images of (a, b) natural lotus leaf, (c, d) carbon felt, (e, f) n-GCNF/SiO_2/carbon felt, (g, h) n-GCNF/SiC/carbon felt, and (i, j) w-GCNF/carbon felt. (a and b are reproduced from ref 103 and 104. Copyright 1997 Springer-Verlag and 2002 Wiley-VCH.)

Wide herringbone GCNFs are grown similarly on carbon felt fibers after deposition of Fe_7Cu_3 catalyst precursor, as shown in Figure 21i and 21j. The wide GCNFs have diameters of ca. 200 nm and are loosely wrapping around the carbon felt fibers, forming a GCNF layer with thickness of ca. 5-10 μm. All of the three GCNF/carbon felt samples have a hierarchical structure, similar with the lotus leaf structure (Figure 21a and 21b).[103,104]

Acid etching is used to examine the mechanical robustness and chemical stability of the prepared GCNF/carbon felt samples. As shown in SEM images, most GCNFs are lost when n-GCNF/SiO_2/carbon felt samples were etched by acid. For HCl etching, about one third of GCNFs remain on the surface of carbon felt fibers (Figure 22a). For HF etching, only 5% of GCNFs survive (Figure 22b). The weak interactions between GCNFs and carbon felt substrate is not satisfactory for desired practical use.

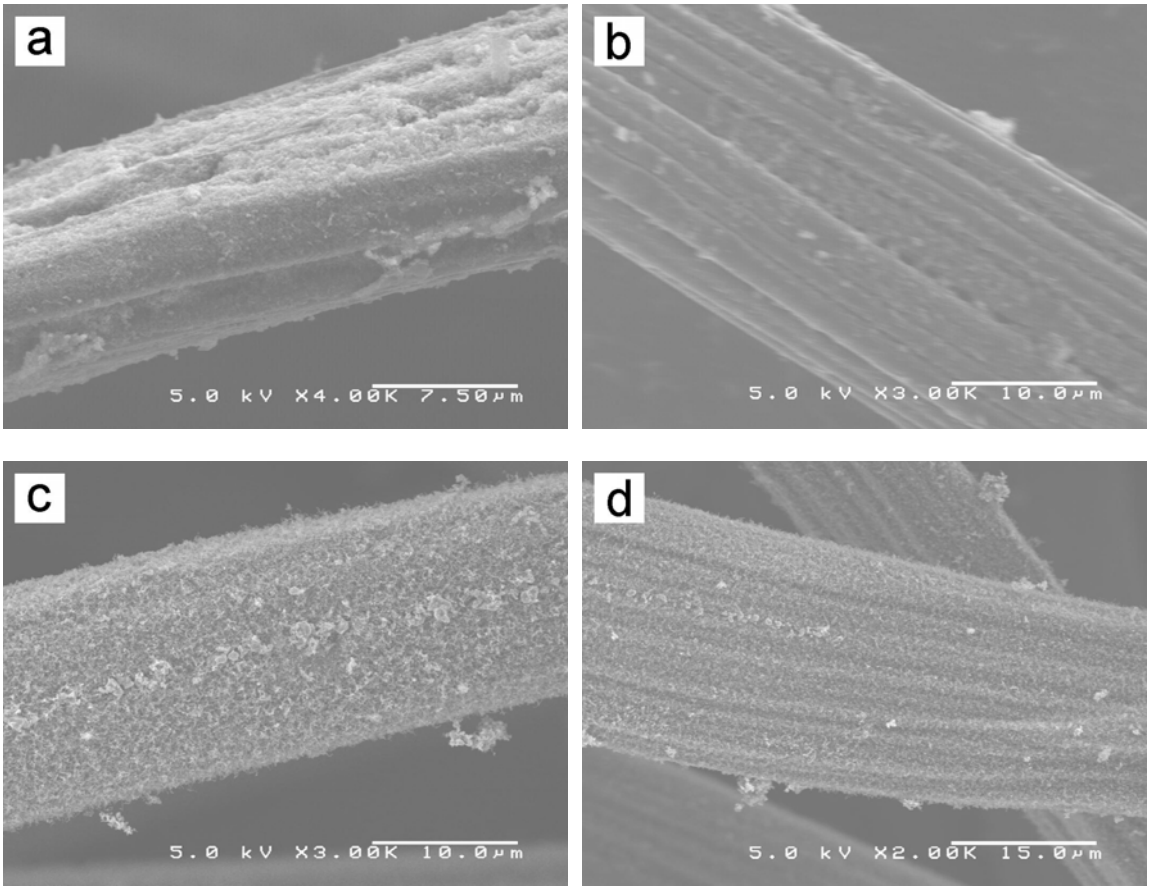

Figure 22. SEM images of n-GCNF/SiO_2/carbon felt nanocomposites after (a) HCl etching and (b) HF etching and of n-GCNF/SiC/carbon felt nanocomposites after (c) HCl etching and (d) HF etching.

After carbothermal treatment, n-GCNF/SiO_2/carbon felt samples are transformed into n-GCNF/SiC/carbon felt samples. SEM images of n-GCNF/SiC/carbon felt samples after HCl etching (Figure 22c) and HF etching (Figure 22d) confirm that GCNFs are retained, indicating the superior mechanical robustness and chemical stability imparted by the SiC phase.

6.3.2 Composition Analysis

Qualitative elemental analysis has been performed by energy-dispersive X-ray spectroscopy (EDX). Four elements, carbon, silicon, oxygen, and nickel, are present in the n-GCNF/SiO_2/carbon felt sample (Figure 23a), while residual iron remaining from the growth catalyst cannot be detected due to its low content. After HCl etching, the emission peak of nickel disappears (Figure 23b), showing that nickel (iron as well) is dissolved by HCl. After HF etching, the peaks corresponding to nickel, silicon, and oxygen disappear (Figure 23c), indicating that both iron/nickel catalyst and silica support are dissolved by HF.

After carbothermal treatment, oxygen disappears, while silicon is still present (Figure 23d), suggesting the conversion of silicon oxide into silicon carbide. This silicon carbide phase even survives HCl etching and HF etching, as shown from the corresponding EDX spectra (Figure 23e and 23f).

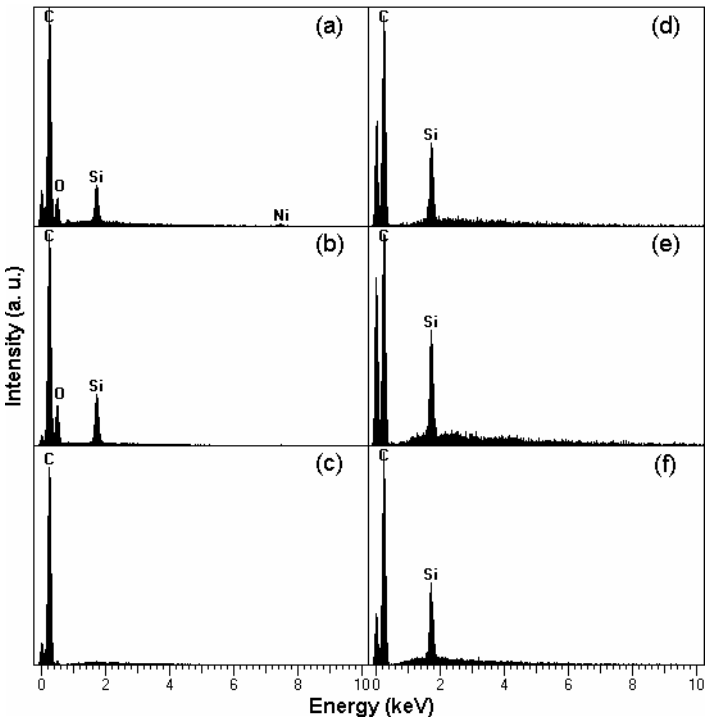

Figure 23. EDX spectra of n-GCNF/SiO_2/carbon felt nanocomposites before (a) and after (b) HCl etching and after (c) HF etching and of n-GCNF/SiC/carbon felt nanocomposites before (d) and after (e) HCl etching and after (f) HF etching.

Elemental mapping images reveal changes of elemental distributions before and after carbothermal treatment. For this purpose, n-GCNF/SiO_2/carbon felt and n-GCNF/SiC/carbon felt samples with sub-monolayer coverage of GCNFs on carbon felt fibers were prepared and imaged. SEM images (Figure 24a and 24e) confirm the desired low surface density of n-GCNFs on carbon felt fibers. Before carbothermal treatment, silicon (Figure 24c) and oxygen (Figure 24d) are distributed along the carbon felt fibers as is carbon (Figure 24b), although with much lower intensity due to their low contents. Iron and nickel mapping shows totally random light spots from instrumental noise given

their very low contents (images not shown).

After carbothermal treatment, silicon mapping (Figure 24g) still shows light spots along carbon felt fibers, suggesting the discrete distribution of silicon carbide, while oxygen mapping shows random instrumental noise (Figure 24h), confirming the disappearance of oxygen element. It is also suggested that during carbothermal treatment, silicon oxide particles are transformed into silicon carbide particles without layer formation. It is the silicon carbide particles that effectively connect GCNFs onto carbon felt fibers.

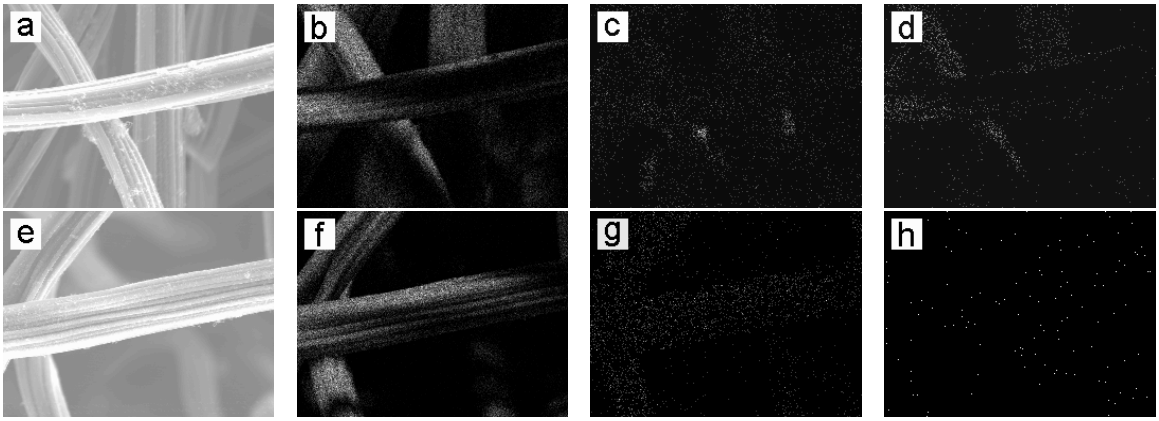

Figure 24. Elemental mapping of (a-d) n-GCNF/SiO_2/carbon felt and (e-h) n-GCNF/SiC/carbon felt samples. Panels from left to right: SEM images (a, e), carbon mapping (b, f), silicon mapping (c, g), and oxygen mapping (d, h).

The presence of crystalline phases was examined by XRD (Figure 25). As-received carbon felt is multi-crystalline as suggested by XRD (scan a in Figure 25), which can be indexed as graphite (ICDD PDF # 41-1487). n-GCNF/SiO_2/carbon felt only shows

graphite diffractions (scan b), the same as as-received carbon felt sample (scan a). Diffractions from silica or Fe_2Ni_8 catalyst cannot be seen given their low content and/or amorphous nature.

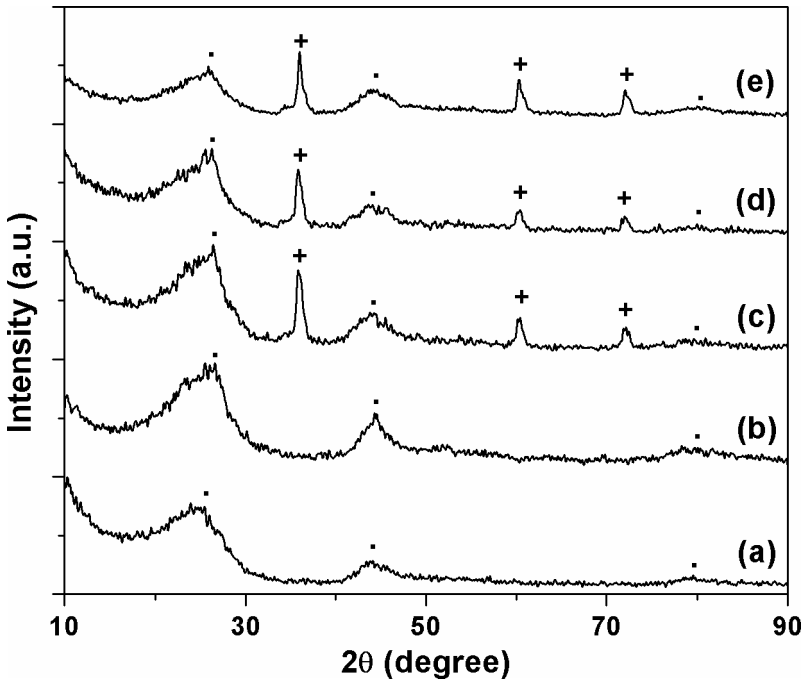

Figure 25. XRD scans of (a) carbon felt and of (b-e) GCNF/carbon felt samples, including (b) n-GCNF/SiO_2/carbon felt, (c) n-GCNF/SiC/carbon felt, and (d) HCl-etched or (e) HF-etched n-GCNF/SiC/carbon felt samples. Peaks with (·) come from graphite phase while those indicated by (+) from silicon carbide phase.

After carbothermal treatment, a highly crystalline phase appears (scan c), which can be assigned to cubic 3C-SiC (ICDD PDF # 29-1129). This is consistent with the argument that the silica phase has been converted into silicon carbide, and with previous studies in the Lukehart group that GCNF/silica aerogel composites can be transformed to SiC/silica

nanocomposites via carbothermal treatment under the same conditions.[108] XRD scans of n-GCNF/SiC/carbon felt composites after HCl etching and HF etching (scans d and e) confirm that the silicon carbide phase survives harsh acid etching treatment.

6.3.3 TEED Measurements of GCNF/Carbon Felt Samples

Thermionic electron energy distribution (TEED) curves of GCNF/carbon felt samples have been obtained between 750-1000 ^{o}C. Some typical curves are shown in Figure 26. From the TEED curves, work functions of these samples have been determined as shown in Table 6. The work function of as-received carbon felt is 4.52 eV, similar to that of graphite (4.60 eV). All the work functions of GCNF/carbon felt samples measured at temperature of 850-1000 ^{o}C fall in the range of 4.42-4.64 eV, similar to that of the carbon felt control sample. Two work functions measured at 750 ^{o}C, 4.33 eV for n-GCNF/SiC/carbon felt and 4.24 eV for w-GCNF/carbon felt, are lower than those measured at higher temperature.

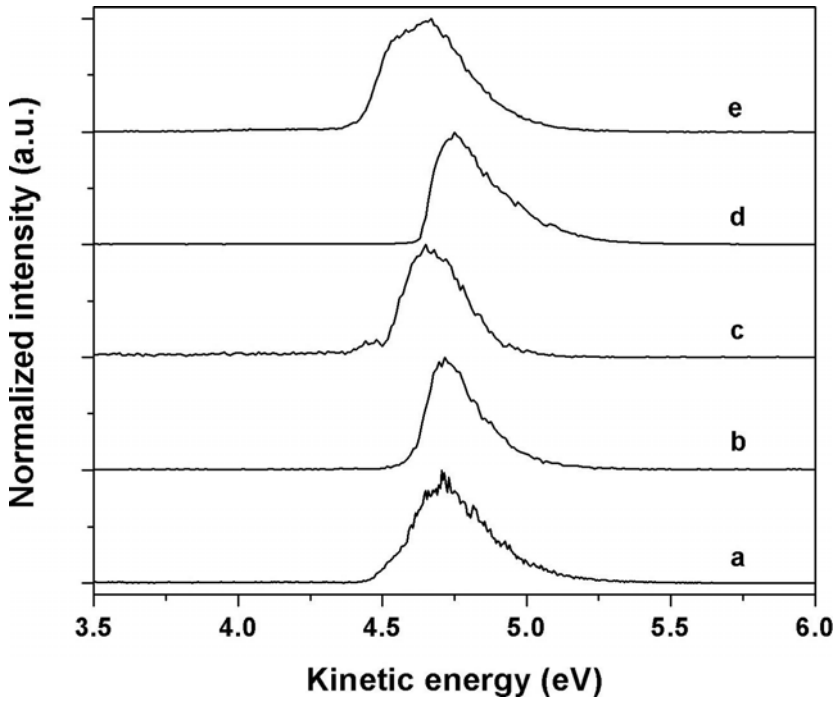

Figure 26. TEED curves of (a) carbon felt at 950 ^{o}C and of (b-e) GCNF/carbon felt samples, including (b) n-GCNF/SiO_2/carbon felt at 850 ^{o}C, (c) HCl-etched n-GCNF/SiO_2/carbon felt at 950 ^{o}C, (d) n-GCNF/SiC/carbon felt at 900 ^{o}C, and (e) w-GCNF/carbon felt at 900 ^{o}C.

The FWHM values have been estimated from TEED curves as shown in Table 6. As discussed in Chapter V, the free-electron theory predicts a FWHM value of 2.45 kT for thermionic electron emission. The FWHM values are consistent with predicted values within experimental error, suggesting that thermionic electron emission from nanofibers complies with free-electron theory.

Table 6. TEED measurements of GCNF/carbon felt nanocomposites

Sample	Temperature (^oC)	E_{max}[a] (eV)	φ[b] (eV)	FWHM[c] (eV)	2.45 kT (eV)
Carbon felt	950	4.70	4.52	0.26	0.20
	1000	4.72	4.49	0.24	0.21
n-GCNF/SiO_2/carbon felt	850	4.72	4.60	0.20	0.18
n-GCNF/SiO_2/carbon felt, HCl etched	950	4.67	4.50	0.25	0.20
n-GCNF/SiC/carbon felt	750	4.44	4.33	0.22	0.16
	850	4.76	4.64	0.21	0.18
	900	4.75	4.63	0.24	0.19
	950	4.72	4.61	0.26	0.20
w-GCNF/carbon felt	750	4.50	4.24	0.29	0.16
	900	4.67	4.42	0.32	0.19

[a] E_{max}: Peak energy. [b] φ: work function. [c] FWHM: full width at half maximum.

6.3.4 Contact-Angle Measurements of GCNF/Carbon Felt Samples

The hydrophilicity and hydrophobicity of nanomaterials have been studied recently.[101,102] In particular, the superhydrophobicity of lotus leaves has attracted a lot of research interest, and the lotus-leaf effect has been ascribed to the binary micro- and nanoscale structural features on the top surface of lotus leaves.[103-106] Several biomimics

of the lotus leaf have been reported, mostly utilizing polymer systems.[102]

GCNF/carbon felt samples prepared in this study are close structural mimics to lotus leaves, as shown in SEM images (Figure 21). Contact-angle measurements have been performed on these GCNF/carbon felt samples. In a sessile drop method, a water droplet stays on the surface of a sample, and the contact angle at the interface can be measured. However, as-received carbon felt cannot stabilize a water droplet, since the water droplet quickly permeates into the carbon felt. As-received carbon felt transiently holds a water droplet with a contact angle at $90^{o} \pm 10^{o}$, as shown in Figure 27a. However, a n-GCNF/SiC/carbon felt sample stabilizes a water droplet very well, with a contact angle of $150^{o} \pm 3^{o}$, as shown in Figure 27b. There is only a slight change of contact angle for HF-etched samples, as shown in Figure 27c. n-GCNF/SiC/carbon felt samples stabilize a water droplet, because those nanofibers contain nano-scale porosity, and the surface tension of water at those air pockets supports the water droplet.

Even with similar structural features, both n-GCNF/SiO_2/carbon felt and w-GCNF/carbon felt samples cannot stabilize a water droplet, and water immediately permeates into these samples. This observation may be ascribed to the poor robustness of these samples. Water droplets will wash off GCNFs from carbon felt surface, and the remaining carbon felt fibers will spread out water like a bare carbon felt sample.

After hot water treatment for 10 min, n-GCNF/SiC/carbon felt samples are wetted by water vapor, and water droplets immediately spread out along the sample surface. When this wetted n-GCNF/SiC/carbon felt sample is dried under vacuum at room temperature,

the dried sample regains its superhydrophobicity with water contact angle of $151^{o} \pm 3^{o}$ (Figure 27d). All these tests suggest that n-GCNF/SiC/carbon felt sample is a close mimic of lotus leaf for both hierarchical structure and reversible wetting properties between superhydrophobicity and hydrophilicity.

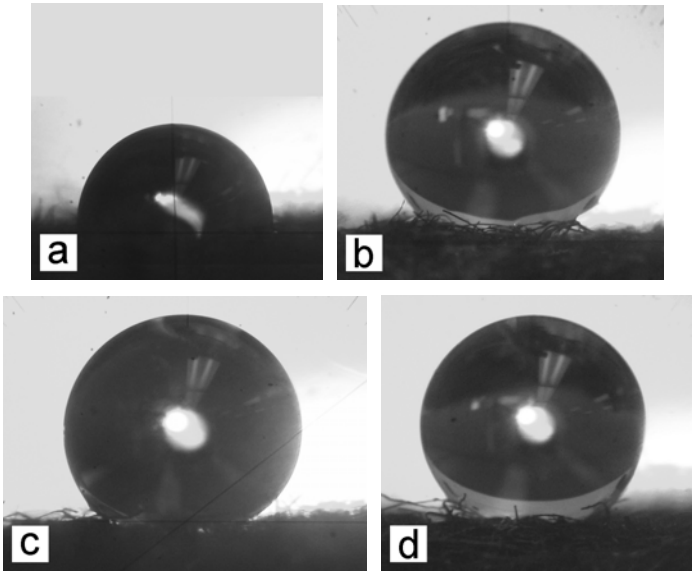

Figure 27. Contact-angle measurements of (a) as-received carbon felt, (b) n-GCNF/SiC/carbon felt, (c) n-GCNF/SiC/carbon felt after HF etching, and (d) n-GCNF/SiC/carbon felt after hot water treatment and vacuum drying.

Bulk density has been measured for carbon felt samples. According to IUPAC nomenclature, bulk density refers to the density of the material including pores and interparticle voids.[109] As-received carbon felt shows a bulk density of 0.64 ± 0.11 g/cm^3, while n-GCNF/SiC/carbon felt shows a bulk density of 0.11 ± 0.01 g/cm^3, only one fifth of the former. This large reduction of bulk density, coming from the nature of

superhydrophobicity, might be useful in marine applications.

6.4 Conclusions

Both narrow and wide herringbone-type GCNFs have been grown on carbon felt following the deposition of a catalyst precursor, in situ reduction of the growth catalyst, and carbonaceous gas decomposition, forming GCNF/carbon felt nanocomposites. Carbothermal treatment transforms catalyst silica support into silicon carbide, which dramatically increases the mechanical robustness of the resulting n-GCNF/SiC/carbon felt sample. TEED curves show little variation of work function for the various GCNF/carbon felt samples reported here. Contact-angle measurements confirm the superhydrophobicity of the n-GCNF/SiC/carbon felt sample and reversible wetting properties between superhydrophobicity and hydrophilicity with simple hot water treatment and vacuum drying, which closely mimics natural lotus leaves in both hierarchical structure and wetting properties.

CHAPTER VII

ASSEMBLY OF GCNF/CARBON PAPER NANOCOMPOSITES AS GAS DIFFUSION LAYERS IN FUEL CELLS

7.1 Introduction

Fuel cell technology has attracted great interest from the research and development communities due to the higher efficiency and much reduced emissions of fuel cells compared to internal combustion engines, both of which are promising for satisfying energy demand and environmental protection in the new century.[110-113] Six types of fuel cells have evolved in the past decades, including alkaline fuel cell (AFC), polymer electrolyte membrane fuel cell (PEMFC), direct methanol fuel cell (DMFC), phosphoric acid fuel cell (PAFC), molten carbonate fuel cell (MCFC) and solid oxide fuel cell (SOFC).[110] PEMFC (including its special case, DMFC) has been widely explored for automobile propulsion and for portable electronics as a replacement for lithium-ion batteries. In a typical single PEMFC (Figure 28), a polymer membrane is inserted between two gas diffusion layers (GDLs) coated with noble-metal catalyst, which is further sandwiched between two bipolar plates (gas flow plates).[110]

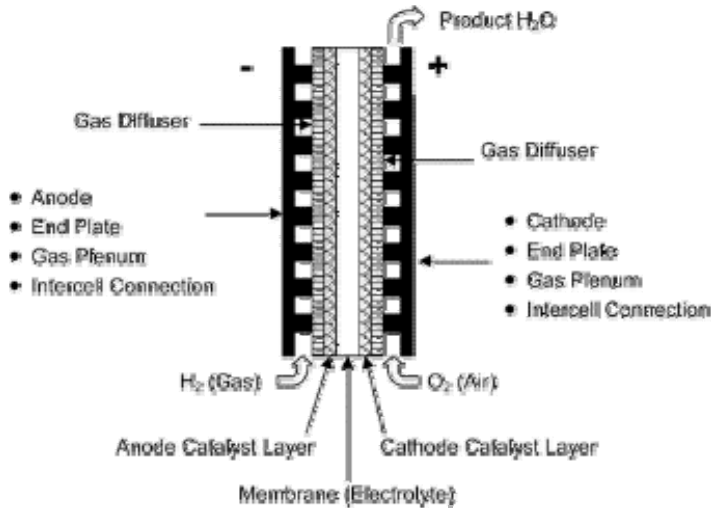

Figure 28. Schematic of a polymer electrolyte membrane fuel cell. Fuel options include pure hydrogen, methanol, natural gas, and gasoline. (Reprinted from ref 110. Copyright 2004 American Chemical Society.)

The high performance desired for PEM fuel cells imposes a combination of property requirements on materials to be used. For example, the polymer membrane, usually Nafion, has a combination of gas impermeability and proton conduction, while the gas diffusion layer needs to be electron conductive, gas permeable and hydrophobic. In a single PEM fuel cell, the electrical resistance between the two bipolar plates, mainly from the bulk resistance of the gas diffusion layers and from the contact resistance between GDLs and bipolar plates, imposes an undesired loss of cell output voltage,[114] which should be minimized. Carbon paper has been studied as a GDL, and there is a need to decrease GDL bulk resistance and GDL contact resistance with bipolar plates.[115,116]

Carbon nanomaterials have specific electrical, mechanical and chemical properties that make them ideal candidates for designing fuel cell components. For instance, carbon

nanofibers and nanotubes have been used as supports of noble metal catalysts for fuel cell electrodes.[6,10] So far, there are no studies using carbon nanostructures to improve GDL performance. It is suggested that GCNFs may be grown on carbon paper fibers. When GCNFs are long enough, they may connect with each other from different carbon paper fibers and decrease the bulk resistance of carbon paper and the contact resistance at the GDL/bipolar plate interface. In this study, herringbone-structure GCNFs with narrow or wide diameters have been grown on carbon paper, and the voltage drop of model cell assemblies, containing GCNF/carbon paper samples as gas diffusion layers, has been tested as a function of compression pressure.

7.2 Experimental Section

Samples of n-GCNF/SiO_2/carbon paper, n-GCNF/SiC/carbon paper and w-GCNF/carbon paper nanocomposites were prepared following the same procedure as Section 6.2.2 for those of n-GCNF/SiO_2/carbon felt, n-GCNF/SiC/carbon felt and w-GCNF/carbon felt nanocomposites, except the use of carbon paper (Toray TGP-H-060) instead of carbon felt as substrate.

Samples were examined by scanning electron microscopy (SEM) on a Hitachi S-4200 Electron Microscope with accelerating voltage at 5 kV. X-ray diffraction (XRD) scans were obtained using a Scintag X_1 θ/θ automated powder X-ray diffractometer with a Cu target, a Peltier-cooled solid-state detector, and a zero-background Si (510) support. Thermogravimetric analyses (TGA) were performed on a Thermal Analysis Instruments

High-Resolution TGA 2950 Thermogravimetric Analyzer with heating rate of 15 ^{o}C min^{-1} in an atmosphere of nitrogen. Temperature-programmed oxidation (TPO) analyses were performed in the same way except for the use of carbon dioxide as carrier gas. BET surface area analysis was determined from N_2 adsorption/desorption isotherms recorded with a Quantachrome NOVA 1000 high-speed surface-area analyzer.

Carbon paper was cut into standard squares of 1 1/8 inch and GCNF/carbon paper samples were prepared as described above and sent to Dana Corp. for resistance testing as gas diffusion layers. For this purpose, a resistance measurement setup, including gold plate/graphite bipolar layer/gas diffusion layer/graphite bipolar layer/gold plate, was assembled and compressed with a press applying a controlled force,[115] and the voltage drop of the assembly at different compression pressure was measured using a four-point method following ASTM C611, "Standard test method for electrical resistivity of manufactured carbon and graphite articles at room temperature".

7.3 Results and Discussion

7.3.1 As-received Carbon Paper

The morphology of as-received carbon paper samples has been examined by SEM. As shown in Figure 29a, carbon paper consists of straight carbon fibers with diameter of ca. 6 μm. According to the manufacturer, these micro-scale carbon paper fibers are bound together with unsaturated polyester resin binders, which are evident from the SEM

image.[117] After TPO treatment up to 900 ^{o}C, there are no visually obvious changes on carbon paper samples. But SEM images show that some degradation occurs (Figure 29b): (1) some polyester binder has been lost leaving more channels among carbon paper fibers, (2) some of the remaining binder cracks, (3) some carbon paper fibers have been either broken transversely or lost with voids left in the paper matrix, and (4) some separation between carbon paper fibers and polyester binders is observed, accounting for the loss of some fibers.

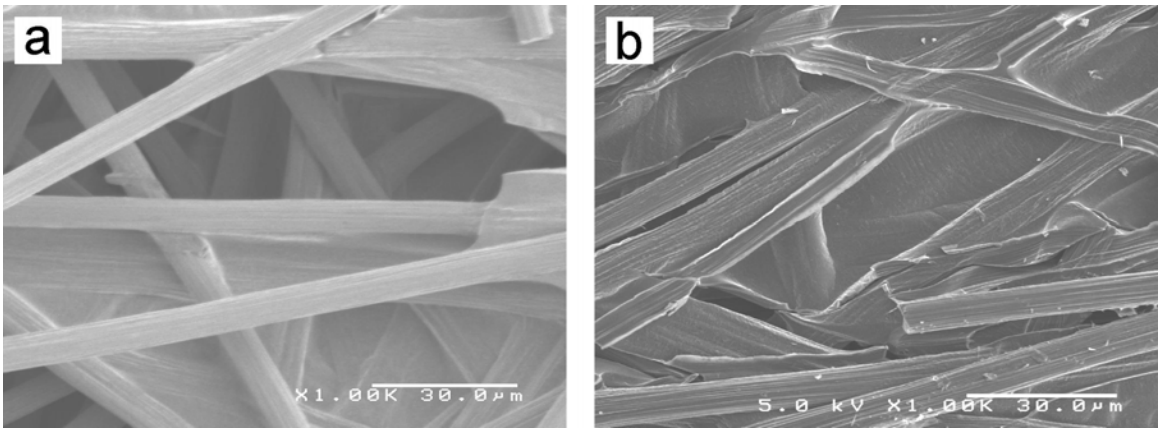

Figure 29. SEM images of as-received carbon paper (a) before and (b) after TPO treatment at 900 ^{o}C.

BET surface area of carbon paper increases from 9.2 m^2/g to 76.8 m^2/g after TPO treatment at 900 ^{o}C. This result is consistent with the SEM observation that TPO treatment opens more channels among the carbon paper fibers of the paper matrix.

By XRD (scan a in Figure 30), as-received carbon paper is made of highly crystalline

graphite (ICDD PDF # 41-1487). The peaks at 26.4°, 42.5°, 43.5°, 54.5°, and 86.8° can be assigned to (002), (100), (101), (004), and (006) crystal faces of graphite. The high intensity ratio of (002) peak to other peaks comes from the anisotropy of carbon paper fibers, meaning that carbon paper fibers are formed along the <002> direction. The crystalline nature of carbon paper is quite different from carbon felt, as the latter shows much lower X-ray diffraction intensities.

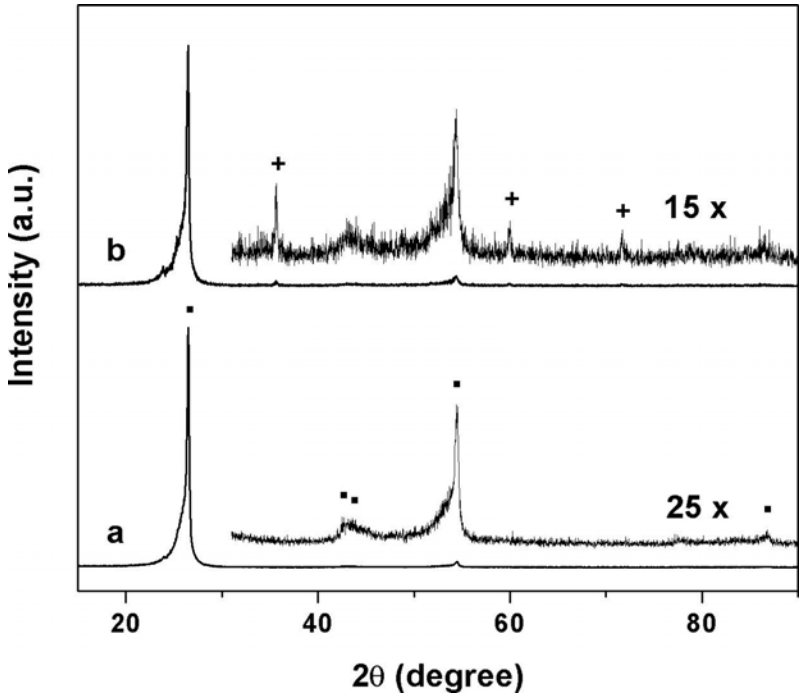

Figure 30. XRD scans of (a) as-received carbon paper and (b) n-GCNF/SiC/carbon paper samples. Peaks with (·) come from graphite phase while those indicated by (+) from silicon carbide phase.

The thermal stability of as-received carbon paper was examined by TGA and TPO. As shown with curve a in Figure 31, the TGA curve of carbon paper under nitrogen

shows mass gain until 850 ^{o}C, then a slight mass loss. It is known that crystalline graphite is quite stable until 850 ^{o}C, at which temperature the surface of graphite starts to oxidize. The mass loss above 850 ^{o}C can be seen for carbon paper, too. But the mass gain below 850 ^{o}C is quite surprising, since mass loss is expected due to loss of carbon paper fibers and polyester binders, shown in SEM (Figure 29b). The mass gain is tentatively assigned to surface oxidation of carbon paper fibers due to the presence of trace oxygen in nitrogen, forming ketone, phenol, and lactone groups as does graphite.[64,65] The TPO curve of carbon paper under CO_2 (curve b in Figure 31) shows the same trend of mass change as TGA curve with a larger mass gain (2.65% vs. 1.85%), consistent with the use of the oxidizing atmosphere under carbon dioxide carrier gas.

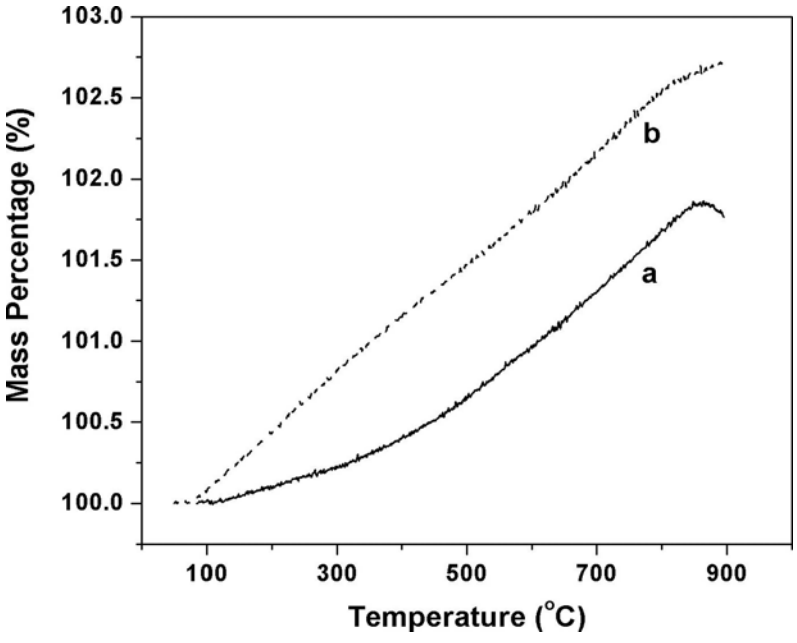

Figure 31. (a) TGA curve under nitrogen and (b) TPO curve under carbon dioxide of as-received carbon paper sample.

7.3.2 GCNF/Carbon Paper Nanocomposites

Similar to the carbon felt case (Chapter VI), GCNFs can be grown on the surface of carbon paper fibers. As shown in Figure 32a and 32b, narrow herringbone GCNFs can be grown on the carbon paper fibers, following the deposition of the growth catalyst precursor and in situ reduction process. The GCNFs wrap the carbon paper fibers tightly, forming a GCNF layer less than one micron, while some GCNFs are grown on the polyester binders. These GCNFs remain on the carbon paper fibers after carbothermal treatment at 1650 ^{o}C with the loss of polyester binders (Figure 32c and 32d). The resulting n-GCNF/SiC/carbon paper samples are quite mechanically robust and chemically stable, since there is little change after HCl etching treatment (images not shown).

Wide herringbone GCNFs were also grown on carbon paper substrate. The GCNFs mainly have diameters of 100-200 nm (Figure 32e and 32f), the same as diameters of free GCNF samples (Chapter II). Wide GCNFs are more likely to protrude from the carbon paper fibers, so GCNFs grown from different carbon paper fibers can connect with each other forming potential electron and heat transport pathways.

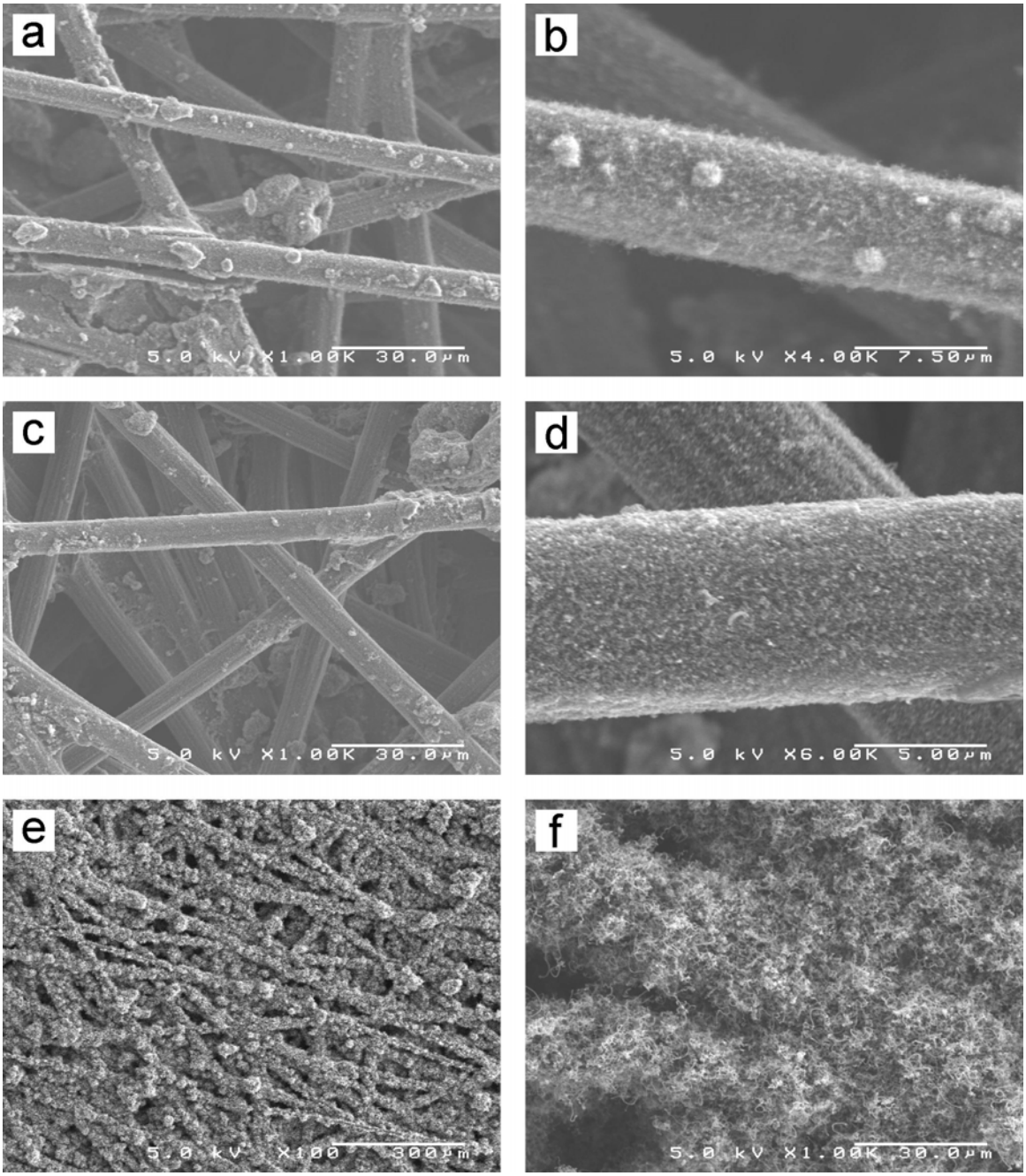

Figure 32. SEM images of (a, b) n-GCNF/SiO_2/carbon paper, (c, d) n-GCNF/SiC/ carbon paper and (e, f) w-GCNF/carbon paper samples.

XRD scans of n-GCNF/SiO_2/carbon paper and w-GCNF/carbon paper samples (data not shown) are similar to that of as-received carbon paper. The XRD scan (scan b in

Figure 30) of n-GCNF/SiC/carbon paper sample clearly shows the formation of the cubic 3C-SiC phase (ICDD PDF # 29-1129). The peaks at 35.6^{o}, 60.0^{o} and 71.8^{o} are assigned to the (111), (220) and (311) crystal faces of crystalline SiC.

7.3.3 Voltage Drop (Electrical Resistance) Measurements of GDL/Bipolar Plate Assemblies

Figure 33 shows changes in the voltage drop of a carbon paper control sample, of a n-GCNF/SiC/carbon paper sample, and of a w-GCNF/carbon paper sample at different compression pressures. The target is to reduce the voltage drop of a model cell assembly down to 10 mV at a reasonable pressure.[118] The voltage drop of an assembly, containing a standard size of carbon paper as gas diffusion layer, is about 24 mV at 100 kPa (ca. 1 atm) of pressure, and about 14 mV at 400 kPa of pressure. The reason for the decrease of voltage drop (electrical resistance) at larger compression pressure is that the compression increases the contact area on the micro-scale.

Similarly, the assembly containing the w-GCNF/carbon paper sample or the n-GCNF/SiC/carbon paper sample as a gas diffusion layer shows a large reduction of voltage drop with increasing compression pressure, which is consistent with test results for carbon paper. However, the assembly containing either GCNF/carbon paper sample shows larger voltage drops, meaning larger resistances, than carbon paper control sample for all the pressures tested.

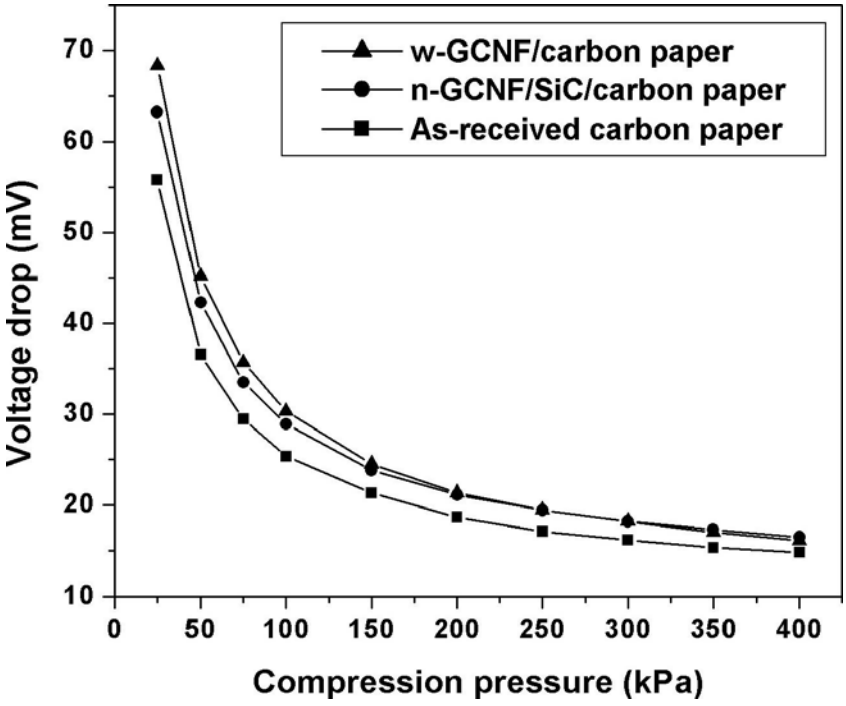

Figure 33. Voltage drop as a function of compression pressure on the model cell setup, containing carbon paper, n-GCNF/SiC/carbon paper or w-GCNF/carbon paper as a gas diffusion layer.

7.4 Conclusions

GCNF/carbon paper samples have been prepared with deposition of catalyst precursor, in situ reduction and carbonaceous gas decomposition. The resulting n-GCNF/SiO_2/carbon paper sample was transformed into n-GCNF/SiC/carbon paper via carbothermal treatment at 1650 ^oC, as confirmed from XRD scans. The latter exhibits superior mechanical robustness and chemical stability. In addition, w-GCNF/carbon paper was prepared, which contains wide GCNFs protruding away from the surface of carbon paper fibers. The n-GCNF/SiC/carbon paper and the w-GCNF/carbon paper samples have been assembled as a gas diffusion layer into a model cell in an effort to

decrease the electrical resistance of fuel cells. It is disappointing that the voltage drop (electrical resistance) of the model cell containing either GCNF/carbon paper sample is larger than a model cell containing carbon paper control sample.

APPENDIX A

GCNF/ANTIBODY CONJUGATION FOR CELL CAPTURE

1 Introduction

Various antibodies have been bound onto carbon nanotubes recently.[119-128] These CNT/antibody conjugates have been examined for detection of proteins[124-128] and cells[122,123] via antibody-antigen interactions with electrochemical, optical or microgravimetric methods. The advantages for binding antibodies to carbon nanotubes lie on the special properties of both components. First, carbon nanotubes possess high aspect ratio, specific surface electronic structure and superior electronic properties. Second, a monoclonal antibody can recognize one type of antigen with high specificity. The combination of these two advantages affords these tiny nanobiodevices high sensitivity with ease of nano-scale manipulation for applications such as early cancer diagnosis or speedy toxin detection.

Further, the mechanism of antibody binding to nanotubes have been determined, including physical adsorption (hydrophobic interactions),[119-125] electrostatic forces,[126,127] or covalent bonding.[128] Physical adsorption of antibodies onto carbon nanotubes has been studied[120-125] and the adsorption mechanism has been simulated.[119] The anti-fullerene IgG monoclonal antibody can specifically bind to SWNTs, and X-ray crystallography of the antibody Fab (fragment with antigen-binding sites) reveals that the binding cavity was

formed by clustering of hydrophobic amino acids.[120] Molecular dynamics simulation of a fullerene-antibody complex shows that the high binding affinity and specificity are achieved through complementary shape and extensive side-chain interactions, including a set of rich π-stacking interactions.[119] The aromatic rings in amino acid residues, including the benzene ring of phenylalanine (*Phe*) and tyrosine (*Tyr*) and 1-benzazole (indole) ring in tryptophan (*Trp*), can form π-stacking, sometimes triple π-stacking interactions with π-electron-rich carbon nanostructures, such as fullerenes, carbon nanotubes and carbon nanofibers.[119] Furthermore, H_ε atoms of some amino acid residues, for example *Trp*, may induce weak hydrogen bonding with the rich π-electrons of carbon nanostructures.[119]

Covalent bonding between single-walled nanotubes and anti-HSA antibodies has been claimed using coupling reagents of 1-(3-(dimethylamino)propyl)-3-ethylcarbodiimide (EDAC) and N-hydroxysulfosuccinimide (NHSS), but there is no characterization supporting this argument.[128] Another way to bind carbon nanotubes with antibodies is by using electrostatic forces, in which polyelectrolytes have been deposited onto the surface of nanotubes for binding oppositely charged antibodies.[126,127]

As discussed in the previous chapters, GCNFs possess specific physical and chemical properties. It is interesting to explore how antibodies will bind to GCNFs, especially when the latter has been functionalized with organic linker molecules. If antibodies can be effectively bound to GCNFs, the conjugates may be used for cell capture via antibody-antigen recognition with ease of preparation and manipulation of

GCNFs. In this study, the binding of rabbit IgG antibodies to surface-functionalized GCNF/ODA nanofibers with coupling of a bifunctional cross-linker, disuccinimidyl glutarate (DSG), has been attempted. The conjugated antibodies were detected with enzyme-linked immunosorbent assay (ELISA), a highly efficient immunoassay procedure.[129] Preliminary data reveal that antibodies are likely to bind with nanofibers via hydrophobic interactions, which make the cross-linker unnecessary.

2 Experimental Section

The following procedures were performed by Dr. Raymond L. Mernaugh. GCNF/ODA (2 mg) prepared as in Chapter II was mixed with rabbit IgG (Amersham Biosciences) in phosphate buffered saline (PBS, 0.1 M phosphate, 0.15 M NaCl, pH 7.2, Pierce) and then disuccinimidyl glutarate (DSG, Pierce) in DMSO was added. After incubation for 30 min at room temperature, the reaction mixture was quenched with Tris solution for 15 min and then filtered and washed with PBS to remove unbound antibodies. Four different concentrations (0, 0.02, 0.31, 2.5 mM) of DSG and eight concentrations (0, 1.56, 3.12, 6.25, 12.5, 25, 50, 100 μg/mL) of rabbit IgG were tested.

The amount of rabbit IgG bound to the nanofibers was determined using an ELISA procedure with an anti-rabbit IgG antibody conjugated with peroxidase, a peroxidase substrate and a color developer. The absorbance at 405 nm was recorded for the evaluation of antibody conjugation efficiency.

3 Results and Discussion

The amount of rabbit IgG conjugated on GCNF/ODA, as depicted from absorbance at 405 nm under ELISA assay, was plotted against IgG concentration in Figure 34. The amount of conjugated rabbit IgG increases with increasing IgG concentration. Saturation of GCNF/IgG conjugation is obtained at an IgG concentration of ca. 50 μg/mL, a value independent on the DSG concentration.

However, unexpected results are obtained when the concentration of DSG is varied from 0 to 2.5 mM. Without DSG or at very low concentration (0.02 mM), there is strong conjugation of IgG on GCNF/ODA nanofibers. With increasing concentration of DSG, lesser amounts of IgG are conjugated to GCNF/ODA nanofibers. At higher DSG concentration (12.5 mM) much less IgG conjugation occurs (data not shown).

It was expected that DSG, a cross-linker, would help link the free amino groups on the GCNF/ODA to the free amines on the rabbit IgG and that the amount of conjugated IgG would increase with higher DSG concentration. But the result is opposite and, in fact, use of a cross-linker inhibits rabbit IgG binding to the nanofibers. As discussed earlier, antibodies are likely to bind to carbon nanotubes via physical adsorption. In this study, it is possible that the rabbit IgG itself binds to GCNF/ODA via physical adsorption (double and triple π-stacking). The amino groups on GCNF/ODA nanofibers provide active sites for hydrogen bonding as well.

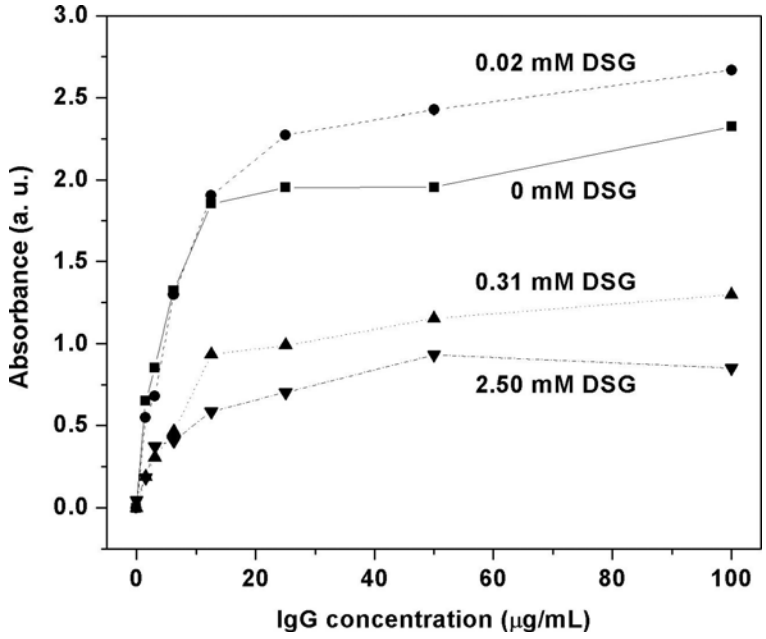

Figure 34. ELISA signal (absorbance at 405 nm) as a function of IgG concentration with different DSG concentrations.

4 Conclusions

In this chapter, conjugation of rabbit IgG antibodies onto GCNF/ODA surfaces with covalent linker molecule, disuccinimidyl glutarate, has been examined. ELISA assays confirm the surface attachment and give the amount of conjugated antibodies. It is shown that the amount of conjugated antibodies increases with increasing antibody concentration, but decreases with increasing cross-linker concentration. The results imply that it is not covalent bonding, but hydrophobic interactions that contribute to the attachment of antibodies onto GCNF/ODA nanofibers. Possible hydrophobic interactions include double or triple π-stacking and weak hydrogen bonding.

APPENDIX B

RADIOHALIDE ANION TRAPPING ON GCNF SURFACES FOR BIOIMAGING

1 Introduction

Bioimaging techniques have been continuously advanced for decades due to their paramount impact on clinical oncology diagnosis and biomedical research. Conventional imaging modalities, such as computed tomography (CT) or magnetic resonance imaging (MRI), detect morphologic changes of the target organ or tissue.[130,131] A novel imaging technique, positron emission tomography (PET), can monitor the changes in cell metabolism, providing more information for dynamic uses such as functional assessment of therapeutic effects.[132-134]

The basics of PET are to image and quantify in vivo distribution of positron-emitting radioisotopes such as fluorine-18, carbon-11, and oxygen-15 that can be substituted or added into radiotracers, that is, biologically relevant and specific receptor radioligands.[130] The PET technique relies on computerized reconstruction procedures to produce tomographic images by indirectly detecting positron emission.[130,132] Positrons (β^+), emitted by radioactive nuclei, collide with electrons within 1-2 mm and are annihilated. Each annihilation will produce two high-energy photons, which are emitted 180^o away from each other. The annihilation radiation can be detected externally and is used to measure both the quantity and the location of the positron emitter. Simultaneous detection

of two of these photons by detectors on opposite sides of an object locates the site of the annihilation on or about a line connecting the centers of the two opposing detectors. The distribution of annihilations is mapped by computer and the tomographic images obtained. PET has been widely used for cancer diagnosis and receptor expression owing to its higher resolution in spite of restrictions, such as the requirement of an on-site cyclotron, special radiosynthesis facilities and short half-lives of the radionuclides used.[130]

There are two groups of radiotracers of interest. The first comprises "general" tracers for non-specific cell metabolism, such as protein synthesis, amino acid transport, nucleic acid synthesis or membrane component synthesis.[135] For example, 2-[^{18}F]fluoro-2-deoxy-D-glucose (FDG), the only PET tracer used for routine cancer imaging, can enter cell membranes using the same transporter as glucose and thus accumulates inside the cell, in proportion to the metabolism of glucose.[135] The second group consists of "specific" tracers for target receptor expression based on antibody-antigen recognition.[135]

Research on nanomaterials has attracted a lot of interests from physicists, chemists, material scientists and biologists due to their novel electronic, magnetic, optical, chemical and biological properties. The integration of nanoscience and nanotechnology into the biological area has stimulated the development of a new research area: nanobiotechnology. For example, superparamagnetic iron oxide nanoparticles have been tested as tracers in MRI with high sensitivity and spatial resolution.[136] Given the broad research of cellular penetration of carbon nanomaterials,[137] it is proposed that carbon

nanostructures labeled with radionuclides may be used as “general” PET tracers, and even as “specific” tracers for receptor expression with antibodies attached to the surface of carbon nanomaterials.

In this study, radiohalide anion trapping on surface-functionalized GCNFs has been realized. The amino groups on GCNF/ODA surfaces has been transformed into quaternary ammonium cation after amide coupling with 1-[bis(dimethylamino)methylene]-1*H*-benzotriazolium tetrafluoroborate 3-oxide (TBTU), a highly efficient peptide coupling reagent,[138] and methylation with methyl trifluoromethanesulfonate (methyl triflate). The triflate anion is a good leaving group,[139] and it was exchanged with radioactive [^{18}F]fluoride or [^{123}I]iodide via sonication or stirring. The net trapping efficiency has been evaluated.

2 Experimental Section

To a GCNF/ODA sample (500 mg) was added the preformed solution of N,N-dimethylglycine (DMG, 78.9 mg, 0.764 mmol), 1-[bis(dimethylamino)methylene]-1*H*-benzotriazolium tetrafluoroborate 3-oxide (TBTU, 245.3 mg, 0.764 mmol), 1-hydroxybenzotriazole (HOBt, 103.2 mg, 0.764 mmol), and N,N-diisopropylethylamine (DIEA, 133.15 μL, 0.764 mmol) dissolved in DMF (2 mL).[138e] After stirring at room temperature for 24 h, the resulting mixture was filtered, and the solid was washed with DMF (3 × 10 mL) and THF (3 × 10 mL). Drying under vacuum afforded the compound **1** (472 mg, 94.4%) as depicted in Scheme 8.

To product **1** (400 mg) was added methyl triflate (40.2 μL, 0.367 mmol) and methylene chloride (6 mL) at 0 ^{o}C.[139a] After stirring for 1 h, the temperature was increased to room temperature and the reaction mixture was stirred for an additional 23 h. The resulting mixture was filtered and the solid was washed with methylene chloride (3 × 10 mL) and ether (3 × 10 mL). Drying under vacuum afforded compound **2** (378 mg, 94.5%).

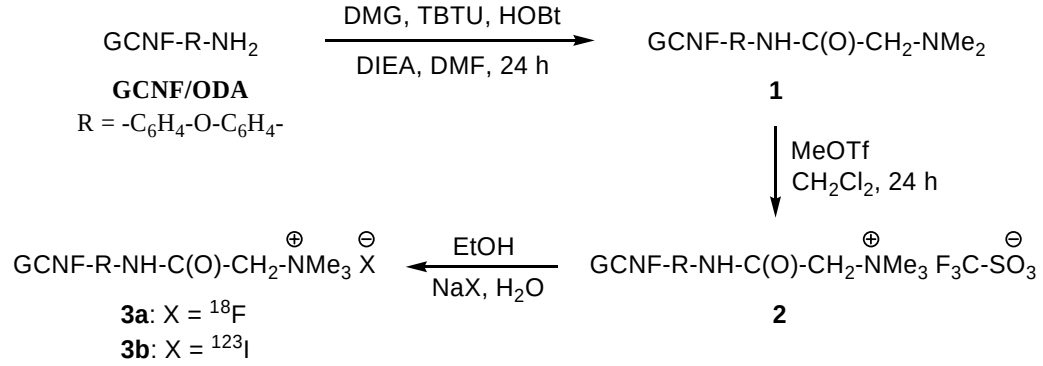

Scheme 8. Radiohalogen anion trapping on surface-functionalized GCNF materials.

The following radiohalide anion trapping procedures were performed by Dr. Ronald M. Baldwin. To nanofibers **2** in a vial were added ca. 100 μL of ethanol and aqueous sodium [^{18}F]fluoride or sodium [^{123}I]iodide solution. The mixture was incubated either by standing, sonication, or stirring for a desired time. Then the mixture was taken up into a syringe and filtered through a 0.45 μm PTFE membrane into a fresh vial. The filtrate, filter, and residue in the reaction vial and the syringe were assayed for radioactivity in an ion chamber (Capintec CRC-12, dial setting 485). All radioactivity measurements were

decay-corrected to a common time (half-life, 110 min for ^{18}F and 13.2 h for ^{123}I). Radionuclide distribution percentages, P_l, P_s and P_r, were calculated as the fractions of radioactivities from the filtrate liquid, from the solid on the filter, and from the residue in the reaction vial and the syringe, divided by the sum of all the radioactive components (Table 7). Net trapping was calculated as the percentage of radioactivity on the filter minus the percentage of radioactivity left in the vial (residual entrainment).

Table 7. Conditions for radiohalogen trapping and radioactivity distribution

Run No.	Fiber mass (mg)	NaX solution (mL)	Method	Time (h)	P_l (%)	P_s (%)	P_r (%)
	[^{18}F]fluoride trapping						
1	12.4	2.10	Standing	0.17	92	4	4
2	2.5	0.35	Sonication	0.50	81	12	7
3	20.6	0.43	Stirring	3.75	85	10	5
	[^{123}I]iodide trapping						
4	3.4	0.40	Sonication	0.17	70	22	8
5	14.7	0.60	Stirring	19.33	6	83	11

3 Results and Discussion

Net trapping percentages of [^{18}F]fluoride and [^{123}I]iodide on functionalized GCNFs **2**

were compared in Figure 35. There is no net trapping of [^{18}F]fluoride without sonication nor stirring, since it is relatively hard for ions to diffuse into GCNFs. With sonication for 0.50 h or with stirring for 3.75 h, there is 5% net trapping of [^{18}F]fluoride onto functionalized GCNFs. Comparison of these two ion exchange experiments is not appropriate, since the amounts of GCNFs and solution volumes are different.

Given the low net trapping percentage of [^{18}F]fluoride onto GCNFs, [^{123}I]iodide solution was used because its half-life is nearly one factor of magnitude longer than that of [^{18}F]fluoride. For iodide ion exchange with sonication for 0.17 h, the net trapping is 14%, a value better than those from fluoride exchange with either sonication or stirring. For iodide-ion exchange with stirring for 19.33 h, the net trapping reaches 72%, a value much better than all other values.

Apparently, the time of ion exchange is a key factor since ion diffusion onto the GCNF surface is the rate-determining step. The difficulty for ion diffusion probably comes from the lyophilic/hydrophobic nature and spontaneous aggregation of GCNFs. It is anticipated that more hydrophilic surface functionalization, addition of surfactants, or using mixed organic/aqueous solutions may help ion diffusion onto GCNF surfaces and improve the net trapping efficiency of radiohalide ions.

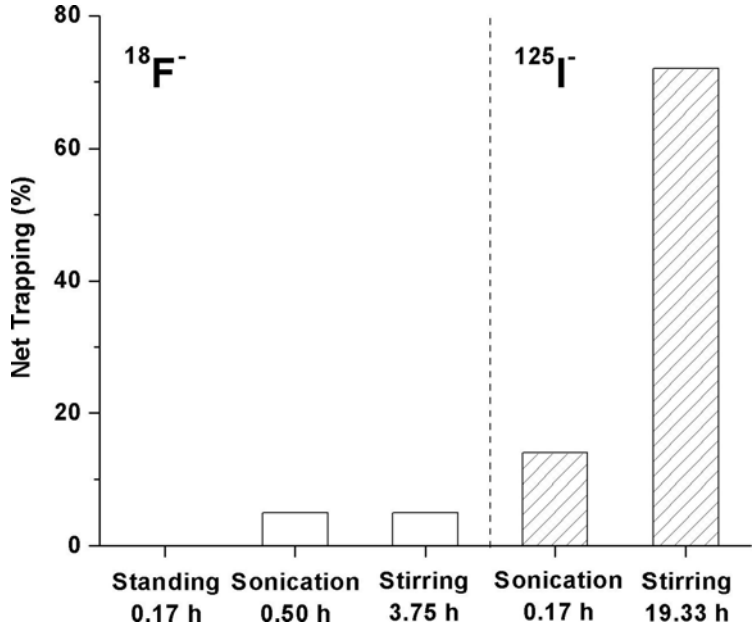

Figure 35. Net trapping percentages of radiohalides on GCNF materials.

4 Conclusions

Radiohalide anion trapping in GCNF materials has been explored following surface functionalization of GCNFs. The amino groups on GCNF/ODA surface have been transformed into quaternary ammonium cations after amide coupling with a glycine derivative and methylation by methyl triflate. The triflate anion in the resulting product was replaced with radioactive [^{18}F]fluoride or [^{123}I]iodide via sonication or stirring. The radiohalide net trapping efficiency was much improved by increasing the exchange time but still needs further improvement for radionuclides having short half lives, such as [^{18}F]fluoride.

APPENDIX C

IR SPECTRA, LDI MASS SPECTRA, AND TGA CURVES OF AS-PREPARED, OXIDIZED AND FUNCTIONALIZED GCNF MATERIALS

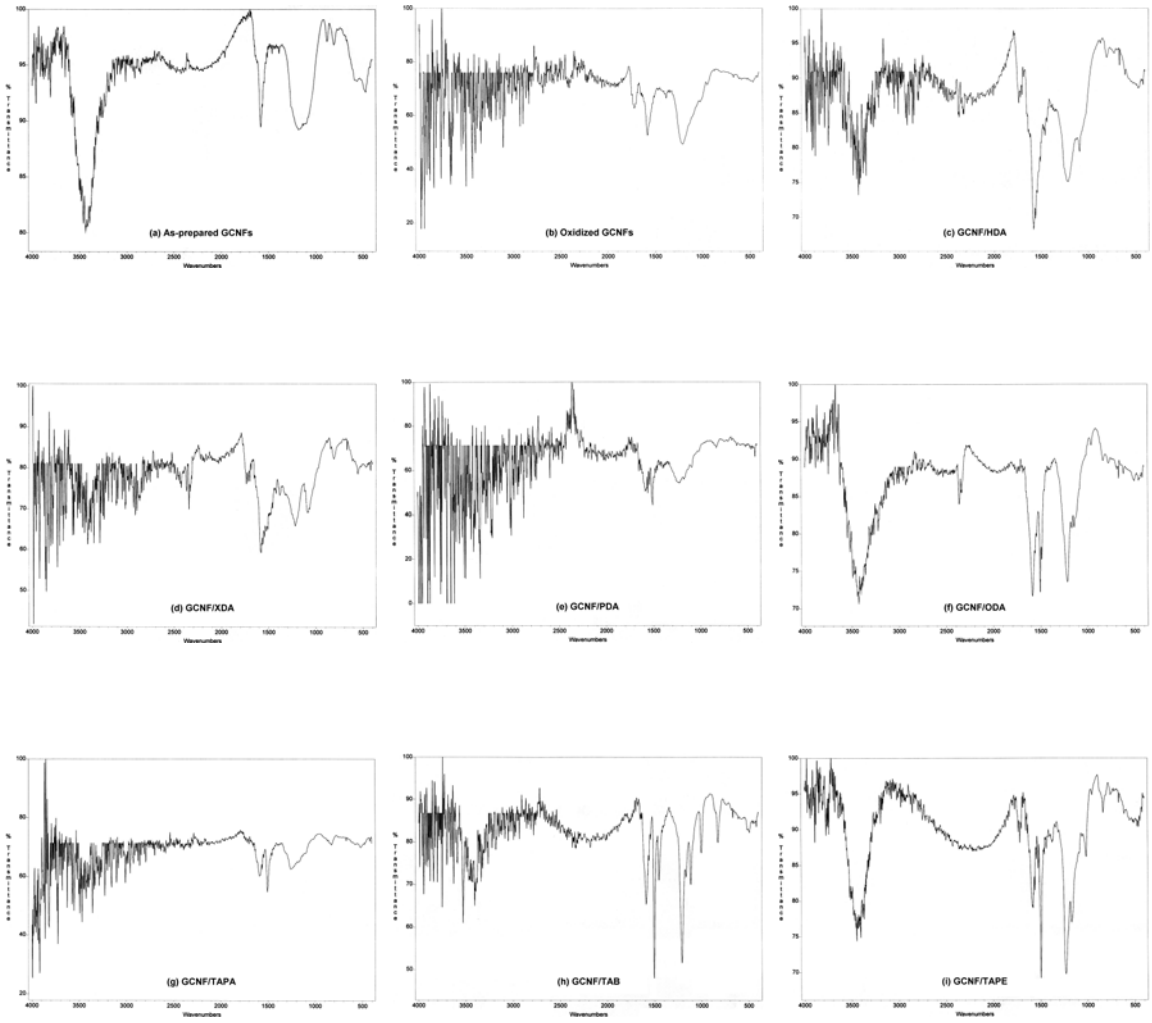

Figure 36. IR Spectra of (a) as-prepared GCNFs and (b) oxidized GCNFs, and of (c) GCNF/HDA, (d) GCNF/XDA, (e) GCNF/PDA, (f) GCNF/ODA, (g) GCNF/TAPA, (h) GCNF/TAB, and (i) GCNF/TAPE materials.

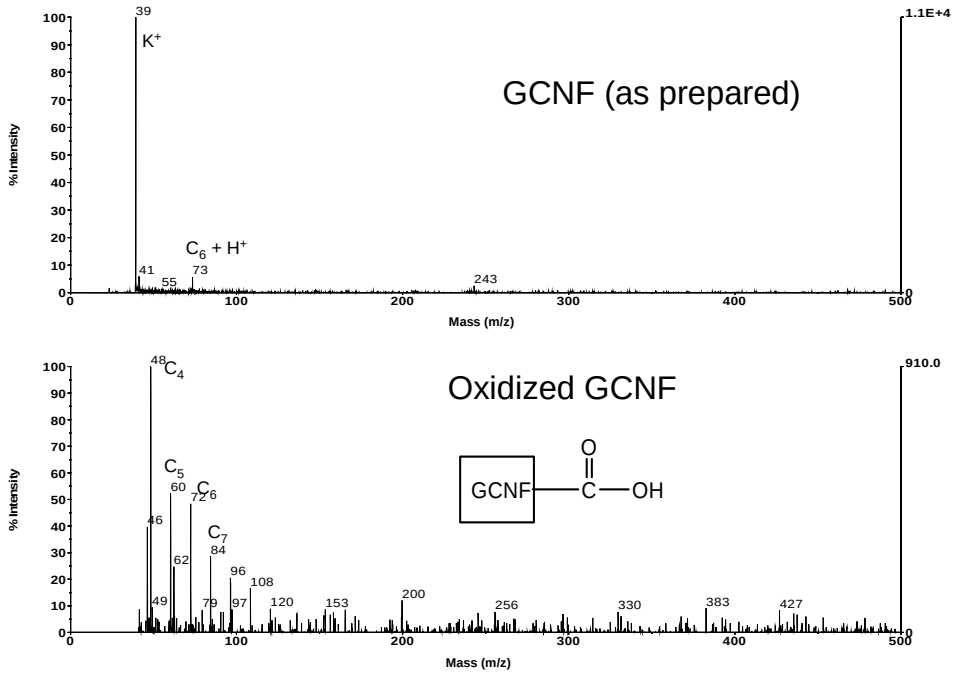

Figure 37. LDI mass spectra of (a) as-prepared GCNFs and (b) oxidized GCNFs.

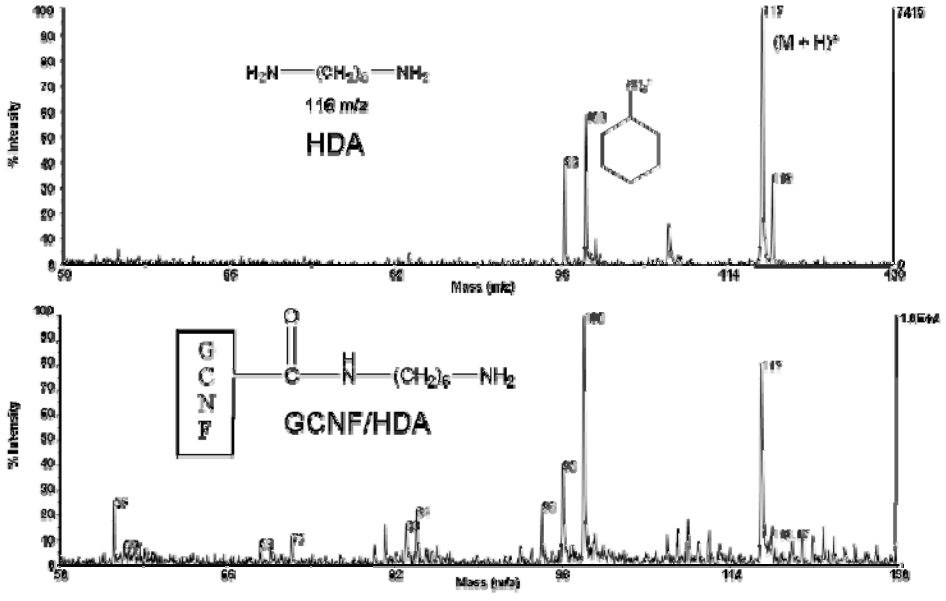

Figure 38. LDI mass spectra of (a) pure HDA and (b) GCNF/HDA.

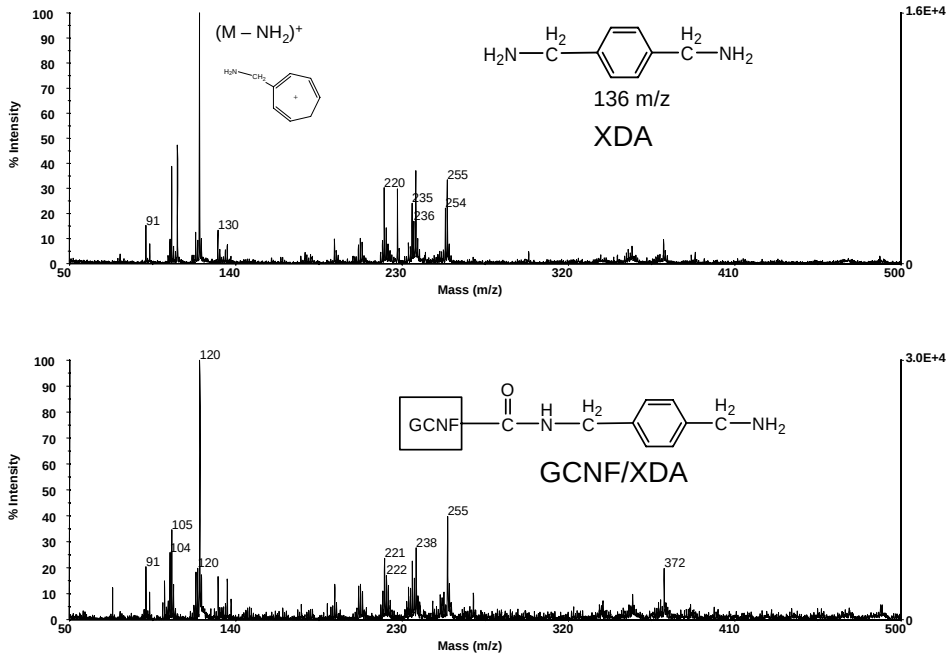

Figure 39. LDI mass spectra of (a) pure XDA and (b) GCNF/XDA.

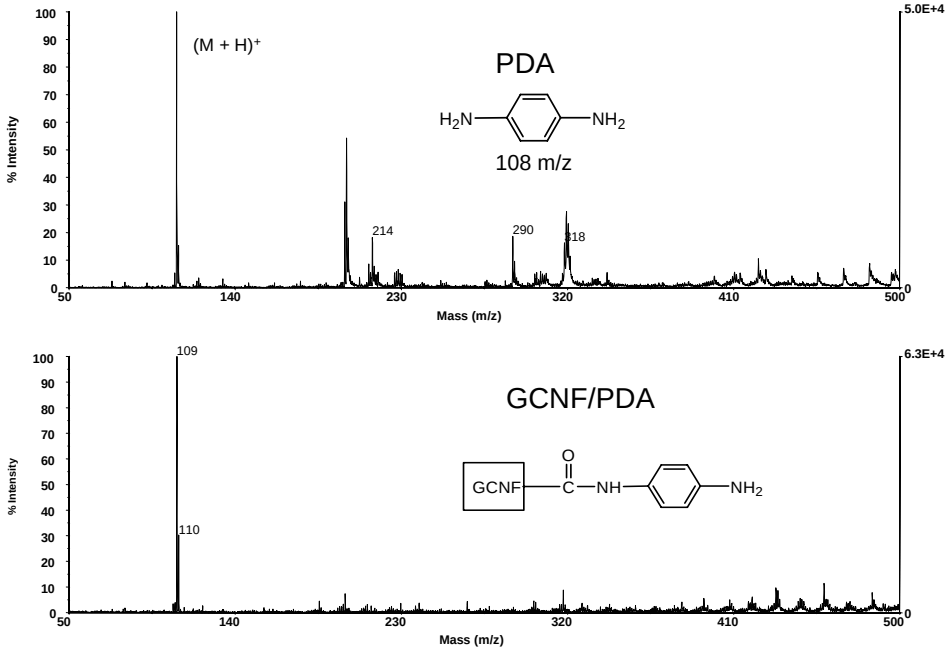

Figure 40. LDI mass spectra of (a) pure PDA and (b) GCNF/PDA.

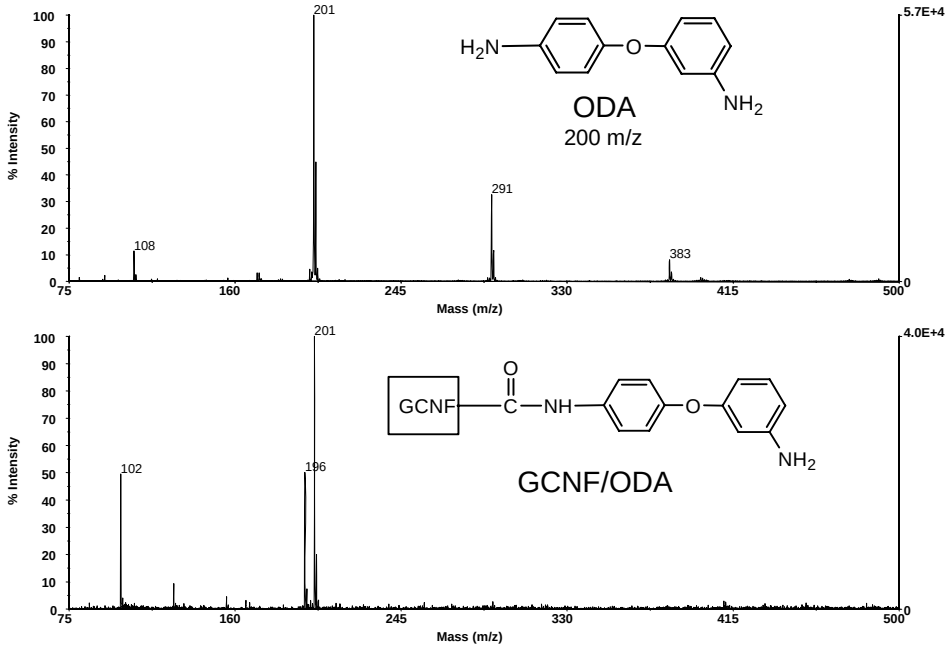

Figure 41. LDI mass spectra of (a) pure ODA and (b) GCNF/ODA.

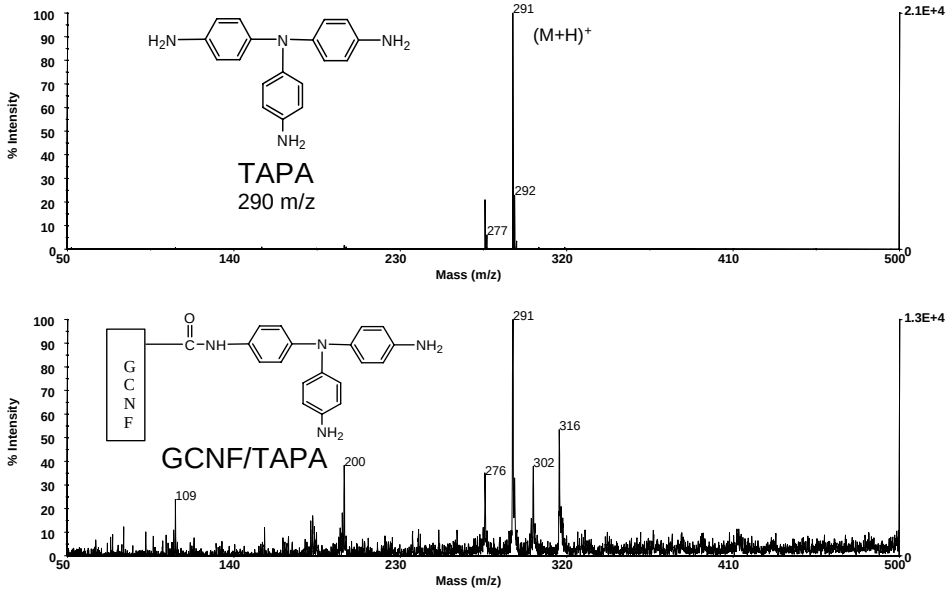

Figure 42. LDI mass spectra of (a) pure TAPA and (b) GCNF/TAPA.

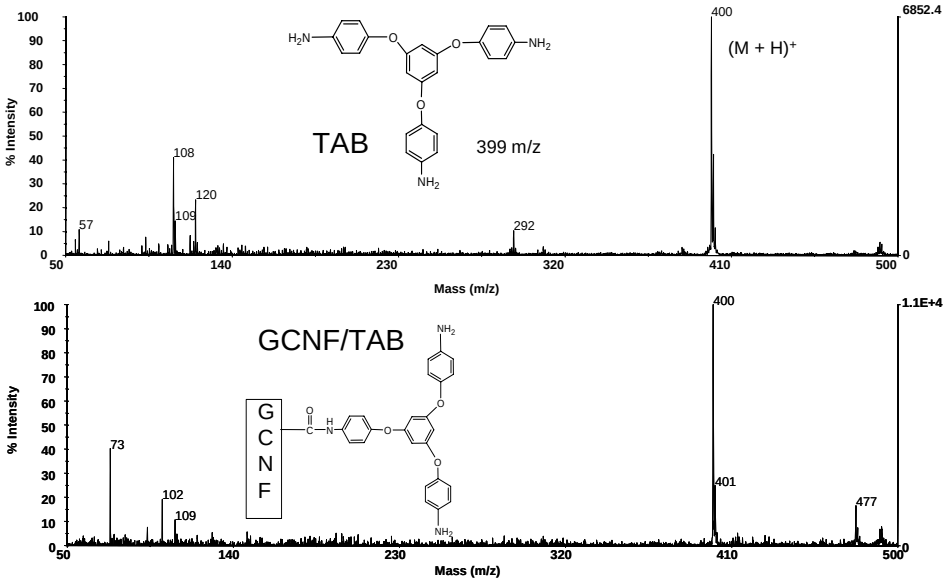

Figure 43. LDI mass spectra of (a) pure TAB and (b) GCNF/TAB.

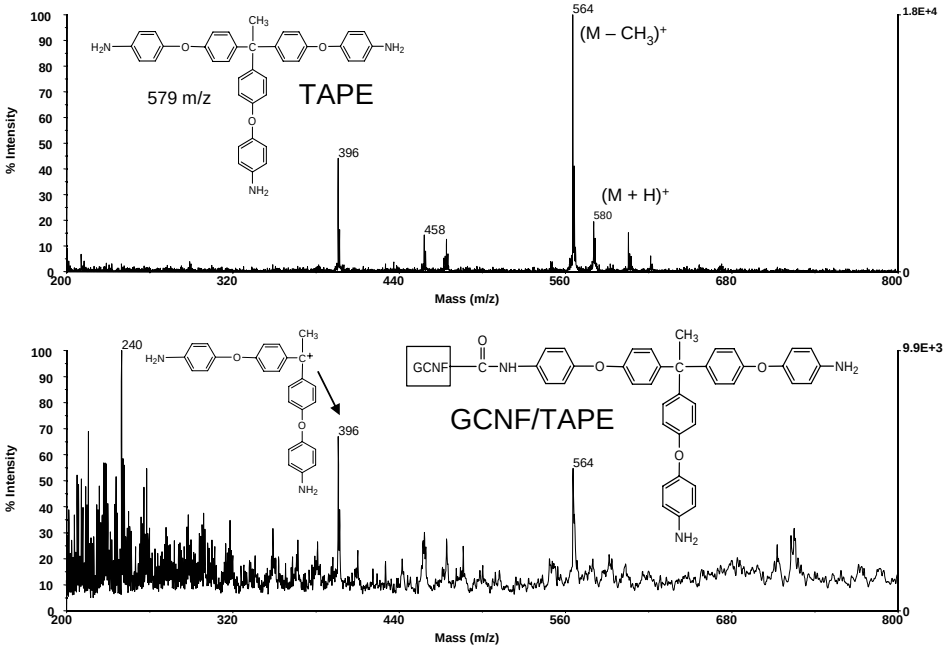

Figure 44. LDI mass spectra of (a) pure TAPE and (b) GCNF/TAPE.

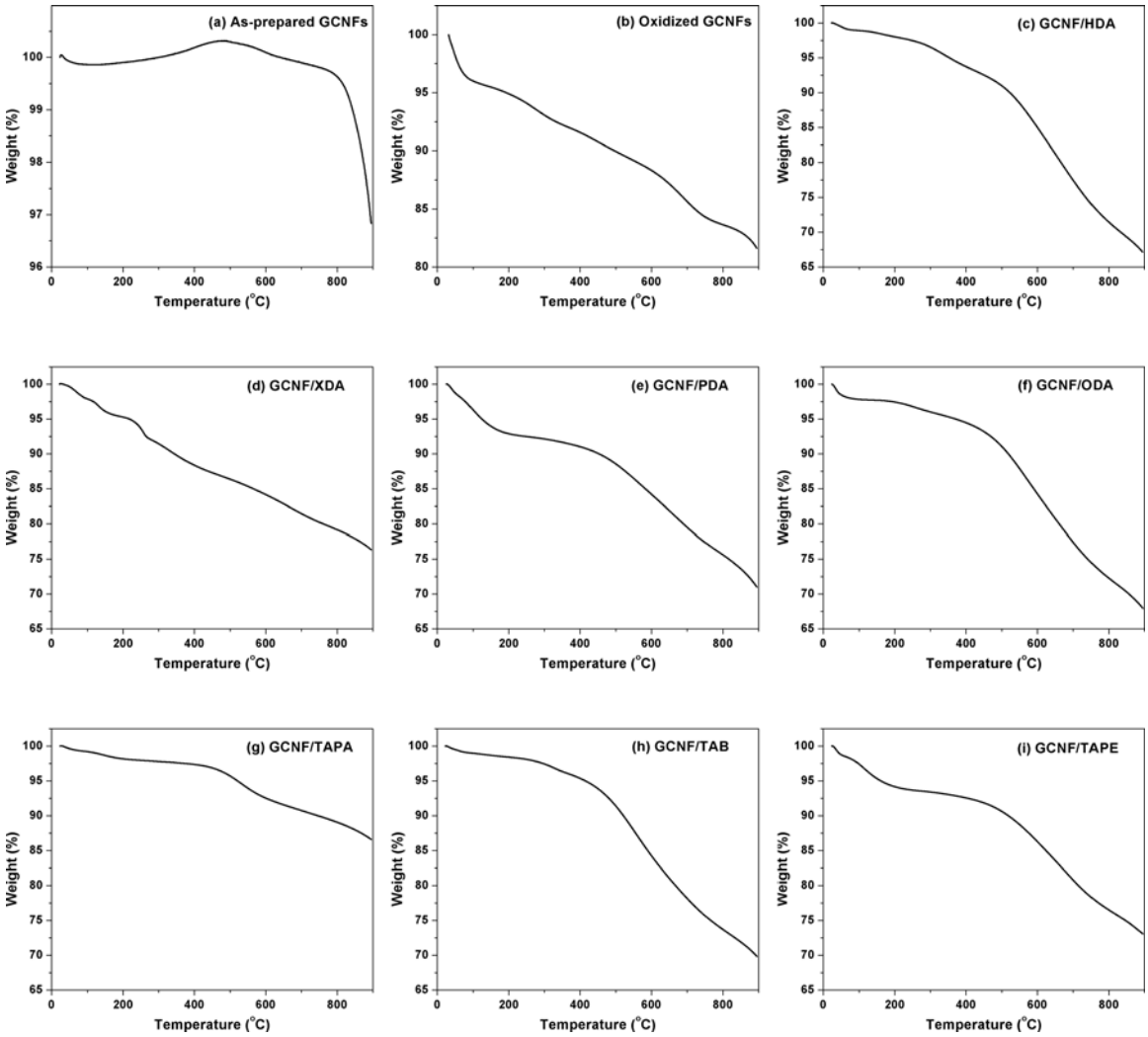

Figure 45. TGA curves of (a) as-prepared GCNFs and (b) oxidized GCNFs, and of (c) GCNF/HDA, (d) GCNF/XDA, (e) GCNF/PDA, (f) GCNF/ODA, (g) GCNF/TAPA, (h) GCNF/TAB, and (i) GCNF/TAPE materials in an atmosphere of nitrogen.

APPENDIX D

GROWTH MECHANISM OF CARBON NANOFIBERS AND NANOTUBES

It is of importance to have many types of carbon nanofibers and nanotubes, which provide structural variety for use in diverse applications. On the other hand, it is critical to selectively grow a desired structure, which requires knowledge about the growth mechanisms of these nanostructures.

Many studies have been conducted to explore the growth mechanism and now, most studies agree on the following three-step mechanism: (1) dissociative adsorption of carbon-containing compounds on favorable crystal facets of metal catalyst particles, (2) diffusion of adsorbed carbon atoms along the surface and subsurface of metal catalyst particles to those crystal facets favoring graphene precipitation, and (3) precipitation of carbon atoms on the crystal facets forming the carbon nanostructures.[8-10] The main driving forces lie in the following points: (1) those carbon-containing compounds are likely to adsorb on metal surface because the total energy of the system will be lowered with heat release during chemical adsorption, and (2) adsorbed carbon atoms are likely to aggregate into graphene layers, also because the total energy will be reduced due to the large heat of formation of graphite.[9] Overall, the steps are highly thermodynamically favorable.

It is relatively well known that, based on studies of heterogeneous catalysis,

dissociative adsorption of carbon-containing compounds occurs on metal catalyst particles. For the case of carbon nanostructure growth, compounds being applied range from hydrocarbons to carbon oxides, including methane, ethane, ethylene, acetylene, carbon monoxide, carbon dioxide, benzene, toluene, naphthalene, and even ethanol. All of them can dissociatively adsorb onto metal surfaces leading to surface carbon atoms and hydrogen release. Also it is well studied that carbon atoms may selectively adsorb on specific crystal faces of metal particles. For example, molecular orbital calculations indicate that the (100) and (110) faces of nickel exhibit stronger affinities for CO decomposition, while the (111) and (311) faces provide stronger epitaxial fits with graphite and favor graphene layer precipitation.[140] Furthermore, defect sites, such as step edges, on the favorable faces are more likely to adsorb those carbon atoms due to their unsaturated coordination and higher surface energy.[9,141]

There is much more controversy surrounding the second step, carbon diffusion. It is argued that the concentration gradient of carbon on different faces drives carbon diffusion to occur. The problem is whether carbon atoms diffuse along the surface of or inside the bulk of catalyst particles. Baker, et. al. suggest that bulk diffusion of carbon atoms within the catalyst particles can explain carbon filament formation.[7] This has been confirmed by the detection of cementite, Fe_3C, and extended to explicate the formation of other carbon structures.[142] It has been argued recently, however, that the cementite may form during the cooling process of the metal catalyst and surrounding carbon structures. *In situ* TEM images and selected area electron diffraction patterns confirm the presence of elemental

metal particles without change of crystal face spacing.[8,143,144] *Ab initio* density functional theory (DFT) simulations suggest the diffusion of carbon atoms along the surface and subsurface is preferred, considering the activation energy barrier for surface and subsurface diffusion, 1.5 eV, is much lower than that for bulk diffusion, 2.33 eV.[9,145] The idea of surface diffusion has been more accepted.

It is not surprising that there are different explanations for the third step, carbon precipitation, consisting of two stages, nucleation and growth. When carbon atoms arrive at crystal faces favorable for precipitation, carbon atoms are likely to bind together to form a graphene layer, given the high heat of formation of graphite. The size of the catalyst particles determines the morphology of the first graphene layer. On large catalyst particles of tens or hundreds of nanometers, a flat graphene layer forms due to lower strain energy, with which carbon nanofibers are likely to form.[146] With reduced catalyst size (a few to tens of nanometers), fullerene hemispheres may form since the edge carbon atoms along fullerene hemisphere can be stabilized due to interactions with surface metal atoms.[146] If a flat graphene layer forms, the high ratio of edge carbon atoms will result in more dangling bonds and higher surface energy.[143] For catalyst sizes less than 5 nm, only one layer of fullerene hemisphere can form and single-walled carbon nanotubes will grow with the size and helicicity consistent with the pre-formed fullerene hemisphere.[147] Simulations have quantitatively confirmed that graphene layers of very small size are likely to form curvatures with the introduction of pentagonal structural units in place of hexagonal ones.[148] Undoubtedly, there is an overlapping of catalyst size suitable for

growth of SWNTs and MWNTs (around 5-10 nm) and for growth of MWNTs and carbon nanofibers (tens of nanometers).

There are more factors which need further study. For example, some researchers argue that the catalyst may be an undercooled supersaturated metal-carbon alloy, which will favor the transport of metal and carbon atoms.[149,150] But the idea of molten catalyst may not be supported considering that the reaction temperature is mostly much lower than binary metal-carbon eutectic temperature, even corrected for size effects. Nonetheless, the presence of a molten alloy catalyst cannot be excluded at higher reaction temperature above 1000 ^{o}C. Also, MWNTs have been made without any catalyst, raising questions as to the role of catalyst. Other factors, such as composition of carbonaceous gas, presence of hydrogen and ammonia, composition of catalyst, temperature, and substrate effects, may influence the growth of carbon nanostructures as well.[147]

Overall, the adsorption-diffusion-precipitation mechanism has been confirmed from experimental evidences and theoretical simulation, although elucidation of the detailed mechanism of each step will require additional study.

REFERENCES

1. Rodriguez, N. M. *J. Mater. Res.* **1993**, *8*, 3233-3250.

2. De Jong, K. P.; Geus, J. W. *Catal. Rev.* **2000**, *42*, 481-510.

3. Rodriguez, N. M.; Chambers, A.; Baker, R. T. K. *Langmuir* **1995**, *11*, 3862-3866.

4. Bessel, C. A.; Laubernds, K.; Rodriguez, N. M.; Baker, R. T. K. *J. Phys. Chem. B* **2001**, *105*, 1115-1118.

5. Carneiro, O. C.; Kim, M. S.; Yim, J. B.; Rodriguez, N. M.; Baker, R. T. K. *J. Phys. Chem. B* **2003**, *107*, 4237-4244.

6. (a) Steigerwalt, E. S. *Preparation and characterization of novel nanocomposite materials*. Ph.D. Thesis, Vanderbilt University, 2001. (b) Mowles, E. D. *Surface functionalization of VGCNFs with pendant amino groups*. M.S. Thesis, Vanderbilt University, 2001.

7. Baker, R. T. K.; Barber, M. A.; Waite, R. J.; Harris, P. S.; Feates, F. S. *J. Catal.* **1972**, *26*, 51-62.

8. Helveg, S.; Lopez-Cartes, C.; Sehested, J.; Hansen, P. L.; Clausen, B. S.; Rostrup-Nielsen, J. R.; Abild-Pedersen, F.; Norskov, J. K. *Nature* **2004**, *427*, 426-429.

9. Abild-Pedersen, F.; Norskov, J. K.; Rostrup-Nielsen, J. R.; Sehested, J.; Helveg, S. *Phys. Rev. B* **2006**, *73*, 115419.

10. Boskovic, B. O.; Stolojan, V.; Khan, R. U. A.; Haq, S.; Silva, S. R. P. *Nat. Mater.* **2002**, *1*, 165-168.

11. Ngo, Q.; Cassell, A. M.; Austin, A. J.; Li, J.; Krishnan, S.; Meyyappan, M.; Yang, C. Y. *IEEE Electron Device Lett.* **2006**, *27*, 221-224.

12. Kimura, T.; Koizumi, H.; Kinoshita, H.; Ichikawa, T. *Nucl. Instrum. Methods Phys. Res., Sect. B* **2005**, *236*, 474-481.

13. Kikuchi, I.; Maruyama, I.; Fujii, T.; Kobayashi, T.; Kim, S. H.; Kim, D. U.; Lee, S. K. *Thin Solid Films* **2006**, *503*, 219-223.

14. Jacobsen, R. L.; Tritt, T. M.; Guth, J. R.; Ehrlich, A. C.; Gillespie, D. J. *Carbon* **1995**, *33*, 1217-1221.

15. Nakagawa, H.; Shudo, A.; Miura, K. *J. Electrochem. Soc.* **2000**, *147*, 38-42.

16. Park, C.; Anderson, P. E.; Chambers, A.; Tan, C. D.; Hidalgo, R.; Rodriguez, N. M. *J. Phys. Chem. B* **1999**, *103*, 10572-10581.

17. Walter, K. C.; Kung, H. H.; Maggiore, C. J. *Appl. Phys. Lett.* **1997**, *71*, 1320-1322.

18. Xu, Y.; Zondlo, J. W.; Finklea, H. O.; Brennsteiner, A. *Fuel Process Technol.* **2000**, *68*, 189-208.

19. Boxall, D. L.; Deluga, G. A.; Kenik, E. A.; King, W. D.; Lukehart, C. M. *Chem. Mater.* **2001**, *13*, 891-900.

20. Boxall, D. L.; Lukehart, C. M. *Chem. Mater.* **2001**, *13*, 806-810.

21. Steigerwalt, E. S.; Deluga, G. A.; Cliffel, D. E.; Lukehart, C. M. *J. Phys. Chem. B* **2001**, *105*, 8097-8101.

22. Marken, F.; Gerrard, M. L.; Mellor, I. M.; Mortimer, R. J.; Madden, C. E.; Fletcher, S.; Holt, K.; Foord, J. S.; Dahm, R. H.; Page, F. *Electrochem. Commun.* **2001**, *3*, 177-180.

23. Iijima, S. *Nature* **1991**, *354*, 56-58.

24. Dai, L. M.; Mau, A. W. H. *Adv. Mater.* **2001**, *13*, 899-913.

25. Ajayan, P. M. *Chem. Rev.* **1999**, *99*, 1787-1799.

26. (a) Dresselhaus M.S., Dresselhaus G.D., Avouris P. *Carbon Nanotubes: Synthesis, Structure, and Applications;* Springer-Verlag: Berlin, 2001; pp 392. (b) Saito, R.; Fujita, M.; Dresselhaus, G.; Dresselhaus, M. S. *Mater. Sci. Eng., B* **1993**, *19*, 185-191. (c) Journet, C.; Bernier, P. *Appl. Phys. A: Mater. Sci. Process.* **1998**, *67*, 1-9. (d) Huang, J. Y.; Chen, S.; Wang, Z. Q.; Kempa, K.; Wang, Y. M.; Jo, S. H.; Chen, G.; Dresselhaus, M. S.; Ren, Z. F. *Nature* **2006**, *439*, 281-281.

27. (a) Banerjee, S.; Wong, S. S. *J. Am. Chem. Soc.* **2004**, *126*, 2073-2081. (b) O'Connell, M. J.; Eibergen, E. E.; Doorn, S. K. *Nat. Mater.* **2005**, *4*, 412-418.

28. (a) Strano, M. S. *J. Am. Chem. Soc.* **2003**, *125*, 16148-16153. (b) Usrey, M. L.; Lippmann, E. S.; Strano, M. S. *J. Am. Chem. Soc.* **2005**, *127*, 16129-16135.

29. (a) Chattopadhyay, D.; Galeska, L.; Papadimitrakopoulos, F. *J. Am. Chem. Soc.* **2003**, *125*, 3370-3375. (b) Kim, S. N.; Luo, Z. T.; Papadimitrakopoulos, F. *Nano. Lett.* **2005**, *5*, 2500-2504.

30. Ziegler, K. J.; Schmidt, D. J.; Rauwald, U.; Shah, K. N.; Flor, E. L.; Hauge, R. H.; Smalley, R. E. *Nano. Lett.* **2005**, *5*, 2355-2359.

31. Tasis, D.; Tagmatarchis, N.; Bianco, A.; Prato, M. *Chem. Rev.* **2006**, *106*, 1105-1136.

32. Hirsch, A. *Angew. Chem. Int. Edit.* **2002**, *41*, 1853-1859.

33. Guo, X. F.; Huang, L. M.; O'Brien, S.; Kim, P.; Nuckolls, C. *J. Am. Chem. Soc.* **2005**, *127*, 15045-15047.

34. Kroto, H. W.; Heath, J. R.; Obrien, S. C.; Curl, R. F.; Smalley, R. E. *Nature* **1985**, *318*, 162-163.

35. (a) Taylor, R.; Walton, D. R. M. *Nature* **1993**, *363*, 685-693. (b) Guldi, D. M. *Chem. Soc. Rev.* **2002**, *31*, 22-36. (c) Prato, M. *J. Mater. Chem.* **1997**, *7*, 1097-1109.

36. Umemoto, K.; Saito, S.; Berber, S.; Tomanek, D. *Phys. Rev. B* **2001**, *64*, 193409.

37. Lee, J.; Sohn, K.; Hyeon, T. *J. Am. Chem. Soc.* **2001**, *123*, 5146-5147.

38. Amma, A.; Razavi, B.; St Angelo, S. K.; Mayer, T. S.; Mallouk, T. E. *Adv. Funct. Mater.* **2003**, *13*, 365-370.

39. Tang, Y. H.; Zhang, P.; Kim, P. S.; Sham, T. K.; Hu, Y. F.; Sun, X. H.; Wong, N. B.; Fung, M. K.; Zheng, Y. F.; Lee, C. S.; Lee, S. T. *Appl. Phys. Lett.* **2001**, *79*, 3773-3775.

40. Viculis, L. M.; Mack, J. J.; Kaner, R. B. *Science* **2003**, *299*, 1361-1361.

41. Thien-Nga, L.; Hernadi, K.; Forro, L. *Adv. Mater.* **2001**, *13*, 148-150.

42. Huang, L. C. L.; Chang, H. C. *Langmuir* **2004**, *20*, 5879-5884.

43. Liu, Y.; Gu, Z. N.; Margrave, J. L.; Khabashesku, V. N. *Chem. Mater.* **2004**, *16*, 3924-3930.

44. Darmstadt, H.; Roy, C.; Kaliaguine, S.; Kim, T. W.; Ryoo, R. *Chem. Mater.* **2003**, *15*, 3300-3307.

45. Li, J.; Vergne, M. J.; Mowles, E. D.; Zhong, W. H.; Hercules, D. M.; Lukehart, C. M. *Carbon* **2005**, *43*, 2883-2893.

46. Zhong, W. H.; Li, J.; Xu, L. Y. R.; Michel, J. A.; Sullivan, L. M.; Lukehart, C. M. *J. Nanosci. Nanotechnol.* **2004**, *4*, 794-802.

47. Zhong, W. H.; Li, J.; Lukehart, C. M.; Xu, L. Y. R. *Polym. Compos.* **2005**, *26*, 128-135.

48. Xu, L. R.; Bhamidipati, V.; Zhong, W. H.; Li, J.; Lukehart, C. M.; Lara-Curzio, E.; Liu, K. C.; Lance, M. J. *J. Compos. Mater.* **2004**, *38*, 1563-1582.

49. Zhamu, A.; Hou, Y.; Zhong, W. H.; Stone, J. J.; Li, J.; Lukehart, C. M. **2006**, Submitted for publication.

50. Li, J.; Lukehart, C. M. *Compos. Interfaces* **2004**, *11*, 525-535.

51. Niyogi, S.; Hamon, M. A.; Hu, H.; Zhao, B.; Bhowmik, P.; Sen, R.; Itkis, M. E.; Haddon, R. C. *Acc. Chem. Res.* **2002**, *35*, 1105-1113.

52. O'Connell, M. J.; Boul, P.; Ericson, L. M.; Huffman, C.; Wang, Y. H.; Haroz, E.; Kuper, C.; Tour, J.; Ausman, K. D.; Smalley, R. E. *Chem. Phys. Lett.* **2001**, *342*, 265-271.

53. Islam, M. F.; Rojas, E.; Bergey, D. M.; Johnson, A. T.; Yodh, A. G. *Nano. Lett.* **2003**, *3*, 269-273.

54. (a) Hamon, M. A.; Chen, J.; Hu, H.; Chen, Y. S.; Itkis, M. E.; Rao, A. M.; Eklund, P. C.; Haddon, R. C. *Adv. Mater.* **1999**, *11*, 834-840. (b) Chen, J.; Hamon, M. A.; Hu, H.; Chen, Y. S.; Rao, A. M.; Eklund, P. C.; Haddon, R. C. *Science* **1998**, *282*, 95-98.

55. (a) Hamon, M. A.; Hu, H.; Bhowmik, P.; Niyogi, S.; Zhao, B.; Itkis, M. E.; Haddon, R. C. *Chem. Phys. Lett.* **2001**, *347*, 8-12. (b) Huang, W. J.; Fernando, S.; Allard, L. F.; Sun, Y. P. *Nano. Lett.* **2003**, *3*, 565-568. (c) Bahr, J. L.; Yang, J. P.; Kosynkin, D. V.; Bronikowski, M. J.; Smalley, R. E.; Tour, J. M. *J. Am. Chem. Soc.* **2001**, *123*, 6536-6542. (d) Holzinger, M.; Vostrowsky, O.; Hirsch, A.; Hennrich, F.; Kappes, M.; Weiss, R.; Jellen, F. *Angew. Chem. Int. Edit.* **2001**, *40*, 4002-4005. (e) Banerjee, S.; Kahn, M. G. C.; Wong, S. S. *Chem. Eur. J.* **2003**, *9*, 1899-1908.

56. (a) Georgakilas, V.; Tagmatarchis, N.; Pantarotto, D.; Bianco, A.; Briand, J. P.; Prato, M. *Chem. Commun.* **2002**, 3050-3051. (b) Lin, Y.; Rao, A. M.; Sadanadan, B.; Kenik, E. A.; Sun, Y. P. *J. Phys. Chem. B* **2002**, *106*, 1294-1298. (c) Eitan, A.; Jiang, K. Y.; Dukes, D.; Andrews, R.; Schadler, L. S. *Chem. Mater.* **2003**, *15*, 3198-3201. (d) Zhang, N. Y.; Xie, J. N.; Guers, M.; Varadan, V. K. *Smart. Mater. Struct.* **2003**, *12*, 260-263.

57. (a) Lakshminarayanan, P. V.; Toghiani, H.; Pittman, C. U. *Carbon* **2004**, *42*, 2433-2442. (b) Bubert, H.; Ai, X.; Haiber, S.; Heintze, M.; Bruser, V.; Pasch, E.;

Brandl, W.; Marginean, G. *Spectrochim. Acta, Part B* **2002**, *57*, 1601-1610. (c) Paredes, J. I.; Martinez-Alonso, A.; Tascon, J. M. D. *Carbon* **2002**, *40*, 1101-1108. (d) Wei, G.; Fujiki, K.; Saitoh, H.; Shirai, K.; Tsubokawa, N. *Polym. J.* **2004**, *36*, 316-322.

58. Sun, Y. P.; Lawson, G. E.; Huang, W. J.; Wright, A. D.; Moton, D. K. *Macromolecules* **1999**, *32*, 8747-8752.

59. Pittman, C. U.; He, G. R.; Wu, B.; Gardner, S. D. *Carbon* **1997**, *35*, 317-331.

60. (a) Tada, T.; Mano, K.; Yoshida, E.; Tanaka, N.; Kunugi, S. *Bull. Chem. Soc. Jpn.* **2002**, *75*, 2247-2251. (b) Ngo, T. T. *Appl. Biochem. Biotechnol.* **1986**, *13*, 213-219. (c) Tyllianakis, P. E.; Kakabakos, S. E.; Evangelatos, G. P.; Ithakissios, D. S. *Appl. Biochem. Biotechnol.* **1993**, *38*, 15-25.

61. Sarin, V. K.; Kent, S. B. H.; Tam, J. P.; Merrifield, R. B. *Anal. Biochem.* **1981**, *117*, 147-157.

62. Fields, G. B.; Noble, R. L. *Int. J. Pept. Prot. Res.* **1990**, *35*, 161-214.

63. Miller, R. D.; Burland, D. M.; Jurich, M.; Lee, V. Y.; Moylan, C. R.; Thackara, J. I.; Twieg, R. J.; Verbiest, T.; Volksen, W. *Macromolecules* **1995**, *28*, 4970-4974.

64. EinEli, Y.; Koch, V. R. *J. Electrochem. Soc.* **1997**, *144*, 2968-2973.

65. (a) Hontorialucas, C.; Lopezpeinado, A. J.; Lopezgonzalez, J. D. D.; Rojascervantes, M. L.; Martinaranda, R. M. *Carbon* **1995**, *33*, 1585-1592. (b) Sha, X. W.; Jackson, B. *J. Am. Chem. Soc.* **2004**, *126*, 13095-13099.

66. Creasy, W. R.; Zimmerman, J. A.; Ruoff, R. S. *J. Phys. Chem.* **1993**, *97*, 973-979.

67. Batich, C.; Yahiaoui, A. *J. Polym. Sci., Part A: Polym. Chem.* **1987**, *25*, 3479-3488.

68. Dang, T. A.; Gnanasekaran, R. *Surf. Interface Anal.* **1990**, *15*, 113-118.

69. (a) Scharff, P.; Xu, Z. Y.; Stumpp, E.; Barteczko, K. *Carbon* **1991**, *29*, 31-37. (b) Fillaux, F.; Menu, S.; Conard, J.; Fuzellier, H.; Parker, S. W.; Hanon, A. C.; Tomkinson, J. *Chem. Phys.* **1999**, *242*, 273-281. (c) Bower, C.; Kleinhammes, A.; Wu, Y.; Zhou, O. *Chem. Phys. Lett.* **1998**, *288*, 481-486.

70. Lozano, K.; Barrera, E. V. *J. Appl. Polym. Sci.* **2001**, 79, 125-133.

71. (a) Ge, J. J.; Zhang, D.; Li, Q.; Hou, H. Q.; Graham, M. J.; Dai, L. M.; Harris, F. W.; Cheng, S. Z. D. *J. Am. Chem. Soc.* **2005**, *127*, 9984-9985. (b) Zhao, B.; Hu, H.; Yu,

A. P.; Perea, D.; Haddon, R. C. *J. Am. Chem. Soc.* **2005**, *127*, 8197-8203. (c) Fang, W. L.; Chu, H. Y.; Hsu, W. K.; Cheng, T. W.; Tai, N. H. *Adv. Mater.* **2005**, *17*, 2987-2992. (d) Yang, Y. L.; Gupta, M. C. *Nano. Lett.* **2005**, *5*, 2131-2134. (e) Liu, P. *Eur. Polym. J.* **2005**, *41*, 2693-2703. (f) Xu, J.; Donohoe, J. P.; Pittman, C. U. *Composites, Part A* **2004**, *35*, 693-701. (g) Carneiro, O. S.; Maia, J. M. *Polym. Compos.* **2000**, 21, 961-969.

72. Pogue, R. T.; Ye, J.; Klosterman, D. A.; Glass, A. S.; Chartoff, R. P. *Composites, Part A* **1998**, 29, 1273-1281.

73. Patton, R. D.; Pittman, C. U. Jr.; Wang, L.; Hill, J. R. *Composites, Part A* **1999**, 30, 1081-1091.

74. Cooper, C. A.; Ravich, D.; Lips, D.; Mayer, J.; Wagner, H. D. *Compos. Sci. Technol.* **2002**, 62, 1105-1112.

75. (a) Sandler, J.; Werner, P.; Shaffer, M. S. P.; Demchuk, V.; Altstadt, V.; Windle, A. H. *Composites, Part A* **2002**, 33, 1033-1039. (b) Werner, P.; Verdejo, R.; Wollecke, F.; Altstadt, V.; Sandler, J. K. W.; Shaffer, M. S. P. *Adv. Mater.* **2005**, *17*, 2864-2869.

76. Pan, Y. X.; Yu, Z. Z.; Ou, Y. C.; Hu, G. H. *J. Polym. Sci., Part B: Polym. Phys.* **2000**, 38, 1626-1633.

77. Paxton, J. P.; Mowles, E. D.; Lukehart, C. M.; Witzig, A. J. In *Proceedings of the American Society for Composites, Technical Conference*, 2001; Vol. 16, pp 565-571.

78. (a) Lukaszczyk, J.; Jaszcz, K. *Polimery* **1999**, *44*, 56-58. (b) Lukaszczyk, J.; Jaszcz, K. *Macromol. Chem. Phys.* **2002**, *203*, 301-308. (c) Ikeda, I.; Horie, N.; Suzuki, K. *J. Appl. Polym. Sci.* **1994**, *51*, 1931-1935.

79. (a) Hoshii, S.; Kojima, A.; Tamaki, T.; Otani, S. *J. Mater. Sci. Lett.* **2000**, *19*, 557-560. (b) Bianchi, V.; Goursat, P.; Sinkler, W.; Monthioux, M.; Menessier, E. *J. Eur. Ceram. Soc.* **1997**, *17*, 1485-1500. (c) Sinkler, W.; Monthioux, M.; Bianchi, V.; Goursat, P.; Menessier, E. *J. Eur. Ceram. Soc.* **1999**, *19*, 305-316. (d) Lamouroux, F.; Bertrand, S.; Pailler, R.; Naslain, R.; Cataldi, M. *Compos. Sci. Technol.* **1999**, *59*, 1073-1085. (e) Dhakate, S. R.; Parashar, V. K.; Raman, V.; Bahl, O. P.; Sahare, P. D. *J. Mater. Sci. Lett.* **2000**, *19*, 1575-1577.

80. (a) Wang, X. T.; Padture, N. P.; Tanaka, H. *Nat. Mater.* **2004**, *3*, 539-544. (b) Zhan, G. D.; Kuntz, J. D.; Wan, J. L.; Mukherjee, A. K. *Nat. Mater.* **2003**, *2*, 38-42. (c) Zhan, G. D.; Kuntz, J. D.; Garay, J. E.; Mukherjee, A. K. *Appl. Phys. Lett.* **2003**, *83*, 1228-1230. (d) Peigney, A.; Flahaut, E.; Laurent, C.; Chastel, F.; Rousset, A. *Chem.*

Phys. Lett. **2002**, *352*, 20-25. (e) Flahaut, E.; Peigney, A.; Laurent, C.; Marliere, C.; Chastel, F.; Rousset, A. *Acta Mater.* **2000**, *48*, 3803-3812.

81. (a) Siegel, R. W.; Chang, S. K.; Ash, B. J.; Stone, J.; Ajayan, P. M.; Doremus, R. W.; Schadler, L. S. *Scr. Mater.* **2001**, *44*, 2061-2064. (b) Hwang, G. L.; Hwang, K. C. *J. Mater. Chem.* **2001**, *11*, 1722-1725. (c) Hernadi, K.; Ljubovic, E.; Seo, J. W.; Forro, L. *Acta Mater.* **2003**, *51*, 1447-1452. (d) Seeger, T.; de la Fuente, G.; Maser, W. K.; Benito, A. M.; Callejas, M. A.; Martinez, M. T. *Nanotechnology* **2003**, *14*, 184-187. (e) Weidenkaff, A.; Ebbinghaus, S. G.; Lippert, T. *Chem. Mat.* **2002**, *14*, 1797-1805.

82. (a) Xu, Y. S.; Chung, D. D. L. *Carbon* **2001**, *39*, 1995-2001. (b) Segiet, M.; Chung, D. D. L. *Compos. Interfaces* **2000**, *7*, 257-275. (c) Kim, J. H.; Shioya, M.; Nakatani, M. *Compos. Interfaces* **2001**, *7*, 443-458.

83. Wood, D. L.; Rabinovich, E. M. *Appl. Spectrosc.* **1989**, *43*, 263-267.

84. Almeida, R. M.; Pantano, C. G. *J. Appl. Phys.* **1990**, *68*, 4225-4232.

85. Perry, C. C.; Li, X. C. *J. Chem. Soc. Faraday Trans.* **1991**, *87*, 761-766.

86. Hontorialucas, C.; Lopezpeinado, A. J.; Lopezgonzalez, J. D. D.; Rojascervantes, M. L.; Martinaranda, R. M. *Carbon* **1995**, *33*, 1585-1592.

87. Kang, Y. J.; Taton, T. A. *J. Am. Chem. Soc.* **2003**, *125*, 5650-5651.

88. Niyogi, S.; Bekyarova, E.; Itkis, M. E.; McWilliams, J. L.; Hamon, M. A.; Haddon R. C. *J. Am. Chem. Soc.* **2006**, *128*, 7720-7721.

89. McKnight, T. E.; Melechko, A. V.; Hensley, D. K.; Mann, D. G. J.; Griffin, G. D.; Simpson, M. L. *Nano. Lett.* **2004**, *4*, 1213-1219.

90. Ye, Q.; Cassell, A. M.; Liu, H. B.; Chao, K. J.; Han, J.; Meyyappan, M. *Nano. Lett.* **2004**, *4*, 1301-1308.

91. Chopra, N.; Majumder, M.; Hinds, B. J. *Adv. Funct. Mater.* **2005**, *15*, 858-864.

92. Chen, X.; Zhang, Y.; Gao, X. P.; Pan, G. L.; Jiang, X. Y.; Qu, J. Q.; Wu, F.; Yan, J.; Song, D. Y. *Int. J. Hydrogen Energy* **2004**, *29*, 743-748.

93. Cao, P. J.; Gu, Y. S.; Liu, F.; Liu, H. W.; Zhang, H. R.; Shen, F.; Zhang, Q. F.; Zhong, D. Y.; Li, J. Q.; Liu, S.; Gao, H. J. *Appl. Phys. A* **2005**, *80*, 195-199.

94. Guo, X. F.; Small, J. P.; Klare, J. E.; Wang, Y. L.; Purewal, M. S.; Tam, I. W.; Hong, B. H.; Caldwell, R.; Huang, L. M.; O'Brien, S.; Yan, J. M.; Breslow, R.;

Wind, S. J.; Hone, J.; Kim, P.; Nuckolls, C. *Science* **2006**, *311*, 356-359.

95. Jung, S. H.; Jeong, S. H.; Kim, S. U.; Hwang, S. K.; Lee, P. S.; Lee, K. H.; Ko, J. H.; Bae, E.; Kang, D.; Park, W.; Oh, H.; Kim, J. J.; Kim, H.; Park, C. G. *Small* **2005**, *1*, 553-559.

96. Marty, L.; Bonnot, A. M.; Bonhomme, A.; Iaia, A.; Naud, C.; Andre, E.; Bouchiat, V. *Small* **2006**, *2*, 110-115.

97. Robinson, V. S.; Fisher, T. S.; Michel, J. A.; Lukehart, C. M. *Appl. Phys. Lett.* **2005**, *87*, 061501.

98. Hatsopoulos, G. N.; Gyftopoulos, E. P. *Thermioni Energy Conversion Vol I: Processes and Devices*; MIT: Cambridge, 1973; pp 12-14.

99. Shiraishi, M.; Ata, M. *Carbon* **2001**, *39*, 1913-1917.

100. Young, R. D. *Phys. Rev.* **1959**, *113*, 110-114.

101. Guo, Z. G.; Zhou, F.; Hao, J. C.; Liu, W. M. *J. Am. Chem. Soc.* **2005**, *127*, 15670-15671.

102. (a) Erbil, H. Y.; Demirel, A. L.; Avci, Y.; Mert, O. *Science* **2003**, *299*, 1377-1380. (b) Xie, Q. D.; Fan, G. Q.; Zhao, N.; Guo, X. L.; Xu, J.; Dong, J. Y.; Zhang, L. Y.; Zhang, Y. J.; Han, C. C. *Adv. Mater.* **2004**, *16*, 1830-1833. (c) Jiang, L.; Zhao, Y.; Zhai, J. *Angew. Chem. Int. Edit.* **2004**, *43*, 4338-4341. (d) Burton, Z.; Bhushan, B. *Nano. Lett.* **2005**, *5*, 1607-1613. (e) Zhai, L.; Cebeci, F. C.; Cohen, R. E.; Rubner, M. F. *Nano. Lett.* **2004**, *4*, 1349-1353. (f) Sun, T. L.; Feng, L.; Gao, X. F.; Jiang, L. *Acc. Chem. Res.* **2005**, *38*, 644-652.

103. Barthlott, W.; Neinhuis, C. *Planta* **1997**, *202*, 1-8.

104. Feng, L.; Li, S. H.; Li, Y. S.; Li, H. J.; Zhang, L. J.; Zhai, J.; Song, Y. L.; Liu, B. Q.; Jiang, L.; Zhu, D. B. *Adv. Mater.* **2002**, *14*, 1857-1860.

105. Cheng, Y. T.; Rodak, D. E. *Appl. Phys. Lett.* **2005**, *86*, 144101.

106. Cheng, Y. T.; Rodak, D. E.; Angelopoulos, A.; Gacek, T. *Appl. Phys. Lett.* **2005**, *87*, 194112.

107. Steigerwalt, E. S.; Deluga, G. A.; Lukehart, C. M. *J. Phys. Chem. B* **2002**, *106*, 760-766.

108. Lu, W. J.; Steigerwalt, E. S.; Moore, J. T.; Sullivan, L. M.; Collins, W. E.; Lukehart,

C. M. *J. Nanosci. Nanotechnol.* **2004**, *4*, 803-808.

109. Rouquerol, J.; Avnir, D.; Fairbridge, C. W.; Everett, D. H.; Haynes, J. H.; Pernicone, N.; Ramsay, J. D. F.; Sing, K. S. W.; Unger, K. K. *Pure Appl. Chem.* **1994**, *66*, 1739-1758.

110. Winter, M.; Brodd, R. J. *Chem. Rev.* **2004**, *104*, 4245-4269.

111. de Bruijn, F. *Green Chem.* **2005**, *7*, 132-150.

112. Carrette, L.; Friedrich, K. A.; Stimming, U. *Chemphyschem* **2000**, *1*, 162-193.

113. Lashway, R. W. *MRS Bull.* **2005**, *30*, 581-583.

114. Blunk, R. H. J.; Lisi, D. J.; Yoo, Y. E.; Tucker, C. L. *AIChE J.* **2003**, *49*, 18-29.

115. Mishra, V.; Yang, F.; Pitchumani, R. *J. Fuel Cell Sci. Tech.* **2004**, *1*, 2-9.

116. Williams, M. V.; Begg, E.; Bonville, L.; Kunz, H. R.; Fenton, J. M. *J. Electrochem. Soc.* **2004**, *151*, A1173-A1180.

117. www.torayca.com (accessed May 2006).

118. Steigerwalt, E. S. Private communication.

119. Noon, W. H.; Kong, Y. F.; Ma, J. P. *Proc. Natl. Acad. Sci. USA* **2002**, *99*, 6466-6470.

120. Erlanger, B. F.; Chen, B. X.; Zhu, M.; Brus, L. *Nano. Lett.* **2001**, *1*, 465-467.

121. O'Connor, M.; Kim, S. N.; Killard, A. J.; Forster, R. J.; Smyth, M. R.; Papadimitrakopoulos, F.; Rusling, J. F. *Analyst* **2004**, *129*, 1176-1180.

122. Lin, Y.; Elkin, T.; Taylor, S.; Gu, L. R.; Chen, B. L.; Veca, L. M.; Zhou, B.; Yang, H.; Brown, J.; Joseph, R.; Jones, E.; Jiang, X. P.; Sun, Y. P. *Microchim. Acta* **2006**, *152*, 249-254.

123. Huang, T. S.; Tzeng, Y.; Liu, Y. K.; Chen, Y. K.; Walker, K. R.; Guntupalli, R.; Liu, C. *Diam. Relat. Mater.* **2004**, *13*, 1098-1102.

124. Viswanathan, S.; Wu, L. C.; Huang, M. R.; Ho, J. A. A. *Anal. Chem.* **2006**, *78*, 1115-1121.

125. Kojima, A.; Hyon, C. K.; Kamimura, T.; Maeda, M.; Matsumoto, K. *Jpn. J. Appl. Phys. 1* **2005**, *44*, 1596-1598.

126. Rouhanizadeh, M.; Tang, T.; Li, C.; Hwang, J. L.; Zhou, C. W.; Hsiai, T. K. *Sens. Actuators, B* **2006**, *114*, 788-798.

127. Munge, B.; Liu, G. D.; Collins, G.; Wang, J. *Anal. Chem.* **2005**, *77*, 4662-4666.

128. Yu, X.; Kim, S. N.; Papadimitrakopoulos, F.; Rusling, J. F. *Mol. Biosyst.* **2005**, *1*, 70-78.

129. (a) Okennedy, R.; Byrne, M.; Ofagain, C.; Berns, G. *Biochem. Educ.* **1990**, *18*, 136-140. (b) Vann, W. F.; Sutton, A.; Schneerson, R. *Methods Enzymol.* **1990**, *184*, 537-541. (c) Clark, M. F.; Lister, R. M.; Barjoseph, M. *Methods Enzymol.* **1986**, *118*, 742-766. (d) Voller, A.; Bartlett, A.; Bidwell, D. E. *J. Clin. Pathol.* **1978**, *31*, 507-520.

130. Van Den Bossche, B.; de Wiele, C. V. *J. Clin. Oncol.* **2004**, *22*, 3593-3607.

131. Mason, N. S.; Mathis, C. A. *Neuroimag. Clin. N. Am.* **2003**, *13*, 671-687.

132. Stuckensen, T.; Kovacs, A. F.; Adams, S.; Baum, R. P. *J. Cranio-Maxill. Surg.* **2000**, *28*, 319-324.

133. Kitagawa, Y.; Nishizawa, S.; Sano, K.; Ogasawara, T.; Nakamura, M.; Sadato, N.; Yoshida, M.; Yonekura, Y. *J. Nucl. Med.* **2003**, *44*, 198-206.

134. Denecke, T.; Rau, B.; Hoffmann, K. T.; Hildebrandt, B.; Ruf, J.; Gutberlet, M.; Hunerbein, M.; Felix, R.; Wust, P.; Amthauer, H. *Eur. Radiol.* **2005**, *15*, 1658-1666.

135. Couturier, O.; Luxen, A.; Chatal, J. F.; Vuillez, J. P.; Rigo, P.; Hustinx, R. *Eur. J. Nucl. Med. Mol. I* **2004**, *31*, 1182-1206.

136. (a) Moore, A.; Grimm, J.; Han, B. Y.; Santamaria, P. *Diabetes* **2004**, *53*, 1459-1466. (b) Heyn, C.; Bowen, C. V.; Rutt, B. K.; Foster, P. J. *Magnet. Reson. Med.* **2005**, *53*, 312-320. (c) Malmstrom, P. U. *Acta Oncol.* **2005**, *44*, 593-598. (d) Paty, B. W.; Bonner-Weir, S.; Laughlin, M. R.; McEwan, J.; Shapiro, A. M. J. *Transplantation* **2004**, *77*, 1133-1137.

137. (a) Kam, N. W. S.; Liu, Z.; Dai, H. J. *J. Am. Chem. Soc.* **2005**, *127*, 12492-12493. (b) Kam, N. W. S.; Dai, H. J. *J. Am. Chem. Soc.* **2005**, *127*, 6021-6026. (c) Cai, D.; Mataraza, J. M.; Qin, Z. H.; Huang, Z. P.; Huang, J. Y.; Chiles, T. C.; Carnahan, D.; Kempa, K.; Ren, Z. F. *Nat. Methods* **2005**, *2*, 449-454. (d) Pantarotto, D.; Briand, J. P.; Prato, M.; Bianco, A. *Chem. Commun.* **2004**, 16-17. (e) Monch, I.; Meye, A.; Leonhardt, A.; Kramer, K.; Kozhuharova, R.; Gemming, T.; Wirth, M. P.; Buchner, B. *J. Magn. Magn. Mater.* **2005**, *290*, 276-278.

138. (a) Carpino, L. A.; Imazumi, H.; El-Faham, A.; Ferrer, F. J.; Zhang, C. W.; Lee, Y. S.; Foxman, B. M.; Henklein, P.; Hanay, C.; Mugge, C.; Wenschuh, H.; Klose, K.; Beyermann, M.; Bienert, M. *Angew. Chem. Int. Edit.* **2002**, *41*, 442-445. (b) Najera, C. *Synlett* **2002**, 1388-1403. (c) Albericio, F.; Carpino, L. A. *Solid-Phase Pept. Synth.* **1997**, *289*, 104-126. (d) Albericio, F.; Chinchilla, R.; Dodsworth, D. J.; Najera, C. *Org. Prep. Proced. Int.* **2001**, *33*, 205-303. (e) Albericio, F.; Bailen, M. A.; Chinchilla, R.; Dodsworth, D. J.; Najera, C. *Tetrahedron* **2001**, *57*, 9607-9613.

139. (a) Langer, O.; Dolle, F.; Valette, H.; Halldin, C.; Vaufrey, F.; Fuseau, C.; Coulon, C.; Ottaviani, M.; Nagren, K.; Bottlaender, M.; Maziere, B.; Crouzel, C. *Bioorgan. Med. Chem.* **2001**, *9*, 677-694. (b) Yin, D. Z.; Zhang, L.; Tang, G. H.; Tang, X. L.; Wang, Y. X. *J. Radioanal. Nucl. Ch.* **2003**, *257*, 179-185. (c) Kevill, D. N.; Anderson, S. W. *J. Heterocyclic Chem.* **1988**, *25*, 399-402.

140. Yang, R. T.; Chen, J. P. *J. Catal.* **1989**, *115*, 52-64.

141. (a) Jarrah, N. A.; van Ommen, J. G.; Lefferts, L. *J. Catal.* **2006**, *239*, 460-469. (b) Zhu, H. W.; Suenaga, K.; Hashimoto, A.; Urita, K.; Hata, K.; Iijima, S. *Small* **2005**, *1*, 1180-1183.

142. Perez-Cabero, M.; Taboada, J. B.; Guerrero-Ruiz, A.; Overweg, A. R.; Rodriguez-Ramos, I. *Phys. Chem. Chem. Phys.* **2006**, *8*, 1230-1235.

143. Lin, M.; Tan, J. P. Y.; Boothroyd, C.; Loh, K. P.; Tok, E. S.; Foo, Y. L. *Nano. Lett.* **2006**, *6*, 449-452.

144. Yasuda, A.; Kawase, N.; Mizutani, W. *J. Phys. Chem. B* **2002**, *106*, 13294-13298.

145. Hofmann, S.; Csanyi, G.; Ferrari, A. C.; Payne, M. C.; Robertson, J. *Phys. Rev. Lett.* **2005**, *95*, 036101.

146. Lee, D. C.; Mikulec, F. V.; Korgel, B. A. *J. Am. Chem. Soc.* **2004**, *126*, 4951-4957.

147. Ward, J. W.; Wei, B. Q.; Ajayan, P. M. *Chem. Phys. Lett.* **2003**, *376*, 717-725.

148. Charlier, J. C.; DeVita, A.; Blase, X.; Car, R. *Science* **1997**, *275*, 646-649.

149. (a) Gorbunov, A.; Jost, O.; Pompe, W.; Graff, A. *Carbon* **2002**, *40*, 113-118. (b) Gorbunov, A.; Jost, O.; Pompe, W.; Graff, W. *Appl. Surf. Sci.* **2002**, *197*, 563-567.

150. Jost, O.; Gorbunov, A. A.; Moller, J.; Pompe, W.; Liu, X.; Georgi, P.; Dunsch, L.; Golden, M. S.; Fink, J. *J. Phys. Chem. B* **2002**, *106*, 2875-2883.